



University of Crete
Physics Department

and



Institute of Electronic Structure and Laser
Foundation for Research and Technology Hellas

Advanced Approaches in the Inscription of Bragg Reflectors in Standard and Microstructured Optical Fibers

George Violakis

Heraklion, December 2007

Abstract

The scope of this thesis is the investigation of advanced approaches in the inscription of Bragg grating reflectors in commercial step index and microstructured optical fibers. In the first experimental part, a B/Ge codoped optical fiber is irradiated with 5ps, 500fs and 120fs 248nm laser radiation, while a Type IIA photosensitivity mechanism is observed. The results of the grating inscriptions are examined in terms of modulated and average index changes evaluated using coupled mode theory. The in-fiber Bragg gratings are also subjected to thermal annealing, for quantifying durability and defect stability. Enhanced thermal stability was observed under high intensity irradiation using 500fs, 50mJ/cm² pulses, indicating formation of structural changes in the B/Ge codoped glass matrix. Moreover, the irradiated fibers are examined using Raman laser microscopy and compared to a pristine fiber sample. The Raman spectra indicated - among other changes - a decrease in the Boson peak of the irradiated fibers that was further decreased with increasing pulse intensity. This particular change indicates extended structural reorganization for the fibers irradiated under high intensities.

On the second experimental part of this thesis Bragg inscriptions realized in a commercial microstructured all-silica optical fiber, are presented. For these exposures a 193nm 10ns laser system is utilized and the Bragg gratings are recorded using phase mask interference. Computer simulations of the fiber side illumination with the 193nm laser were realized by employing commercial ray tracing and FDTD software in order to determine the intensity of the light that reaches the fiber core. The fabrication of in-fiber relief Bragg gratings was attempted using advanced fabrication techniques, including gas infiltration.

Περίληψη

Στην εργασία αυτή παρουσιάζονται εξελιγμένες τεχνικές κατασκευής φραγμάτων Bragg σε εμπορικά διαθέσιμες οπτικές ίνες καθώς και σε χωρικά μικροδομημένες οπτικές ίνες (microstructured optical fibers). Στο πρώτο μέρος της εργασίας αυτής εξετάζεται η κατασκευή φραγμάτων Bragg σε ίνες βηματικού δείκτη διάθλασης εμπλουτισμένες στον πυρήνα τους με Βόριο και Γερμάνιο. Για την κατασκευή τους χρησιμοποιήθηκαν συστήματα laser με διάρκεια παλμού 120fs, 500fs και 5ps με μήκος κύματος 248nm και παρατηρήθηκε φωτοευαισθησία τύπου ΠΑ κατά τις εγγραφές. Τα αποτελέσματα αυτά εξετάστηκαν ως προς τις αλλαγές του δείκτη διάθλασης οι οποίες εξήχθησαν από τις εξισώσεις της θεωρίας συζευγμένων τρόπων διάδοσης (coupled-mode). Τα φράγματα Bragg υπέστησαν, επίσης, θερμική ανόπτηση μέχρι την εξάλειψη των εγγεγραμμένων δομών με σκοπό τον χαρακτηρισμό της θερμοκρασιακής τους αντοχής και της αντοχής των επιμέρους δομικών αλλαγών. Παρατηρήθηκε ότι στις εγγραφές που πραγματοποιήθηκαν με δέσμες υψηλών εντάσεων ($50\text{mJ}/\text{cm}^2$, 500fs), η θερμοκρασιακή αντοχή των φραγμάτων Bragg ήταν μεγαλύτερη, υποδεικνύοντας δομικές αλλαγές στην ίνα. Επιπροσθέτως, οι ίνες που ακτινοβολήθηκαν, εξετάστηκαν και με μικροσκοπία Raman και συγκρίθηκαν με δείγμα ίνας που δεν είχε ακτινοβοληθεί. Τα ληφθέντα φάσματα Raman έδειξαν μεγαλύτερη μείωση της κορυφής Μποζονίου όσο η ένταση της δέσμης εγγραφής αυξάνει, επιβεβαιώνοντας την ύπαρξη εκτεταμένων δομικών αλλαγών σε εγγραφές υψηλών εντάσεων.

Στο δεύτερο μέρος της εργασίας αυτής παρουσιάζονται οι εγγραφές φραγμάτων Bragg που πραγματοποιήθηκαν σε μικροδομημένες οπτικές ίνες. Το laser που χρησιμοποιήθηκε ήταν ένα excimer 193nm με διάρκεια παλμού 10ns και οι εγγραφές έλαβαν χώρα μέσω συμβολής με μάσκα φάσης. Επίσης πραγματοποιήθηκαν εξομοιώσεις μέσω εμπορικών προγραμμάτων H/Y (ray tracing και FDTD) της διάδοσης της δέσμης laser μέσα στην ίνα κατά την εγγραφή των φραγμάτων Bragg, για τον προσδιορισμό του ποσοστού της ενέργειας της δέσμης που φτάνει στον πυρήνα της ίνας. Τέλος, έγινε απόπειρα εγγραφής ανάγλυφων φραγμάτων Bragg στις οπές των μικροδομημένων ινών με εξελιγμένες τεχνικές εγγραφής, οι οποίες περιλάμβαναν την εισαγωγή αερίων στις οπές της μικροδομημένης ίνας.

Table of Contents

Abstract	2
Περίληψη.....	3
Table of Contents	4
1. Introduction	6
1.1 Brief historical overview	8
1.2 Bragg grating manufacturing approaches.....	10
1.3 Profiles of Bragg gratings.....	10
1.4 Applications of Bragg gratings.....	11
1.5 State of the art in Ge doped silicate glass fiber photosensitivity.....	13
1.6 State of the art in photonic crystal fibers.....	14
1.7 Thesis overview, motivation and contribution to the field.....	15
References	18
2. Optical properties of fibre gratings.....	22
2.1 Optical fiber properties.....	22
2.1.1 Step index fibers	22
2.1.2 Microstructured Optical Fibers.....	28
2.2 Coupled mode theory	36
2.3 Uniform Bragg gratings.....	40
2.4 Conclusions	42
References	43
3. Photosensitivity of silicate glass optical fibres.....	45
3.1 Photosensitivity of optical fibers with different core compositions.....	45
3.1.1 Ge-doped silicate glass optical fibers	46
3.1.2 B-Ge co-doped optical fibers.....	49
3.1.3 SiO ₂ (undoped) optical fibers	50
3.2 Photosensitivity mechanisms and models	51
3.2.1 Color center model	51
3.2.2 Stress relief model	52
3.2.3 Compaction / Densification model.....	53
3.3 Phenomenological classification of Bragg gratings	54
3.3.1 Type I Bragg gratings.....	55
3.3.2 Type IIA Bragg gratings.....	55
3.3.3 Type II Bragg gratings	56
3.3.4 Other Types of Bragg gratings	56
3.4 Femtosecond induced interactions	57
3.4.1 Non linear ionization	57
3.4.2 Heat accumulation - dissipation	59
3.5 Conclusions	60
References	61
4. Type IIA Bragg Grating Inscriptions in B-Ge fibers using 248nm fs and ps laser radiation.....	66
4.1 Bragg grating inscription apparatus and methodology.....	67
4.1.1 Laser systems	67
4.1.2 The phase mask technique.....	68
4.1.3 Bragg grating inscription setup	69
4.1.4 Annealing setup.....	71

4.2 Recordings of Bragg gratings in B/Ge codoped optical fibers using 248nm ps and fs laser radiation.....	72
4.2.1 500fs inscriptions	72
4.2.2 Comparative nanosecond laser inscriptions	75
4.2.3 Comparative 120fs, 500fs and 5ps inscriptions.....	76
4.2.4 Annealing results	79
4.2.5 Discussion.....	81
4.3 Inscriptions using other laser wavelengths.....	84
4.4 Unsaturated inscriptions of Type IIA gratings	85
4.5 Raman scattering measurements	87
4.6 Intensity effects in the inscription process	92
4.7 Conclusions	94
References	95
5. Bragg Grating Inscriptions in Microstructured Optical Fibers.....	99
5.1 Experimental setup	101
5.1.1 Backside gas etching exposures on flat, thin fused silica bulks	101
5.1.2 Bragg grating inscription setup in Microstructured Optical Fibers.....	103
5.2 Computer Simulations for Side Illumination of the Microstructured Optical Fibers	105
5.3 Backside gas etching irradiation results in slab samples.....	108
5.3.1 Etching gas – SF ₆	108
5.3.2 Experimental results	109
5.4 Microstructured Optical Fiber Inscriptions	113
5.4.1 Inscriptions without gas flow	113
5.4.2 Inscriptions with SF ₆ flow inside the PCF	116
5.4.3 Inscription attempts using other gases.....	121
5.5 Conclusive remarks	122
References	123
6. Conclusions – Future perspectives	125
List of Publications.....	127
Journal Papers.....	127
International Conferences.....	127

1. Introduction

The fiber Bragg grating is an in-fiber component that was realized after the discovery of photosensitivity in optical fibers. A fiber Bragg grating is an optical fiber in which the refractive index in the core is perturbed forming a periodic or quasi-periodic index modulation profile (Figure 1.1). A narrow band of the incident optical field within the fiber is reflected by successive, coherent scattering by the index variations. When the reflection from a crest in the index modulation is in phase with the next one, maximum mode coupling or reflection is achieved. It is then that the Bragg condition is fulfilled, which is:

$$\lambda_B = 2n_{\text{eff}}\Lambda \quad (1.1)$$

where λ_B is the Bragg wavelength, n_{eff} is the effective modal index and Λ is the perturbation period [1]. Equation 1.1 is derived from the phase matching condition:

$$k_r = k_i + 2\pi/\Lambda \quad (1.2),$$

where k_r is the propagation constant of the backwards propagating mode, k_i is the propagation constant of the forward propagation mode and Λ the period of the grating as defined in 1.1.

Photosensitivity refers to the permanent – and in some cases reversible – change in the index of refraction of the optical material when exposed to light with characteristic wavelength and intensity that depends on the material synthesis and structure. The changes of the refractive index can originate from structural modification or chemical reactions inside the optical material initiated by the light source. The physical mechanism behind photosensitivity has been intensively studied during the last decades providing a strong theoretical foundation for the changes induced by the light and matter interactions. There are though certain aspects of photosensitivity that are not yet fully understood or experimentally verified.

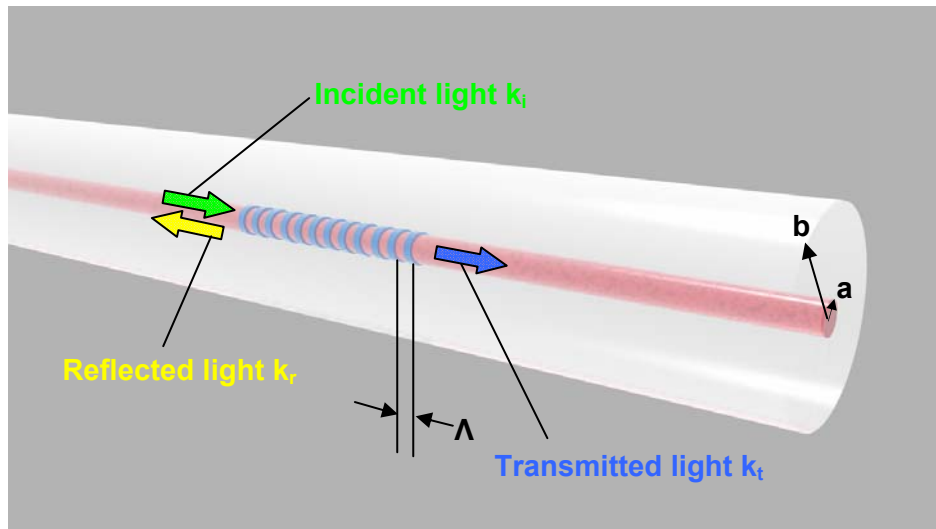


Figure 1.1 Optical fiber with periodic modulation of the refractive index (blue planes spaced at a distance of Λ) in the fiber core (red region). Fiber core radius is a and cladding radius is b .

Bragg gratings are capable of performing specific optical functions including reflection, spatial or temporal dispersion of the guided light. Depending upon the design and scattering properties, fiber Bragg gratings find numerous real field applications in optical communications and sensing fields. The easy applicability of the fiber Bragg gratings in the above fields is promoted by the advantages offered by optical fiber, such as low loss transmission, immunity to electromagnetic interference, light weight and electrical isolation.

The periodicity of the index modulation of a typical Bragg grating in a silicate fiber for scattering at the telecommunications $1.5\mu\text{m}$ band lies near the value of 530nm . The above can be easily extracted by applying the above value to Equation 1.1 along with an effective index value of 1.43 (low concentration Ge in the fiber glass). Reflectivities approaching 100% are possible, with the grating bandwidth ($\Delta\lambda$) tailored from typically 0.1 nm to in excess of 10 nm [2].

The fiber Bragg grating is also sensitive to temperature and strain perturbations, which modify the phase matching condition and lead to wavelength dependent reflectivity. Therefore, the tracking of the wavelength at which the Bragg reflection occurs can be related to the magnitude of an external perturbation. A large number of gratings can be photo-imprinted at predetermined locations on the optical fiber to realize a quasi-distributed sensor network for structural monitoring with relative ease and low cost. For example, Bragg gratings are ideal candidates for sensors that measure dynamic strain in aerospace applications and as temperature sensors for

monitoring thermal load applications. The chemical and biological inertia of the silicate glass, as well as, its relatively high glass transition point and immunity to electromagnetic interference make fiber Bragg gratings ideal for applications where conventional sensors (manufactured for example from metallic alloys) would deteriorate, or not function properly.

Finally, it is also possible to have fiber grating structures that are transmissive, coupling light between core and cladding modes. In this case the phase matching condition dictates that the grating periodicity is several hundred microns, and accordingly these components are known as long period gratings [3].

1.1 Brief historical overview

The first ever demonstration of germanosilicate fiber photosensitivity took place at the Communications Research center by Hill and co-workers in 1978 [4]. Photosensitivity was observed when launching laser light from a single frequency Argon laser emitting at 514.5nm into the core of a germania doped silica fiber. Several minutes after the launch of the laser light into the core it was found that a fraction of the incident power was reflected back by the fiber towards the laser source. The origin of this reflection was found to be the formation of an index grating that had been permanently inscribed inside the fiber core. That was the first in-fiber grating formation reported. This kind of grating, though, was practically useless because of its ability to reflect only the wavelength that has inscribed it. In the following decade Lam and Garside [5] showed that the magnitude of the photoinduced refractive index change is dependent on the square of the writing power of the argon laser. This implied that a two step absorption process was behind the inscription of the reflecting structure.

In order to overcome the restrictions induced by internally inscribed fiber gratings, external inscription methods were utilized. The first method of these, involved the polishing of the side of an optical fiber and then the physical etching of the grating into it. This process, though, required several days of work and included steps that could easily lead to failure of the etch process and was later abandoned.

What actually revolutionized grating inscriptions in optical fibers was the side-writing technique (also called the transverse holographic technique) that was first demonstrated at the United Technologies Research Center by Meltz, *et al*, [6].

Following the findings of Lam and Garside [5], Meltz and co-workers were the first to demonstrate the inscription of permanent gratings by exposing an optical fiber from the side to two interfering beams of ultraviolet light [6]. Using this technique it was possible to fabricate Bragg reflectors at any wavelength longer than the inscribing wavelength, making the holographic technique a versatile tool that could produce reflectors scattering in the communications infrared or other regions. Furthermore, contrary to the relief gratings, this new technique was capable of inscribing gratings within minutes with very low loss and without the need to polish or heavily modify and destroy the fiber hyperstructure.

It was after Meltz's [6] discovery that the field of fiber grating inscription significantly progressed. As a consequence of this intense interest that was cultivated in the field, it only took a few years to develop techniques such as the point – by – point inscription [7] or the popular phase mask technique[8],[9]. Parallel to the new grating inscription techniques, research was also conducted in the field of fiber photosensitivity. It was found that fiber photosensitivity could be greatly enhanced by co-doping the core with Tin [10], Boron [11], or Aluminum [12] or by naturally increasing the amount of Germanium inside the fiber core. Another significant discovery took place in 1993, when Mizrahi, *et al*, managed to increase the photosensitivity of an optical fiber by diffusing molecular hydrogen inside it under high pressure (hydrogen loading technique) [13]. Later, in 2003, Dianov, *et al*, used a femtosecond Ultraviolet laser source to inscribe fiber Bragg gratings [14]. The high intensity that such laser systems provide leads to the efficient inscription of Bragg gratings and provides new means for photosensitivity study.

During the last decade and following the demonstration of photonic crystal fibers by Rusell, *et al*,[15], a lot of interest has been concentrated in the fabrication of Bragg gratings in photonic crystal fibers. This interest rises from the fact that these fibers exhibit unique optical and mechanical properties that could be exploited by recording fiber grating and developing devices such as high efficiency biological/chemical sensors or high power delivery systems. These fibers can be made of undoped high-purity silicate glass and thus demonstrate very low intrinsic photosensitivity. However, Canning, *et al*, was able to inscribe a Bragg grating in a custom made photonic crystal fiber of relatively low quality glass [16] and Eggleton, *et al*, managed to do the same in hydrogen loaded pure silica photonic crystal fibers [17].

1.2 Bragg grating manufacturing approaches

As mentioned above [4], the first demonstration of Bragg grating inscription by Hill et al was realized using an internal writing technique. This technique requires a single frequency laser light whose absorption lies in the UV photosensitivity region of the fiber, so that index modulation can take place. This method features minimal flexibility in the design of the inscribed structure.

Nowadays there are commonly two approaches in external Bragg grating inscription. Point – by – point inscription [7] and the phase mask technique [9]. The phase mask is a diffractive optical element. Incident ultraviolet (UV) radiation to the phase mask will be diffracted to multiple diffraction orders. The phase mask is designed in a way that the majority of the incident power is equally split to two orders, which interfere with each other, photoimprinting to the fiber core a periodic refractive index modulation profile. For the experimental part of this thesis the phase mask technique was solely used, which will be briefly described in the experimental part of this thesis.

1.3 Profiles of Bragg gratings

The fiber Bragg grating has been characterized in section 1.1 as an optical fiber which has a periodic perturbation of the refractive index in its core. This perturbation can be either periodic or quasi-periodic. This means that under specific grating inscription conditions, it is easy to achieve a variety of index perturbation profiles that will in turn lead to different reflection and transmission spectra.

The most simple and commonly inscribed grating profile is the uniform grating (Figure 1.2). In this type of grating the fringe pattern period is kept constant between the grating planes to the value Λ as defined in section 1.1. The resulting reflection spectrum features a major lobe centered at the design wavelength of the grating, accompanied by minor (much lower in intensity) side lobes on each side which are risen due to phase matching at the edges of the uniform grating. In this thesis all gratings inscribed were tailored to be as uniform as experimentally possible. Uniform gratings are easily inscribed using the phase mask technique in contact mode with the fiber, as it will be later described.

In order to wash out the side lobes that are produced by the uniform gratings, a tapered grating profile can be used. Another interesting grating profile is that of the

chirped grating which can be easily produced by the point by point technique, which is the most common case for these gratings due to the flexibility it offers. In this case the grating plane distance is not constant, but varies along the grating axis usually in a monotonic manner. Moiré gratings are produced by superimposing two gratings of slightly different periods. Finally, blazed gratings are formed when the grating planes are at an angle with respect to the fiber axis.

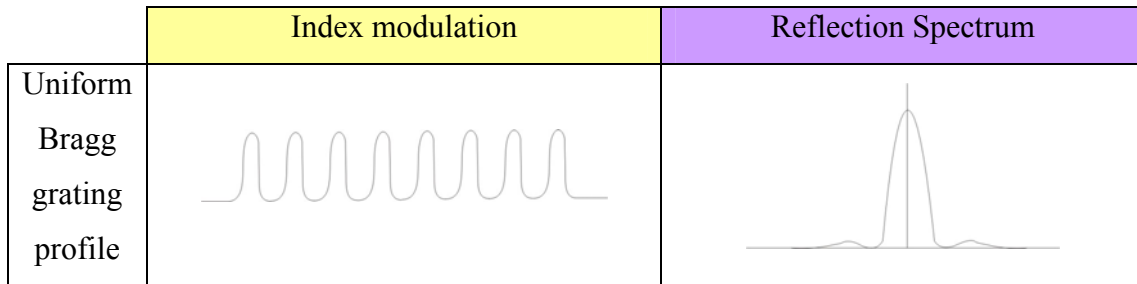


Figure 1.2 Uniform Bragg grating profile and reflection spectrum

1.4 Applications of Bragg gratings

Until recently (year 2000), the highest motivation for the research and development of in-fiber gratings has been the optical telecommunications revolution. Nowadays the unique properties of the optical fibers have been exploited for the production of in-fiber sensors. With the advent of photonic crystal fibers, new telecommunications components and sensing devices are possible, extending the applications to fields for which conventional fibers were inadequate. In short the two major application fields of in-fiber gratings are the telecommunications and the sensing industries.

The contribution of fiber gratings to the telecommunications industry is significant. Their unique filtering properties and versatility is reflected on the wide range of uses they have in the optical telecoms. They have been used in wavelength stabilized lasers, remote pump amplifiers, Raman amplifiers, phase conjugators, wavelength converters, passive optical networks, wavelength division multiplexers and demultiplexers, add/drop multiplexers, dispersion compensators, and gain equalizers [2]. A list of some of the applications where in-fiber gratings are used in telecoms, along with a brief description of the main optical features and grating parameters is shown in Table 1.1 after reference [2].

Table 1-1 Applications of Bragg gratings in the telecommunications (after [2])

Applications	Description
Fiber laser	Narrowband reflector
Laser wavelength stabilization (980nm, 1480nm)	Narrowband reflector
Pump reflector in fiber amplifiers (1480nm)	Highly reflective mirror
Raman amplifiers (1300nm, 1550nm)	Several highly reflective mirror pairs
Isolation filters in bidirectional WDM transmission (1550nm)	Matched sets of WDM gratings
Pump reflector in phase conjugator (1550nm) and isolation filter in wavelength converter	Highly reflective mirror
WDM demultiplexer (1550nm)	Multiple high-isolation reflectors
WDM add/drop filter (1550nm)	High isolation reflector
Optical amplifier gain equalizer (1530-1560nm)	Blazed Bragg gratings or long period grating
Dispersion compensation for long-haul transmission (1550nm)	Chirped grating

In the field of sensing the in-fiber gratings exhibit unique advantages compared to mechanical, electrical, electronic, or other types of optical sensors [19]. Their principal advantage is that the measured quantity is wavelength encoded, making the sensor self-referencing, rendering it independent of fluctuating light levels and the system immune to source power and connector losses [19]. Moreover, they exhibit linear response over many orders of magnitude from parts per billion up to several percent. Immunity to electromagnetic interference, light weight, flexibility, stability, high temperature tolerance and even durability against high radiation environments make the use of fiber sensors preferable in certain applications, like temperature monitoring [20], strain and structural monitoring [19]. It is also crucial to mention the small diameter of the optical fibers that make them irreplaceable in applications where small diameter probes are required such as medicine [21] and surgery [22]. The flexibility in the deployment of optical fibers can make possible the construction of a complex sensor network that can monitor multiple parameters at a single instance. Furthermore, new optical fiber geometries like tapered fibers, or photonic crystal fibers, can be exploited to expand in-fiber grating sensitivity to the fields of chemical and biological sensing.

Table 1-2 Applications of Bragg gratings in the sensors industry

Applications	Description
Structural monitoring	Tension sensing
	Torsion sensing
Temperature monitoring	Temperature sensing
Medical applications	Biological sensing
	In vivo sensing
	Surgery
Hazardous environment sensing	Nuclear reactor temperature sensing
Chemical sensing (PCF-MOF)	Chemical substances sensors
Pressure monitoring (PCF-MOF)	Pressure sensing

1.5 State of the art in Ge doped silicate glass fiber photosensitivity

As stated in the historical overview section, photosensitivity in optical fibers has been studied since 1978. Since then, the systematic study of this physical mechanism has led to significant advancements like the addition of co-dopants like Sn, Al, B among many others in the fiber core to raise the fiber's photosensitivity. Hydrogen infusion to the fiber was another significant technique [13] which again raises photosensitivity and leads to very efficient Bragg grating inscription. Femtosecond laser systems have been recently used for the inscription of Bragg gratings [14] and provide a quite efficient means of fiber Bragg grating recording. Both infrared [23] and Ultraviolet [14] laser systems have been used for Bragg grating, as well as long period [24] grating inscription. They can produce from Type I to Type II gratings (which will be discussed in Chapter 3) with sharply tailored spectral features and relatively small energy density per pulse.

The utilization of femtosecond laser systems for Bragg grating inscription does not come without a cost in fabrication flexibility. The use of interferometric setups for holographic exposure of an optical fiber is practically prohibited by the strict alignment requirements. The path lengths of the interfering beams must be matched to within the spatial location of the fs-pulse [37], restricting the practical inscription setups to those using a phase mask to create the interference pattern. On the other hand, the utilization of a phase mask can restrict the fluence per pulse due to non-linear absorption in the phase mask slab. The phase mask and the optical fibers are

made of the same host material, SiO₂. Under high intensities the phase mask could nonlinearly absorb light resulting in phase mask damage [31]. Another potential problem arises from the use of phase masks with pitch spacing similar to the laser inscription wavelength. The large spectral content of the femtosecond pulse would be broadly dispersed and the energy would be spread over a large area [38]. This problem can be easily overcome though with the use of suitable phase masks, of long period.

Despite the above shortcomings, femtosecond laser systems are the cutting edge technology for producing fiber Bragg gratings in photosensitive step index fibers. The large intensity per pulse provides the means for routine and fast inscription of strongly reflecting Bragg gratings (>99.9% reflectivity). Moreover, the short pulse duration can give rise to multiphoton absorption and contribute to the inscription process. The absence of heat diffusion effects for repetition rates below 200kHz [36] is also acting positively for the purposes of photosensitivity study, as it removes this complex mechanism from the system under study. Finally, the use of a femtosecond laser system along with systems with different pulse durations, provide the means for a direct comparison of the effect of the intensity per pulse on the inscription process.

1.6 State of the art in photonic crystal fibers

Despite the fact that photonic crystal fibers (PCFs) have only been recently demonstrated by Russel, *et al*, [15],[25], a significant amount of research is focused in inscribing Bragg gratings in them. Their unique structure makes them exceptionally attractive for sensing and high power delivery applications. Research in producing externally written Bragg gratings in PCFs involved prior sensitization of the fiber, most commonly with hydrogen infusion under high pressure and then irradiation [17]. Another approach was the doping of the PCF's core with specific ion for enhancing photosensitivity and then irradiation of the fiber to record Bragg gratings inside it [26]. More recently, Canning, *et al*, [16] showed that such structures could be realized in custom made – relatively low quality silicate glass PCFs, using 193nm laser radiation and a phase mask, without any preconditioning of the fiber. Due to the nature of PCFs, Bragg grating inscription in these fibers is not a routine process and does not exhibit the easiness of the recording in highly photosensitive optical fibers.

Moreover the use of the dopants in the fiber structure or the use of low quality glass, may in general affect the optical performance of these special fibers.

The difficulty of producing Bragg gratings in PCFs due their intrinsically low photosensitivity has made long period grating (LPG) recording popular for these fibers. The methods used for creating LPGs include the use of mechanical means to emboss the grating pattern to the fiber [27], the use of an electric arc to rapidly melt and quench “slices” inside the fiber core [28] and the use of UV femtosecond laser systems [29]. Although all of the above methods are successful in LPG recording, the whole process –as in the case of Bragg grating recording in PCFs- is not easily repeatable and exhibits variations from fiber to fiber.

The two major challenges in the recording of Bragg gratings in photonic crystal fibers is the achievement of large refractive index changes and the repeatable inscription processing. Canning et al [30], who filled the capillaries of the photonic crystal fibers with various liquids, succeeded in improving the side illuminated Bragg grating recording efficiency. Although this work resulted in some promising results, the inscribed strong gratings were not symmetric and exhibited spectral irregularities. However, both of the above goals are attempted to be reached in this work as will be briefly discussed in the following section.

1.7 Thesis overview, motivation and contribution to the field.

Although the first in-fiber grating appeared almost 30 years ago, there are still many challenges in Bragg grating inscription in optical fibers. For the case of photosensitive step index fibers these are summed in the following points:

- 1) Increase of the photoinduced refractive index change during Bragg grating inscription. This is important for the realization of high performance and functional devices for both the sensing industries and the optical telecommunications.
- 2) Production of temperature resistant Bragg gratings with precisely tailored spectral characteristics for high resolution sensing applications.
- 3) Understanding of the physical mechanisms behind photosensitivity and laser induced Bragg grating recording in optical fibers, and the study of the effect

of the laser wavelength, energy density and duration in the photoinduced changes of the irradiated glass.

In the current thesis the recording of strong and thermally durable Bragg reflectors in a commercial B-Ge optical fiber by employing fs and ps 248nm laser radiation is examined. By using femtosecond laser systems it is possible to record Bragg gratings by employing high intensities per pulse and have the possibility to compare recording efficiency between various pulse durations of the same wavelength. By studying the effects of inscription laser pulse duration and intensity in photosensitive fibers and exhibiting enhanced thermal stability in them, novel data was retrieved concerning the effect of laser pulse duration in the recording process [31-34]. These fibers due to their enhanced thermal stability can be used for sensing in high temperature ambience or post-exposure treated with high temperature processes.

A second goal presented in this thesis refers to the recording of Bragg grating reflectors in microstructured optical fibers (MOFs) using advanced laser processing methods. Concerning MOFs or photonic crystal fibers, the greatest challenge in Bragg grating inscription can be presented in three major points:

- 1) Increase of the photoinduced refractive index changes during Bragg grating inscription, which is usually much smaller than in photosensitive fibers, under the same inscription conditions
- 2) Easy fabrication of Bragg gratings in MOFs and PCFs. The complex nature of the structure of these fibers raises diffraction, scattering and more complex optical mechanisms during irradiation for Bragg grating recording, resulting in systems that do not exhibit repeatable results.
- 3) Understanding of the physical mechanisms during the irradiation process, as for the case of step index photosensitive fibers

The study of Bragg grating inscription behavior of commercial high quality MOFs and the development of a setup making such recordings routine have provided new insight into the MOF Bragg grating recording technology. Routine Bragg grating inscription in commercial MOFs is a significant achievement, because of their intrinsic low photosensitivity. Such capability is reported, to the author's best knowledge, for the first time for untreated, undoped, pure silica MOFs [35]. Adding to the above, the attempt to produce relief gratings in MOFs, although not successful, led to the accumulation of important knowledge on the reasons of failure and will

provide useful input into future experiments, focused in the same goal. Finally, computer simulations were conducted for the propagation of the laser beam across the fiber structure and resulted in useful data concerning the effectiveness of the inscription process.

The above data will be discussed in detail in the subsequent pages.

Chapter 2: A brief overview of the step index and photonic crystal fiber optical properties is presented along with the essential theoretical tools for basic computations and analysis of Bragg gratings.

Chapter 3: The photosensitivity models are presented for the cases of pure silica fibers and doped fibers. Alongside them, there is a short report on the interaction between femtosecond laser radiation and matter.

Chapter 4: Bragg grating inscriptions on the B/Ge codoped optical fiber using various laser wavelengths and pulse durations. Discussion of the results.

Chapter 5: Bragg grating inscriptions on microstructured optical fibers and laser etching setup for fused silica. Attempts to inscribe relief gratings in these fibers are also presented and discussed.

Chapter 6: Conclusions, along with future perspectives and applications.

References

- [1] T. Erdogan, "Fiber Grating Spectra", *Journal of Lightwave Technology*, **15** : 1277 – 1294, (Review Article), (1997)
- [2] A. Othonos and K. Kalli, "Fiber Bragg gratings", Artech House Inc., London, (1999)
- [3] S.J. James and R.P. Tatam, "Optical fibre long-period grating sensors: characteristics and application" (review article), *Meas. Sci. Technol.* **14**: R49–R61, (2003)
- [4] K.O. Hill, "Photosensitivity in optical fiber waveguides: application to reflection fiber fabrication", *Applied Physics Letters*, **32**: 647, (1978)
- [5] D.K.W. Lam and B.K. Garside, "Characterization of single mode optical fiber filters", *Applied Optics*, **20**: 440-445, (1981)
- [6] G. Meltz, *et al*, "Formation of Bragg gratings in optical fibers by a transverse holographic method", *Optics Letters*, **14**: 823, (1989)
- [7] B. Malo, K.O. Hill, F. Bilodeau, D.C. Johnson, J. Albert, *Electronics Letters*, **29**: 1668-1669, (1993)
- [8] D.Z. Anderson, V. Mizrahi, T. Erdogan and A.E. White, "Production of in fibre gratings using a diffractive element", *Electronics Letters* **29**: 566-568, (1993)
- [9] K.O. Hill, B. Malo, F. Bilodeau, D.C. Johnson and J. Albert, "Bragg gratings fabricated in monomode photosensitive optical fibre by UV exposure through a phase mask", *Appl. Phys. Lett.* **62**: 1035-1037, (1993)
- [10] A. Dragomir, D.N. Nikogosyan and G. Brambilla, "Increased photosensitivity of Ge-doped and Ge, Sn-doped fibres under high-intensity 264 nm laser light", *Electronics Letters* **39**: 1437–1438, (2003)
- [11] C.W. Haggans, W.F. Varner, J-S. Wang, US patent No. 6058231, (2000)
- [12] Maurer and Schultz, US patent No. 3659915, Corning Glass Inc., (1972)
- [13] V. Mizrahi, P.J. Lemaire, T. Erdogan, W.A. Reed, D.J. DiGiovanni and R.M. Atkins, *Applied Physics Letters* **63**: 1727, (1993)
- [14] A. Dragomir, D.N. Nikogosyan, K.A. Zagorulko, P.G. Kryukov and E.M. Dianov, "Inscription of fiber Bragg gratings by ultraviolet femtosecond radiation", *Optics Letters* **28**: 2171–2173, (2003)

- [15] J. C. Knight, J. Broeng, T. A. Birks and P. St. J. Russell, "Photonic band gap guidance in optical fibers," *Science* **282**, 1476-1478, (1998)
- [16] N. Groothoff, J. Canning, E. Buckley, K. Lyttikainen and J. Zagari, "Bragg gratings in air-silica structured fibers", *Optics Letters* **28**: 233-235, (2003)
- [17] L.B. Fu, G.D. Marshall, J.A. Bolger, P. Steinvurzel, E.C. Magi, M.J. Withford, B.J. Eggleton, "Femtosecond laser writing Bragg gratings in pure silica photonic crystal fibres", *Electronics Letters* **41**: 638-640, (2005)
- [18] Kristian Buchwald, "Fused Silica Transmission Gratings", White Paper (available through www.ibsen-photonics.dk), (2007)
- [19] W. Gornal and T. Amarel, "Applications and techniques for fiber Bragg grating sensor measurements", White Paper (available through www.ottawaphotonics.com), EXFO Burleigh Products Group, (2003)
- [20] S.W. James, R.P. Tatam, A. Twin, M. Morgan and P. Noonan, "Strain response of fibre Bragg grating sensors at cryogenic temperatures", *Meas. Sci. Technol.* **13**: 1535-1539, (2002)
- [21] Y.J. Rao, D.J. Webb, D.A. Jackson, L. Zhang and I. Bennion "Optical In-Fiber Bragg Grating Sensor Systems for Medical Applications", *Journal of Biomedical Optics* **3**: 38-44, (1998)
- [22] Gunther Wehrle, Percy Nohama¹, Hypolito Jos'e Kalinowski, Pedro Ign'acio Torres and Luiz Carlos Guedes Valente, "A fibre optic Bragg grating strain sensor for monitoring ventilatory movements", *Meas. Sci. Technol.* **12**:805-809, (2001)
- [23] S.J. Mihailov, C.W. Smelser, D. Grobnic, R.B. Walker, P. Lu, H. Ding and J. Unruh, "Bragg Gratings Written in All-SiO₂ and Ge-Doped Core Fibers with 800-nm Femtosecond Radiation and a Phase Mask", *Journal of Lightwave Technology* **22**: 94, (2004)
- [24] Y. Kondo, K. Nouchi, T. Mitsuyu, M. Watanabe, P.G. Kazansky, K. Hirao, "Fabrication of long period fiber by focused irradiation of infrared femtosecond laser pulses", *Opt. Lett.* **24**:646-648, (1999)
- [25] P. St. J. Russell, "Photonic crystal fibers," *Science* **299**, 358-362 (2003). (Review article.)
- [26] B.J. Eggleton, P.S. Westbrook, R.S. Windeler, S. Spalter and T. A. Strasser, "Grating resonances in air-silica microstructured optical fibers", *Optics Letters* **24**: 1460-1462, (1999)

- [27] K.N. Park, T. Erdogan and K.S. Lee, “Cladding mode coupling in long-period gratings formed in photonic crystal fibers,” *Optics Communication* **26**: 541–545, (2006)
- [28] H. Dobb, K. Kalli and D. Webb, “Temperature-insensitive long period grating sensors in photonic crystal fibre,” *Electronics Letters* **40**: 657–658, (2004)
- [29] A.A. Fotiadi, G. Brambilla, T. Ernst, S.A. Slattery, and D.N. Nikogosyan, “TPA-induced long-period gratings in a photonic crystal fiber: inscription and temperature sensing properties”, *Journal of Optical Society of America B*. **24**: 1475-1481, (2007)
- [30] H.R. Sorensen, J. Canning, J. Laegsgaard, K. Hansen, P. Varming, “Liquid filling of photonic crystal fibres for grating writing”, *Optics Communications* **270**: 207-210, (2007)
- [31] G. Violakis, M. Konstantaki, S. Pissadakis, “Accelerated Recording of Negative Index Gratings in Ge-Doped Optical Fibers Using 248-nm 500-fs Laser Radiation”, *IEEE Photonics Technology Letters*, **18**: 1182, (2006)
- [32] G.Violakis, M.Konstantaki, S.Pissadakis, “Inscription of Thermally Durable Type IIA Gratings in B-Ge doped Optical Fibres Using 248nm, 500fs Radiation”, *CLEO-USA*, CTuY6, (2006)
- [33] S. Pissadakis, M. Konstantaki, G. Violakis, “Recording of Type IIA Gratings in B-Ge codoped Optical Fibres Using 248nm Femtosecond and Picosecond Laser Radiation”, *ICTON 2006*, Nottingham, UK, (2006)
- [34] G. Violakis, M. Konstantaki, S. Pissadakis, “Comparative Studies on Type IIA Photosensitivity in a B-Ge Optical Fiber Using Ultraviolet Femtosecond Radiation”, *BGPP 2007*, Quebec, Canada, (2007)
- [35] G. Violakis, S. Pissadakis, “Bragg Grating Inscription in a Commercial Solid Core Microstructured Optical Fiber”, *ICTON 2007*, Rome, Italy, (2007)
- [36] S. M. Eaton, H. Zhang, P. R. Herman, F. Yoshino, L. Shah, J. Bovatsek, A. Y. Arai, “Heat accumulation effects in femtosecond laser written waveguides with variable repetition rate”, *Optics Express* **13**: 4708-4716, (2005)
- [37] K. I. Kawamura, N. Sarukura, M. Hirano, H. Hosono, “Holographic encoding of fine-pitched micrograting structures in amorphous SiO₂ thin films on silicon by a single femtosecond laser pulse”, *Applied Physics Letters*, **78**: 1038-1040, (2001)

[38] G. D. Goodno, G. Dadusc, R. J. D. Miller, “Ultrafast heterodyne-detected transient grating spectroscopy using diffractive optics”, *Journal of the Optical Society of America*, **15**: 1791-1794, (1998)

2. Optical properties of fibre gratings

In order to understand the operation principles of fiber gratings it is necessary to have a global view on light propagation in these stratified optical fibers. Fiber gratings can be broadly classified into two types: Bragg gratings (also called reflection and short period gratings), in which coupling occurs between modes traveling in opposite directions and transmission gratings (also called long period gratings), in which the coupling is between modes traveling in the same direction. In the experimental work conducted for this thesis, Bragg gratings have been inscribed in either conventional or microstructured optical fibers. The propagation principles in both types of the above fibers will be examined. Coupled wave theory will be applied in order to retrieve the main optical properties and propagation through Bragg fiber gratings. The formalism used in this chapter is initially used to derive the reflectivity and band width of the grating with respect to geometrical and physical properties of the fiber. Finally, the general model is applied to analyze the coupling to cladding modes. The whole analysis performed holds for uniform Bragg gratings.

2.1 Optical fiber properties

In this section key geometrical and optical features of conventional and microstructured optical fibers will be presented. By examining the structural layout and refractive index distribution inside the glass matrix, values for key optical parameters will be derived, which will be useful in the later analysis of coupled mode theory. The differences in light propagation inside these two substantially different fiber types will be also discussed.

2.1.1 Step index fibers

A cylindrical step index fiber is characterized by the diameter of the core and the cladding. The core, for the optical fiber in Figure 2.1, has a diameter of the order of $6 - 12\mu\text{m}$ – in the case of single mode fibers – and a cladding diameter of $125\mu\text{m}$, optimized for the $1.5\mu\text{m}$ telecommunications window. The fiber is surrounded by a protective polymer jacket extending to a diameter of $250\mu\text{m}$. The cladding is made of silicate glass and is usually undoped in contrast with the core which is made of the

same glass but it is doped with elements such as germanium, boron [2], aluminum [3], tin [1] and others (Er, Yb) depending on the desired fiber properties. Most of the step index optical fibers used here are fabricated using the Modified Chemical Vapor Deposition (MCVD) technique. The refractive index profile of the step index fiber has as follows:

$$n(r) = n_{co} = n_{cl} (1+\Delta), \quad r \leq a$$

$$n(r) = n_{cl}, \quad a < r \leq b$$

$$n(r) = n_{env}, \quad r > b$$

where n_{co} , n_{cl} and n_{env} are constants (refractive indices of core, cladding and surrounding environment), a and b are the core and cladding radii and Δ is the relative core – cladding index difference, usually of the order of 1% for single mode fibers.

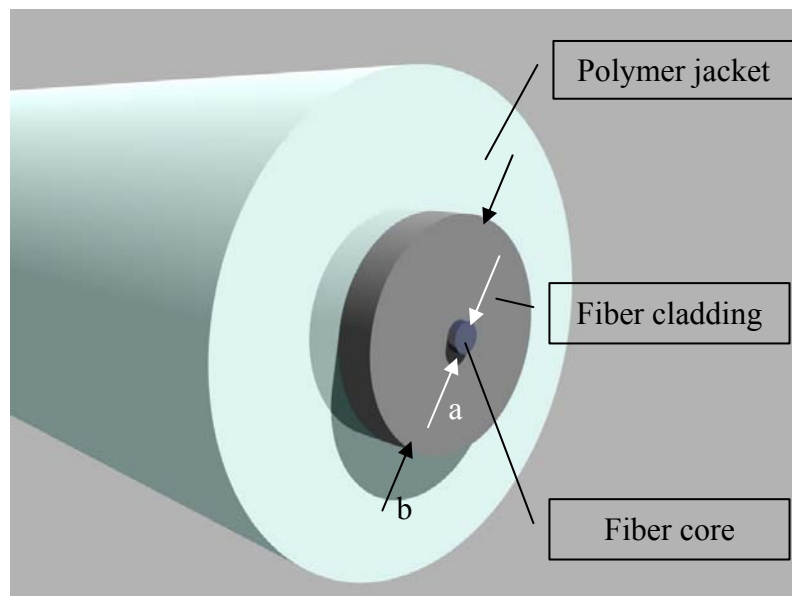


Figure 2.1 Step index fiber layout

The principle of operation of a step index fiber lays in the total internal reflection of the guided light at the core - cladding interface [4]. Total internal reflection is possible when the light is probed under certain angle inside the fiber, called critical angle, which is derived from Snell's law [5]. A single mode fiber is designed in a way that will only support one propagation mode of light of particular wavelength. The propagation constant k_z of that mode, called the fundamental mode, will lie between the values of: $\frac{\omega}{c} n_{cl} < k_z < \frac{\omega}{c} n_{co}$ [6] with ω referring to the frequency of the guided light and c the speed of light in vacuum. The lower and upper bounds represent the low frequency (cutoff) and high frequency limits, respectively.

The refractive index of the core (n_{co}) has a value close to the refractive index of the cladding so that the fiber supports only one mode at a particular wavelength as the previously stated inequality suggests.

The fundamental mode can be approximated for simplicity as a plane wave, linearly polarized in one direction. If the propagation direction chosen is \hat{y} the wave fields are approximately given by:

$$\begin{Bmatrix} E(x, y, z) \\ H(x, y, z) \end{Bmatrix} \cong \begin{Bmatrix} \hat{y}\Psi(x, y) \\ -\frac{\bar{x}}{\eta}\Psi(x, y) \end{Bmatrix} e^{-k_z z} \quad (2.1)$$

where $\Psi(x, y)$ represents the variation in field amplitude along the fiber radial direction and the characteristic impedance η is given by

$$\eta = \sqrt{\frac{\mu_0}{\varepsilon}} \text{ with } \varepsilon \cong \varepsilon_0 n^2. \quad (2.2)$$

Function $\Psi(x, y)$ satisfies the general wave equation expressed in cylindrical coordinates:

$$\left(\frac{\partial^2}{\partial r^2} + \frac{1}{r} \frac{\partial}{\partial r} + \frac{1}{r^2} \frac{\partial^2}{\partial \phi^2} + \omega^2 \mu \varepsilon_i - k_z^2 \right) \Psi(r, \phi) = 0 \quad (2.3)$$

where ε_i refers to either the core or cladding region. By applying variable separation on $\Psi(r, \phi)$ it becomes:

$$\Psi(r, \phi) = \psi(r) \begin{pmatrix} \sin q\phi \\ \cos q\phi \end{pmatrix}, \text{ where } q \text{ is an integer.} \quad (2.4)$$

Substituting $\Psi(r, \phi)$ to the wave equation one gets:

$$\left[\frac{\partial^2}{\partial r^2} + \frac{1}{r} \frac{\partial}{\partial r} + \frac{1}{r^2} \frac{\partial^2}{\partial \phi^2} + (\omega^2 \mu \varepsilon_i - k_z^2) - \frac{q^2}{r^2} \right] \psi(r) = 0 \quad (2.5)$$

which is separately solved for the core/clad regions with: $k_\rho^2 = \omega^2 \mu \varepsilon_i - k_z^2$.

The solutions of the wave equation (5) are the Bessel (J) and Neumann (K) functions or a linear combination of them [6] of the form:

$$\psi(r) = \sum_q A_q J_q(k_\rho r) + \sum_q B_q K_q(k_\rho r) \quad (2.6)$$

In order to calculate the solution of the wave equation (5) in the core region it is necessary to introduce the wavenumber u that is normalized to the fiber core's radius

$$a, \text{ and defined as: } u^2 = (k_2^2 - k_z^2) a^2 \quad (2.7)$$

By substituting (7) into (6) the wave equation solution inside the core region

becomes:

$$\Psi(r, \phi) = AJ_q(u/ar) \begin{pmatrix} \cos q\phi \\ \sin q\phi \end{pmatrix} e^{-ik_z z} \quad (2.8).$$

Accordingly by introducing a normalized wavenumber w to the cladding region, the solution to the wave equation in this region becomes:

$$\Psi(r, \phi) = BK_q\left(\frac{w}{a}r\right) \begin{pmatrix} \cos q\phi \\ \sin q\phi \end{pmatrix} e^{-ik_z z} \quad (2.9).$$

At this point the substitution of (2.8) to (2.1) can lead to the calculation of the electric and magnetic fields along the z axis in the core region. By moving from Cartesian to cylindrical coordinates one gets the solutions of the form:

$$E_z = \frac{-iA}{\omega\epsilon_2\eta} \left[\frac{u}{a} J'_q\left(\frac{u}{a}r\right) \begin{pmatrix} \cos q\phi \\ \sin q\phi \end{pmatrix} \sin\phi + \frac{q}{r} J_q\left(\frac{u}{a}r\right) \begin{pmatrix} -\sin q\phi \\ \cos q\phi \end{pmatrix} \cos\phi \right] \quad (2.10)$$

$$H_z = \frac{iA}{\omega\mu} \left[\frac{u}{a} J'_q\left(\frac{u}{a}r\right) \begin{pmatrix} \cos q\phi \\ \sin q\phi \end{pmatrix} \cos\phi - \frac{q}{r} J_q\left(\frac{u}{a}r\right) \begin{pmatrix} -\sin q\phi \\ \cos q\phi \end{pmatrix} \sin\phi \right] \quad (2.11).$$

For the cladding region the field equations can be extracted by substituting A with B , u with w , J_n with K_n and J_n' with K_n' in (2.10) and (2.11).

Finally, the use of boundary conditions will define parameters A and B that appear in (2.10) and (2.11). The first boundary condition is the continuity of the wave equation at the core-clad interface which is expressed as $\Psi(a, \phi)_{\text{core}} = \Psi(a, \phi)_{\text{cladding}}$ and leads to: $AJ_q(u) = BK_q(w)$. The second boundary condition is derived by the requirement of equal tangential z -components of the fields at the core-clad interface. This is possible by assuming $\epsilon_1 = \epsilon_2$, which holds true for single mode optical fibers where $n_1 \approx n_2$ (notation 1 and 2 refers to the core and cladding regions respectively). The second boundary condition can be expressed as: $uK_q(w)J'_q(u) = wJ_q(u)K'_q(w)$. These two boundary conditions along with the use of mathematical identities [6], can lead to the waveguiding equation of an optical fiber that is expressed as [6]:

$$u \frac{J_{q-1}(u)}{J_q(u)} = -w \frac{K_{q-1}(w)}{K_q(w)} \quad (2.12).$$

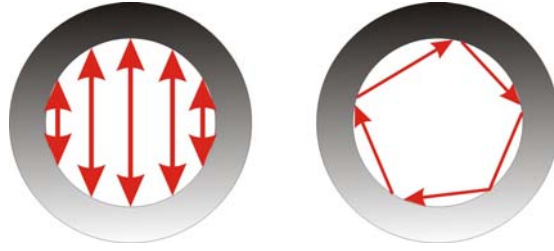


Figure 2.2 Meridian and skew propagation of light inside the fiber core region

If the fiber supports propagation of more than one mode, it is classified as multimode. A single mode fiber can become multimode for wavelengths shorter than the design wavelength, namely the wavelength of operation at which it supports only one mode. The light can propagate inside the fiber by sequential meridian or skew reflections/propagation (Figure 2.2). For the case of meridian propagation of light inside the fiber, the E_z (Transverse Electric, TE) and H_z (Transverse Magnetic, TM) field components equal to zero. In any other case there are hybrid modes propagating inside the optical fiber that have non zero electric and magnetic field components on z axis at the same time. For these cases (i.e. skew propagation) it is necessary to use double indices l, m for the characterization of the propagating mode. These modes are denoted as EH_{lm} or HE_{lm} depending on which of the two field components has a larger projection on the z axis. Examples of HE modes calculated for a step index fiber can be found in Figure 2.3.

For step index fibers with small refractive index differences between core and cladding, light propagation can take place as the superposition of all possible modes of the l^{th} order. This complex propagation mode is characterized as a Linearly Polarized (LP) mode and denoted as LP_{lm} , where l the radial and m the azimuthal order.

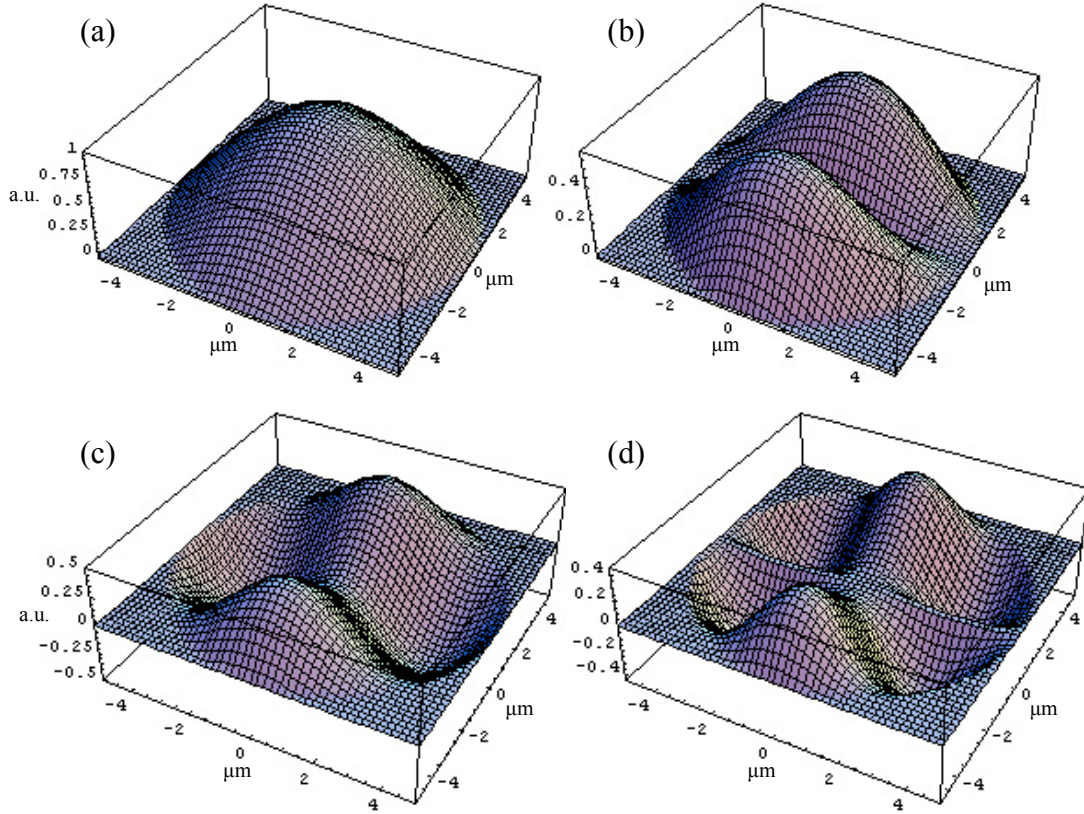


Figure 2.3 HE modes of 900nm radiation propagating through a 5 μ m step index fiber. The four 3-d graphs depict the magnetic field distribution along the core diameter. (a) Fundamental mode LP₀₁ or HE₀₁ (b) HE₁₁ (c) HE₂₁ (d) HE₃₁.

A single mode fiber, such that used in the experiments carried out for this thesis, supports for a specific wavelength the propagation of the fundamental mode LP₀₁. Each mode can be characterized by its propagation constant β_{lm} or its effective index $n_{lm} = \frac{\beta_{lm}}{k}$, where $k = 2\pi/\lambda$ is the vacuum wavenumber and λ is the wavelength.

The value of the effective index specifies the type of mode: $n_{cl} < n_{lm} < n_{co}$ for core modes, $n_{env} < n_{lm} < n_{cl}$ for cladding modes and $0 < n_{lm} < n_{env}$ for radiation modes. Core and cladding modes are discrete, while radiation modes form a continuum. In order to clarify the number of modes that are supported by the fiber core the normalized frequency value of the fiber is needed, defined as:

$$V = k \cdot a \cdot \sqrt{n_{co}^2 - n_{cl}^2} = k \cdot a \cdot NA,$$

where NA refers to the numerical aperture of the fiber. For V values less than 2.405 only the fundamental LP₀₁ mode is supported.

Another useful quantity for the theoretical analysis of optical fibers is the effective index parameter b . The effective index is related to b through:

$$b = (n_{eff}^2 - n_{cl}^2) / (n_{co}^2 - n_{cl}^2).$$

For LP $_{l\mu}$ modes, b is a solution to the dispersion relation [20]

$$V\sqrt{1-b} \frac{J_{l-1}(V\sqrt{1-b})}{J_l(V\sqrt{1-b})} = -V\sqrt{b} \frac{K_{l-1}(V\sqrt{b})}{K_l(V\sqrt{b})} \quad (2.13)$$

where l is the azimuthal order of the mode. Once V and b are known, the confinement factor Φ can be determined from [7]

$$\Phi = \frac{b^2}{V^2} \left[1 - \frac{J_l^2(V\sqrt{1-b})}{J_{l+1}(V\sqrt{1-b})J_{l-1}(V\sqrt{1-b})} \right]. \quad (2.14)$$

Confinement factor Φ is an indication of the extension of the propagating mode of interest outside the core boundaries. For example a mode with a confinement factor of 85% means that 15% of the mode's power is propagating outside the core region.

2.1.2 Microstructured Optical Fibers

The geometry and light propagation principles of microstructured optical fibers (MOFs) are different from those of conventional optical fibers. There are several types of microstructured optical fibers, such as hollow core fibers, large mode area fibers and highly non linear. For the purposes of this thesis, solid core, endlessly single mode photonic crystal fibers will be examined, as these were the only used in Bragg grating inscriptions.

Microstructured Optical Fibers can be divided into two major classes, the index-guiding or high index core fibers and the photonic bandgap or low index core fibers. These two classes have different guiding properties. The waveguiding principle of the high index core fibers may be expressed as modified total internal reflection (MTIR) [9]. The low index core fibers guide light in their core by trapping it through the photonic bandgap that is formed from the capillary array [9]. The core in the high index core fiber class, as its name suggests, has an averagely higher effective refractive index than the surrounding cladding material. The most common way of realizing this, is to introduce an array of capillaries to the cladding region of the fiber. Since the manufacturing material of the fiber is the same throughout the whole of the fiber diameter, the array of holes lowers the effective refractive index of the cladding

region. This way the light is guided inside the core in a way similar to the total internal reflection guidance of step-index fibers (Figure 2.4)

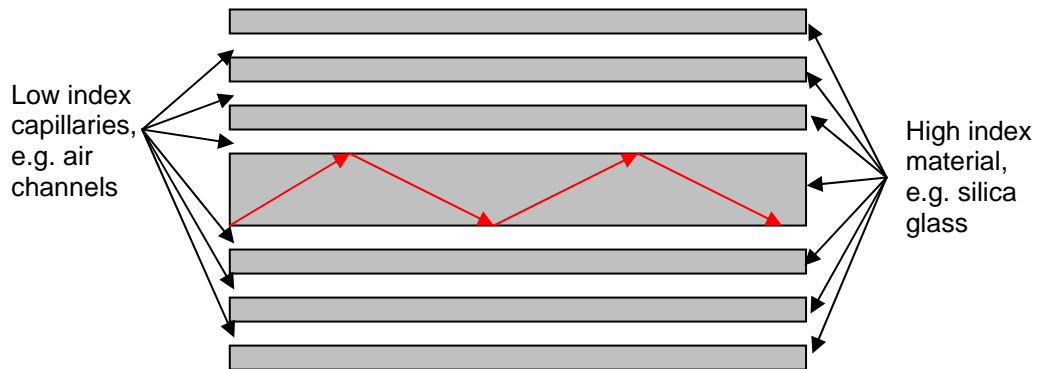


Figure 2.4 Light propagation in a high index core MOF. Grey areas: High index region. White areas: Low index regions. Red arrows: Propagating beam

The structure of such a high-index solid core microstructured optical fiber (MOF) is presented in Figure 2.5. The particular sketch refers to a fiber that is commercially available and it is the one used in the experiments carried out for this thesis. A SEM scan of a cross section of this fiber is presented in the inset of Figure 2.4. This type of MOFs is characterized by triangular arranged cladding holes. The relative size of the cladding-hole d/Λ_h may range for this class of fibers from a few percent up to around 90%. Λ_h is the center to center capillary spacing, ranging from around a micron up to $20\mu\text{m}$ and d is the capillary diameter with typical values from a micron up to tens of microns. The solid core of the fiber is made of the same material as the rest of the fiber and does not usually contain any dopants. The size of the core typically lies in the range of $5 - 20\mu\text{m}$. Commercial MOFs are usually made of low-loss, high-purity silicate glass [8]. By adjusting the geometrical features of the fibers one can adjust the light propagation properties from highly linear performance to highly non-linear propagation.

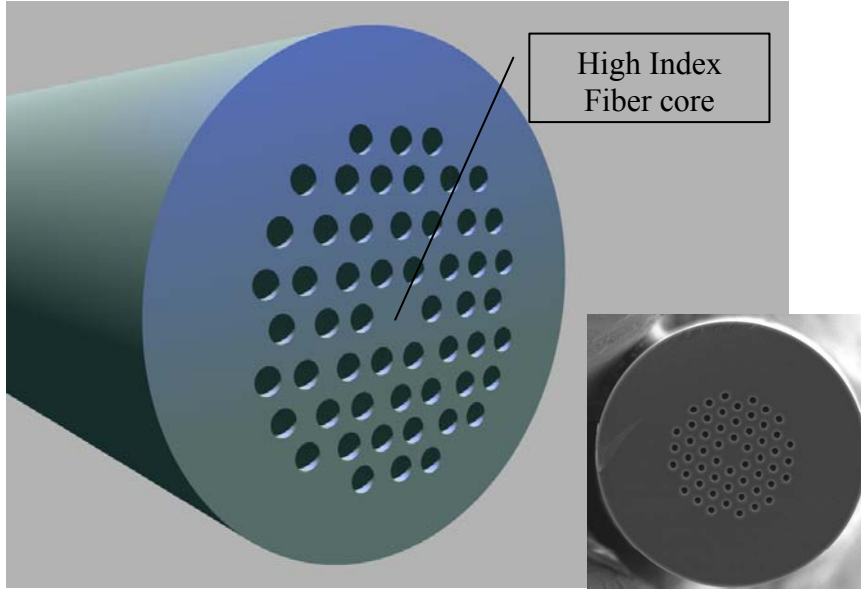


Figure 2.5 High Index Core Microstructured Optical Fiber layout (size of the air holes exaggerated for illustration purposes) . Inset: SEM scan of ESM-12-01 from Crystal Fibre.

In order to model the light propagation of these fibers Birks, *et al*, [10] proposed the effective index approach. In this model the cladding containing the air holes are given an effective refractive index value (based on the approximate waveguiding properties of the cladding) and the resultant structure has a refractive index value n_{cl} and the core n_{co} , reducing the problem to the simplicity of a step index fiber. The simplicity of this method though is reflected as inaccuracy in the resulting mode profiles and it is not popular for MOF mode calculations.

A more precise approach on the light propagation modeling is the full-vectorial plane wave expansion method. It was the first method to accurately analyze photonic crystals [11-12]. This method solves the full vector wave equation for the magnetic and/or the electric field by expanding the plane-wave of the field and the dielectric constant, which is varying with position [9]. It is possible to calculate the photonic band diagram of a photonic crystal and consequently the existence of photonic bandgaps. This method can be applied to one-, two-, and three-dimensional problems, due to its general nature. Briefly in this method, for photonic crystals assumed to be linear, isotropic, non-magnetic and non-absorbing the position dependent E and H fields of angular frequency ω may be expressed as:

$$\begin{aligned}\bar{E}(\bar{r}, t) &= \bar{E}(\bar{r})e^{j\omega t} \\ \bar{H}(\bar{r}, t) &= \bar{H}(\bar{r})e^{j\omega t}\end{aligned}\quad (2.15)$$

By using equations (2.15), a single equation describing the electromagnetic wave

propagation can be deduced, known as the wave equation. For the case of the electric field the wave equation becomes:

$$\nabla \times \nabla \times \bar{E}(\bar{r}) = \frac{\omega^2}{c^2} \varepsilon(\bar{r}) \bar{E}(\bar{r}) \quad (2.16)$$

and for the magnetic field the wave equation reads:

$$\nabla \times \left[\frac{1}{\varepsilon(\bar{r})} \nabla \times \bar{H}(\bar{r}) \right] = \frac{\omega^2}{c^2} \bar{H}(\bar{r}) \quad (2.17),$$

where $\varepsilon(\bar{r})$ is the relative dielectric constant and c is the speed of light in vacuum. Due to the fact that photonic crystals are periodic structures, one of the above two wave equations' (2.16),(2.17) solutions may be expressed as a plane wave modulated by a function with the periodicity of the photonic crystal, by taking advantage of the Bloch's theorem:

$$\bar{E}(\bar{r}) = \bar{V}_k(\bar{r}) e^{-j\bar{k} \cdot \bar{r}} \quad (2.18)$$

$$\bar{H}(\bar{r}) = \bar{U}_k(\bar{r}) e^{-j\bar{k} \cdot \bar{r}} \quad (2.19)$$

where $\bar{V}_k(\bar{r})$, $\bar{U}_k(\bar{r})$ are the periodic functions and k is the k vector of the solution. For the determination of the solutions it is useful to work in the reciprocal space and express the periodic functions as a Fourier series expansion in terms of the reciprocal lattice vectors, \bar{G} :

$$\bar{E}(\bar{r}) = \sum_{\bar{G}} \bar{E}_{\bar{k}}(\bar{G}) e^{-i(\bar{k} + \bar{G}) \cdot \bar{r}} \quad (2.20)$$

$$\bar{H}(\bar{r}) = \sum_{\bar{G}} \bar{H}_{\bar{k}}(\bar{G}) e^{-i(\bar{k} + \bar{G}) \cdot \bar{r}} \quad (2.21)$$

Finally, by applying the Fourier transformation to (2.18) and (2.19) the resultant equations are:

$$-(\bar{k} + \bar{G}) \times [(\bar{k} + \bar{G}) \times \bar{E}_{\bar{k}}(\bar{G})] = \frac{\omega^2}{c^2} \sum_{\bar{G}'} \varepsilon_r(\bar{G} - \bar{G}') \bar{E}_{\bar{k}}(\bar{G}') \quad (2.22)$$

$$-(\bar{k} + \bar{G}) \times \left[\sum_{\bar{G}'} \varepsilon_r^{-1}(\bar{G} - \bar{G}') (\bar{k} + \bar{G}') \times \bar{H}_{\bar{k}}(\bar{G}') \right] = \frac{\omega^2}{c^2} \bar{H}_{\bar{k}}(\bar{G}) \quad (2.23),$$

where $\varepsilon_r(\bar{E})$ and $\varepsilon_r^{-1}(\bar{E})$ are the Fourier coefficients of $\varepsilon_r(\bar{r})$ and $\varepsilon_r^{-1}(\bar{r})$. These coefficients can vary in value depending on the geometry of the problem. Subscript k denotes that the eigenvalue problem is solved for a fixed wave vector to find the angular frequencies of all allowed propagating modes. Equations (2.22) and (2.23) may be expressed in matrix form and solved using numerical methods.

Along with the full vectorial plane wave approximation method there are numerous other methods for modeling MOFs. Amongst them is the biorthonormal basis method developed by Silvestre, *et al*, [13], the multipole method [14], the Fourier decomposition method [15], the finite difference methods [16-17], the finite element method [18], beam propagation method [19] and the equivalent averaged index method [15].

Throughout this thesis, two computer softwares were used for the calculation of propagation mode profiles inside MOFs. The first is based on the multipole method [14] and the second on the finite difference time difference domain methods [16]. The program based on the multipole method is the freeware CUDOS MOF Utilities [26], by the University of Sydney [25]. Among the capabilities of this software is the calculation of MOF modes, their dispersion curves, their field distribution, their structural losses and their effective area. The second program used was the OptiFDTD® version 7 from Optiwave® software [27]. This software is based on the finite difference time difference domain method [16] and features the Uniaxial perfectly matched layer (UPML) technique for boundary conditions [28]. Using OptiFDTD it is possible to design, analyze and test modern passive and nonlinear photonic components for wave propagation, scattering, reflection, diffraction, polarization and the nonlinear phenomena. Simulation of propagating modes of 1.52 μm light inside the ESM-12-01 MOF is presented in Figures 2.6a through e. Figure 2.6e was calculated using the CUDOS MOF Utilities and the previous 4 using the OptiFDTD software. The CUDOS MOF Utilities resulted in singularities when prompted to calculate higher order modes in the MOF fiber and thus no higher order results obtained with this approach are presented here.

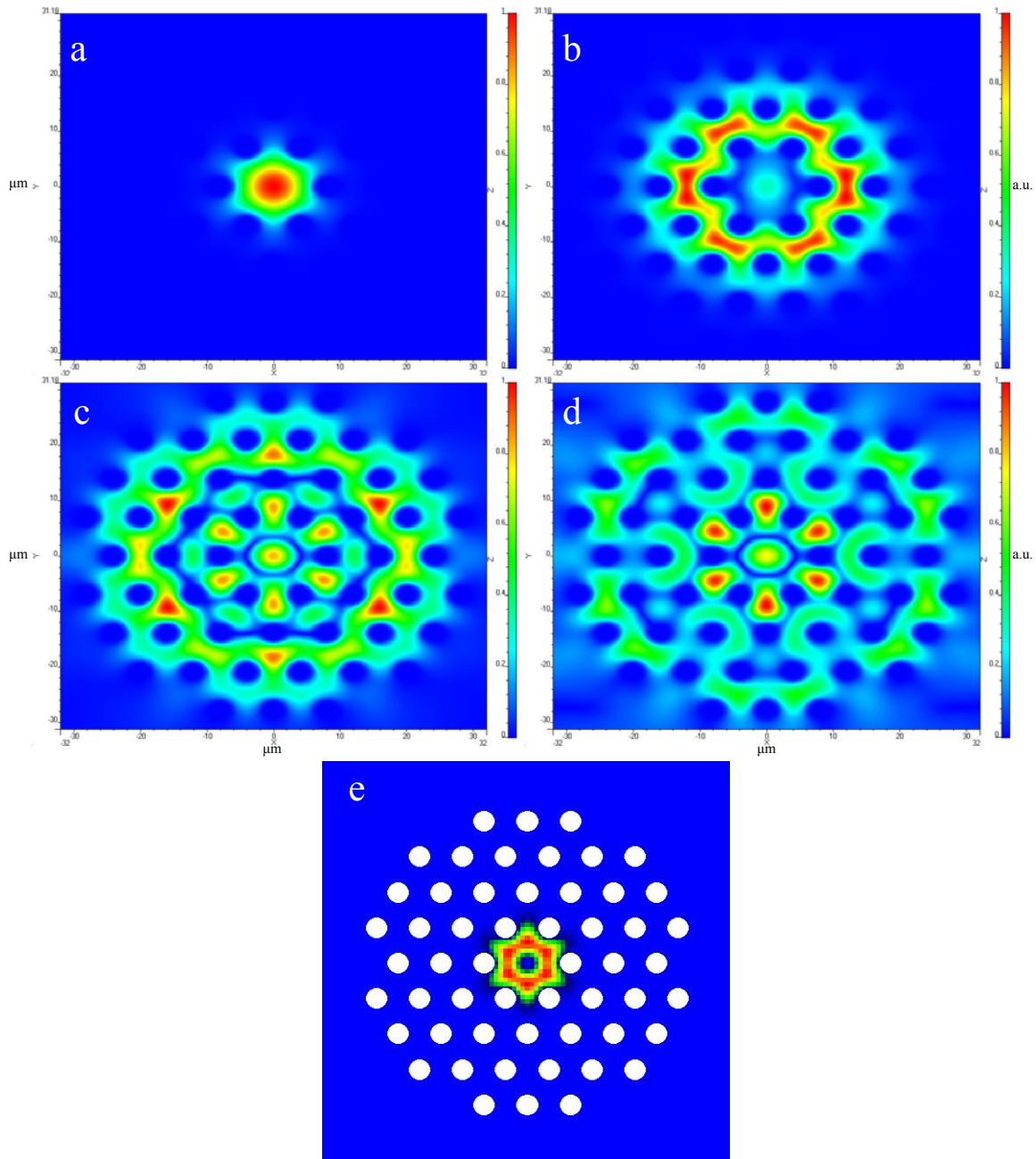


Figure 2.6 Z-axis Poynting vector profile of: (a) 1st supported mode for ESM-12-01 at 1.52 μm , (b) 2nd mode, (c) 3rd mode and (d) 4th mode, as calculated by the OptiFDTD® program [27]. There is no fifth supported mode for this wavelength. (e) 1st supported mode for the same fiber at 1.52 μm as calculated by the CUDOS MOF Utilities (fiber capillaries shown) [25]

Similar to standard optical fibres, the high-index core MOFs will always support at least one index-guided mode. However, it is possible to design endlessly single mode MOFs, namely MOFs that will support only one (the fundamental) propagation mode over a large range of frequency. This unique ability of the MOFs was first explained by Birks, *et al*, [10] using the effective index approach for the cladding structure. For conventional step index fibres the number of guided modes is determined by the value of the normalised frequency V that was defined as:

$$V_{\text{eff}} = k \cdot a \sqrt{n_{\text{co}}^2 - n_{\text{cl}}^2} = \frac{2\pi}{\lambda} a \sqrt{n_{\text{co}}^2 - n_{\text{cl}}^2} \quad (2.24),$$

where a is the core radius. The difference with the conventional step index fibers is that for MOFs the V value can be stabilized to a fixed value in the high frequency regime. This can be observed in Figure 2.7, where the V_{eff} value is saturated in the high frequency regime. This behavior originates from the strong wavelength dependence of the cladding's effective refractive index. Different spacing between the air holes and different hole sizes can greatly affect the effective refractive index of the cladding region, resulting in the above-mentioned wavelength dependence. As the frequency is increased the effective index of the cladding n_{cl} is approaching n_{co} and equation (2.24) can reach a stationary value (visible for large normalized frequency values in Figure 2.7). This value is determined by the ratio of the capillary diameter d to the period of the lattice Λ_h and increases with the ratio as seen in Figure 2.7. This way it is possible to design MOFs with d/Λ_h below a certain value, ensuring that the V_{eff} value does not exceed the second order mode cutoff value over the desired wavelength range. The result of such a design would be an endlessly single mode operation of the fiber over a specific wavelength range. Such a design possibility is not applicable to conventional fibers, because their cladding refractive index is largely wavelength independent.

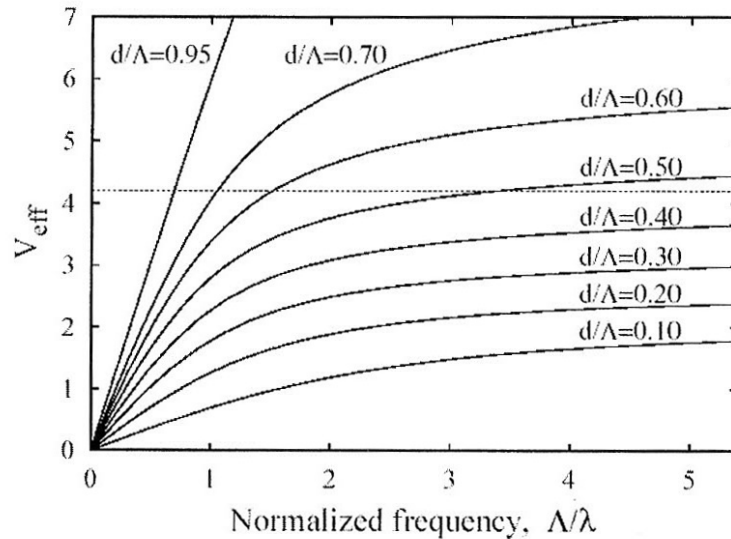


Figure 2. 7 Effective V-values versus normalized frequency for various cladding-hole diameter over spacing ratios (after [9])

The possibility to use the normalised frequency (V) in both MOFs and step index fibers will be used to derive the Bragg grating formalising for both types of fibers.

2.2 Coupled mode theory

Coupled mode equations and coupled mode theory are the most commonly used tools for quantitative simulation of reflection and transmission gratings in fibers or bulks [7,21]. They can be applied to uniform [7], non-uniform [7], chirped [21], apodized [21] and tilted [21] gratings providing results in good agreement with experimental observations. The accuracy of this method lies in the fact that refractive index changes are small compared to the refractive index value, which is true for most types of gratings and true for all gratings inscribed for this thesis work. Coupled mode theory treats the photoinduced refractive index change of the fiber as a perturbation which couples together the modes of the unperturbed fiber. The optical properties of a fiber grating are defined by the variation of the induced index change δn_{eff} along the fiber axis z (the light propagation axis). For the purposes of this work only the cases of uniform reflection gratings will be examined, as the gratings experimentally inscribed belong to this category. In the analysis that follows two assumptions are made. First, the envelopes of the mode amplitudes are slowly varying in z and second, the optical fields are expressed as scalar quantities. The above approximations are used globally and introduce very small errors for most cases, but are absolutely necessary for an analytical approach to this problem.

The first step to this analysis is to define the effective refractive index that was the result of the UV irradiation process. The effective refractive index refers to the guided modes of interest and is described by the equation

$$\delta n_{\text{eff}}(z) = \overline{\delta n_{\text{eff}}}(z) \left\{ 1 + u \cos\left[\frac{2\pi}{\Lambda} z + \phi(z)\right] \right\} \quad (2.25)$$

where $\overline{\delta n_{\text{eff}}}$ is the “dc” index change spatially averaged over a grating period, u is the fringe visibility of the index change, Λ is the grating period, and $\phi(z)$ describes grating chirp. It is assumed for the case of step index fibers, that the grating formation takes place only in the fiber core. However the propagating mode field is probable to extend outside the core boundaries, so in order to be precise on the modulated index calculation the mode confinement factor in the core must be considered. For a step index profile and an induced index change δn_{co} uniformly distributed across the core, the effective index change is defined as:

$$\delta n_{\text{eff}} = \Phi \delta n_{\text{co}},$$

where Φ is the core power confinement factor for the mode of interest.

Before stepping to the quantitative analysis using coupled mode theory, a qualitative picture of the basic interactions of the two modes that couple together will be examined. The fiber grating is an optical diffraction grating and can be described by the grating equation [22]:

$$n \sin \theta_2 = n \sin \theta_1 + m \frac{\lambda}{\Lambda} \quad (2.26)$$

where θ_2 is the angle of the diffracted wave, θ_1 is the incidence angle of the light wave and the integer m determines the diffraction order (Figure 2.8). This equation can be used to predict the angle(s) $\theta_{2(m)}$ where constructive interference occurs and the wavelength of maximum light coupling efficiency between two modes.

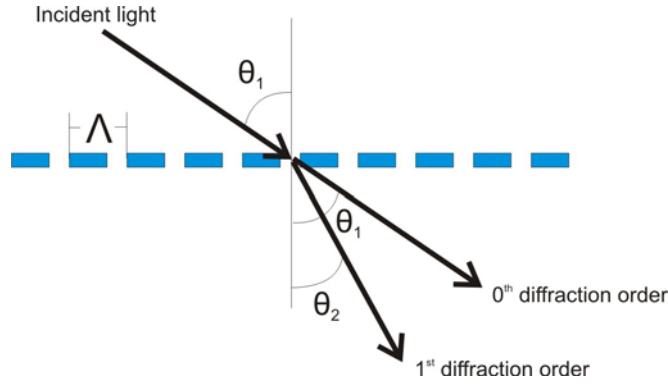


Figure 2.8 Diffraction of light by a grating

Figure 2.9 illustrates reflection by a Bragg grating. The forward propagating mode has an angle of incidence θ_1 and the backwards propagating mode an angle $\theta_2 = -\theta_1$. Equation (2.26) can be rewritten as for the guided modes:

$$\beta_2 = \beta_1 + m \frac{2\pi}{\Lambda} \quad (2.27)$$

using the fact that the propagation constant β is: $\beta = (2\pi/\lambda)n_{\text{eff}}$,

where $n_{\text{eff}} = n_{\text{co}} \sin \theta$.

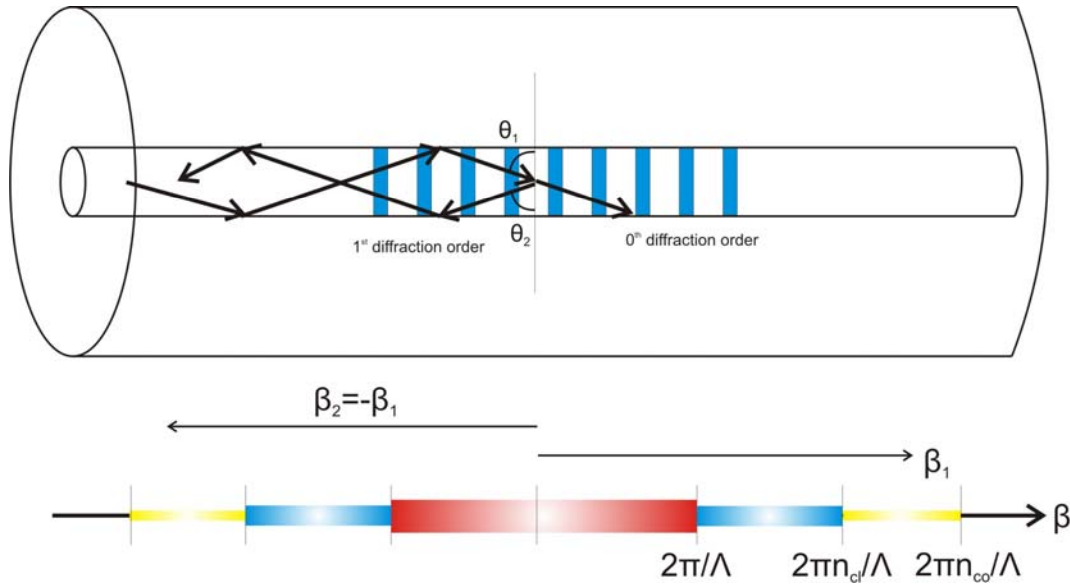


Figure 2.9 Bragg grating reflection inside optical fiber

The back reflection of the first diffraction order ($m = \pm 1$) is illustrated in Figure 2.9. The propagation constant value of the back reflected mode (β_2) lays in the $2\pi n_{cl}/\Lambda - 2\pi n_{co}/\Lambda$ region (where any other bound core modes will be found, if they exist - thin yellow region in the propagation constant diagram of Figure 2.9). Any cladding modes will have propagation constant values located in the $2\pi/\Lambda - 2\pi n_{cl}/\Lambda$ region (cladding modes – medium blue region in the propagation constant diagram). A mode with propagation constant of value less than $2\pi/\Lambda$ is a radiation mode exiting the fiber hyperstructure (thick red region in the propagation constant diagram of Figure 2.9). Negative β values refer to modes that propagate in the $-z$ direction. Using equation (2.27) it is possible to calculate the resonant wavelength of reflection of a mode of index $n_{eff,1}$ into a mode of index $n_{eff,2}$.

$$\lambda = (n_{eff,1} + n_{eff,2})\Lambda. \quad (2.28)$$

If the two modes are identical, the resultant equation is:

$$\lambda = 2n_{eff}\Lambda,$$

as presented in Chapter 1.

At this point it is useful to proceed to the quantitative analysis of Bragg gratings. Derivation of coupled mode theory is not presented here, but can be easily found in the literature [23-24].

In the ideal – mode approximation to coupled mode theory, it is assumed that the transverse component of the electric field can be written as a superposition of the

ideal modes labeled j (i.e. the modes in an ideal waveguide with no grating perturbation). The electric field can be written then as:

$$\vec{E}_t(x, y, z, t) = \sum_j [A_j(z) \exp(i\beta_j z) + B_j(z) \exp(-i\beta_j z)] \cdot \vec{e}_{jt}(x, y) \exp(i\omega t) \quad (2.29)$$

where $A_j(z)$ and $B_j(z)$ are slowly varying amplitudes of the j^{th} mode traveling in the $+z$ and $-z$ directions, respectively. The transverse mode fields $\vec{e}_{jt}(x, y)$ can describe the bound-core LP, the cladding modes, or the radiation modes. The presence of a dielectric perturbation (grating structure) causes the modes to be coupled such that the amplitudes A_j and B_j of the j^{th} mode evolve along the z axis according to

$$\frac{dA_j}{dz} = i \sum_k A_k (K_{kj}^t + K_{kj}^z) \exp[i(\beta_k - \beta_j)z] + i \sum_k B_k (K_{kj}^t + K_{kj}^z) \exp[-i(\beta_k + \beta_j)z] \quad (2.30)$$

$$\frac{dB_j}{dz} = -i \sum_k A_k (K_{kj}^t - K_{kj}^z) \exp[i(\beta_k + \beta_j)z] - i \sum_k B_k (K_{kj}^t + K_{kj}^z) \exp[-i(\beta_k - \beta_j)z] \quad (2.31)$$

In the above two equations (2.30) and (2.31), $K_{kj}^t(z)$ is the transverse coupling coefficient between modes j and k given by

$$K_{kj}^t(z) = \frac{\omega}{4} \iint_{\infty} dx dy \Delta \varepsilon(x, y, z) \vec{e}_{kt}(x, y) \cdot \vec{e}_{kj}^*(x, y) \quad (2.32)$$

where $\Delta \varepsilon$ is the perturbation to the permittivity, approximately $\Delta \varepsilon \approx 2n\delta n$ when $\delta n \ll n$. The longitudinal coefficient $K_{kj}^z(z)$ is analogous to $K_{kj}^t(z)$, but generally $K_{kj}^z(z) \ll K_{kj}^t(z)$ for low order guiding fiber modes, and this coefficient can be neglected in the most of cases.

For the sake of mathematical simplification the fiber gratings that will be analyzed are supposed to have uniform induced index change $\delta n(x, y, z)$ across the core and nonexistent outside the core. Although this does not hold true for the experimentally inscribed gratings, it greatly simplifies the solution of the problem. The extend of error that this assumption adds can be estimated by taking into account the confinement factor of the interacting modes during Bragg reflection. The higher the confinement factor of the modes the less the error added.

With this assumption the core index can be described by an expression similar to (2.25), but with $\overline{\delta n_{eff}}(z)$ replaced by $\overline{\delta n_{co}}(z)$, since no index modulation takes place outside the core boundaries. By defining two new coefficients:

$$\sigma_{kj}(z) = \frac{\omega n_{co}}{2} \overline{\delta n_{co}}(z) \iint_{core} dx dy \vec{e}_{kt}(x, y) \cdot \vec{e}_{jt}^*(x, y) \quad (2.33)$$

$$\kappa_{kj}(z) = \frac{u}{2} \sigma_{kj}(z) \quad (2.34)$$

where σ is a “dc” (period-averaged) coupling coefficient and κ is an “AC” coupling coefficient, the general coupling coefficient can be written

$$K'_{kj}(z) = \sigma_{kj}(z) + 2\kappa_{kj}(z) \cos\left[\frac{2\pi}{\Lambda}z + \phi(z)\right]. \quad (35)$$

Equations (2.30)-(2.35) are the coupled-mode equations that will be used to simulate fiber-grating spectra in the following section. The (2.33) and (2.34) are the overlap integrals of the grating coupling constant.

2.3 Uniform Bragg gratings

When a single mode of amplitude $A(z)$ is reflected into an identical mode propagating in the opposite direction with amplitude $B(z)$, equations (2.30) and (2.31) can be simplified, as suggested by Koglenik [24]. This simplification is possible by omitting terms that include the amplitude of other modes (right hand side of equations (2.30) and (2.31)). This is the “synchronous approximation”. The resulting equations are:

$$\frac{dR}{dz} = i\hat{\sigma}R(z) + i\kappa S(z) \quad (2.36)$$

$$\frac{dS}{dz} = i\hat{\sigma}S(z) - i\kappa^*R(z) \quad (2.37)$$

where the amplitudes R and S are $R(z) \equiv A(z)\exp(i\delta z - \varphi/2)$ and $S(z) \equiv B(z)\exp(-i\delta z + \varphi/2)$. In these equations κ is the “AC” coupling coefficient from (2.34) and $\hat{\sigma}$ is a general “dc” self-coupling coefficient defined as

$$\hat{\sigma} \equiv \delta + \sigma - \frac{1}{2} \frac{d\phi}{dz}. \quad (2.38)$$

The detuning δ can be defined as

$$\delta \equiv \beta - \frac{\pi}{\Lambda} = \beta - \beta_D = 2\pi n_{eff} \left(\frac{1}{\lambda} - \frac{1}{\lambda_D} \right) \quad (2.39)$$

where $\lambda_D \equiv 2n_{eff}\Lambda$ is the “design wavelength” of a Bragg grating with a period of Λ . Absorption loss in the grating can be described by a complex coefficient σ , where the power loss coefficient is $\alpha = 2\text{Im}(\sigma)$. Finally, the derivative $\frac{1}{2}d\phi/dz$ describes possible chirp of the grating period, where $\phi(z)$ is defined using (2.25) or (2.35).

For a single mode Bragg reflection grating, the following simple relations are found:

$$\sigma = \frac{2\pi}{\lambda} \overline{\delta n_{eff}} \quad (2.40)$$

$$\kappa = \kappa^* = \frac{\pi}{\lambda} u \overline{\delta n_{eff}} \quad (2.41)$$

If the grating is uniform along z , then $\overline{\delta n_{eff}}$ is a constant and $d\phi/dz = 0$ (no chirping), and thus κ , σ , and $\hat{\sigma}$ are constants. Thus, (2.36) and (2.37) are coupled first-order ordinary differential equations with constant coefficients, for which solutions can be found when appropriate boundary conditions are specified. The reflectivity of a uniform fiber grating length L can be found by assuming a forward going wave incident from $z = -\infty$ (say $R(-L/2) = 1$) and requiring that no backward-going wave exists for $z \geq L/2$ (i.e., $S(L/2)=0$). The amplitude and power reflection coefficients $\rho = S(-L/2)/R(-L/2)$ and $r = |\rho|^2$, respectively, can then be shown to be [23], [24]

$$\rho = \frac{-\kappa \sinh(\sqrt{\kappa^2 - \hat{\sigma}^2} L)}{\hat{\sigma} \sinh(\sqrt{\kappa^2 - \hat{\sigma}^2} L) + i\sqrt{\kappa^2 - \hat{\sigma}^2} \cosh(\sqrt{\kappa^2 - \hat{\sigma}^2} L)} \quad (2.42)$$

and

$$r = \frac{\sinh^2(\sqrt{\kappa^2 - \hat{\sigma}^2} L)}{\cosh^2(\sqrt{\kappa^2 - \hat{\sigma}^2} L) - \frac{\hat{\sigma}^2}{\kappa^2}} \quad (2.43)$$

A number of interesting features of fiber Bragg gratings can be seen from these results. Typical examples of the power reflectivity r for uniform gratings with $\kappa L = 2$ and $\kappa L = 6$ are shown in Figure 2.10, plotted versus the normalized wavelength:

$$\frac{\lambda}{\lambda_{max}} = \frac{1}{1 + \frac{\hat{\sigma} L}{\pi N}} \quad (2.44)$$

where N is the total number of grating periods ($N = L/\Lambda$), here chosen to be $N = 7476$

(1073.5nm phase mask pitch and 4mm grating) and λ_{\max} is the wavelength at which maximum reflectivity occurs. From (2.43) maximum reflectivity r_{\max} for a Bragg grating is found to be:

$$r_{\max} = \tanh^2(\kappa L)$$

and it occurs when $\hat{\sigma} = 0$, or at the wavelength

$$\lambda_{\max} = \left(1 + \frac{\overline{\delta n_{eff}}}{n_{eff}} \right) \lambda_D. \quad (2.45)$$

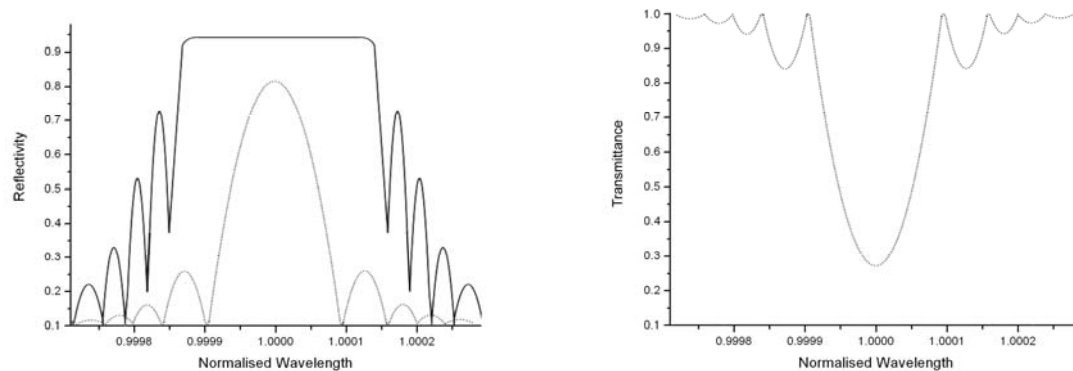


Figure 2.10 (a) Calculated reflectivity of a uniform Bragg grating with $\kappa L=2$ (dotted line) and $\kappa L=10$ (solid line) and calculated transmission of a uniform Bragg grating with $\kappa L=2$, (b) Transmittance of the uniform Bragg grating with $\kappa L=2$

2.4 Conclusions

In this chapter some of the basic propagation properties of both step index and microstructured optical fibers were discussed. It was demonstrated that some basic operations in high-index, solid core microstructured optical fibres can be described by using expressions based on step index fibre theory. This analogy between step index and PCF can be further expanded to include the tools that were described for the quantitative analysis of Bragg gratings. These tools, namely the coupled wave equations gave off quantitative tools for the design and the calculation of in-fibre Bragg gratings. Although the extraction of these tools required simplifying assumptions, these affect calculations referring to higher order modes largely extended outside the fibre core region.

References

- [1] A. Dragomir, D.N. Nikogosyan and G. Brambilla, “Increased photosensitivity of Ge-doped and Ge, Sn-doped fibres under high-intensity 264 nm laser light”, *Electronics Letters* **39**: 1437–1438, (2003)
- [2] C.W. Haggans, W.F. Varner, J-S. Wang, US patent No. 6058231, (2000)
- [3] Maurer and Schultz, US patent No. 3659915, Corning Glass Inc., (1972)
- [4] S.N. Kapany, “Fiber Optics”, Academic Press, New York, (1967).
- [5] J.D. Kraus, D.A. Fleisch, “Electromagnetics with Applications”, McGraw Hill International Editions, International Edition, (1999).
- [6] D.L. Lee, “Electromagnetic Principles of Integrated Optics”, John Wiley and Sons, International Edition, (1988).
- [7] T. Erdogan, “Fiber Grating Spectra”, *Journal of Lightwave Technology*, **15** : 1277 – 1294, (Review Article), (1997)
- [8] B.J. Eggleton, C. Kerbage, P.S. Westbrook, R.S. Windeler, A. Hale, “Microstructured Optical fibre devices”, *Optics Express*, **9**: 698-713, (2001).
- [9] A. Bjarklev, J. Broeng, A.S. Bjarklev, “Photonic Crystal Fibers”, Kluwer Academic Publishers, International Edition, (2003)
- [10] J. C. Knight, T. A. Birks, P. St. J. Russell, and J. P. Sandro, “Properties of photonic crystal fiber and the effective index model,” *J. Opt. Soc. Am. A*, vol. 15, 748, (1998).
- [11] K. Leung, Y. Liu, “Full vector wave calculation of photonic band structures in face-centred-cubic dielectric media”, *Physical Review Letters*, **65**: 2646-2649, (1990).
- [12] Z. Zhang, S. Satpathy, “Electromagnetic wave propagation in periodic structures: Bloch wave solution of Maxwell’s equations”, *Physical Review Letters*, **65**: 2650-2653, (1990).
- [13] E. Silvestre, M.V. Andres, P. Andres, “Biorthonormal basis method for the vector description of optical fibre modes”, *IEEE Journal of Lightwave Technology*, **16**: 923-928, (1998).
- [14] T.P. White, R.C. McPhedran, L.C. Botten, G.H. Smith, C.M. de Sterke, “Calculations of air-guided modes in photonic crystal fibers using the multipole method”, *Optics Express*, **11**: 721-732 (2001)

- [15] L. Poladian, N.A. Isan, T.M. Monro, “Fourier decomposition algorithm for leaky modes of fibres with arbitrary geometry”, *Optics Express*, **10**: 449-454, (2002)
- [16] M. Qiu, “Analysis of guided modes in photonic crystal fibers using the finite-difference time-difference domain method”, *Microwave and Optical Technology Letters*, **30**:327-330, (2001)
- [17] Z. Zhu, T.G. Brown, “Full vectorial finite-difference analysis of microstructured optical fibers”, *Optics Express*, **10**: 853-864, (2002)
- [18] F. Brechet, J. Marcou, D. Pangoux, P. Roy, “Complete analysis of the characteristics of propagation into photonic crystal fibers by the finite element method”, *Optical Fiber Technology*, **6**: 181-191, (2000)
- [19] B.J. Eggleton, P.S. Westbrook, R.S. Windeler, S. Spalter, T.A. Strasser, “Grating resonances in air/silica micro structured optical fibers”, *Optics Letters*, **24**: 1460-1462, (1999)
- [20] D. Marcuse, “Theory of Dielectric Optical Waveguides”, New York: Academic, (1991)
- [21] A. Othonos and K. Kalli, “Fiber Bragg gratings”, Artech House Inc., London, (1999)
- [22] M. Born, E. Wolf, “Principles of Optics”, New York: Pergamon, (1987)
- [23] A. Yariv, “Coupled-mode theory for guided-wave optics,” *IEEE Journal of Quantum Electron*, **QE-9**:919–933, (1973)
- [24] H. Kogelnik, “Theory of optical waveguides,” in T. Tamir’s “Guided-Wave Optoelectronics”, Springer-Verlag, International Edition, (1990)
- [25] <http://www.physics.usyd.edu.au/cudos/mofsoftware/>
- [26] T. P. White, B. T. Kuhlmey, R. C. McPhedran, D. Maystre, G. Renversez, C. Martijn de Sterke, L. C. Botten, “Multipole method for microstructured optical fibers I : formulation”, *Journal of the Optical Society of America B*, **19**: 2322-2330, (2002).
- [27] <http://www.optiwave.com/site/products/fdtd.html>
- [28] S.D. Gedney, “An anisotropic perfectly matched layer absorbing media for the truncation of FDTD lattices”. *IEEE Transactions on Antennas and Propagation*, **44**: 1630–1639, (1996)

3. Photosensitivity of silicate glass optical fibres

Photosensitivity in optical materials refers to the change of the physical properties of the dielectric material (refractive index, density, micro-structure, etc.) under exposure to laser radiation with specific wavelength, intensity, pulse duration and energy density. The chemical composition and structure (amorphous, crystalline, etc.) of the optical material are few of the dominant factors defining its intrinsic photosensitivity. In addition the response of the optical material under exposure to the incident laser light depends on the laser beam intensity, wavelength, energy density and exposure dose. Irradiation of a photosensitive optical material can cause changes to its refractive index, density, structure, phase changes, ablation, or local melting, among other effects. Although photosensitivity is not a directly measured quantity, it can be estimated by measuring the photoinduced changes after irradiation. This way, techniques such as microscopy (i.e. SEM, AFM, optical, infrared, Raman microscopy), optical techniques (i.e. refractometry, diffraction efficiency measurements), mechanical testing (i.e. material hardness), or indirect methods (like the reflectivity measurement of the grating of in-fiber Bragg grating inscriptions) can be utilized for measuring the changes induced by the laser light.

Grating recording of devices developed in fibers and bulks is largely based on laser photosensitivity processes. Therefore, the study of laser photosensitivity has a direct impact on the development of functional photonic devices. It was initially believed that only fibers with germanosilicate glass exhibited photosensitivity [1], [2], but it was later discovered that Bragg grating inscription is also possible in optical fibers containing other dopants or no dopants at all.

3.1 Photosensitivity of optical fibers with different core compositions

Photosensitivity in optical fibers is highly affected by the core dopants, preconditioning, prior thermal treatment, the incident laser radiation wavelength, intensity and energy density, among other factors. Dopants can induce different absorption bands, creating a number of pre-existing defects that can be exploited for enhancing photosensitivity (color centers). In this section a brief discussion of the

photosensitivity mechanism, in fibers with different co-dopants, or no dopants, will follow.

3.1.1 Ge-doped silicate glass optical fibers

Silicon oxide tetrahedra in glass do not exhibit microscopic order and form an amorphous structure. Since Germanium has the same valence as Silicon, the former easily replaces the later in vitreous structures. The addition of Ge inside the fiber silica core introduces to the glass absorption bands located principally at 195nm and 242nm [3-4]. Russell and Hand attribute the 242nm band to oxygen deficient defects of the $\text{GeO}_2\text{-SiO}_2$ matrix, known as Germanium–Oxygen Deficiency Centers (GODCs) [5]. These centers are formed in two types of structures (Figure 3.1). The first one is the neutral oxygen vacancy (NOV) structure which consists of a germanium atom having a silicon or germanium nearest neighbor (Figure 3.1a) and in the second structure the germania molecule is in the reduced state GeO with the germanium atom being bonded to only two oxygens and is left with a lone pair of electrons (Figure 3.1b) [3].

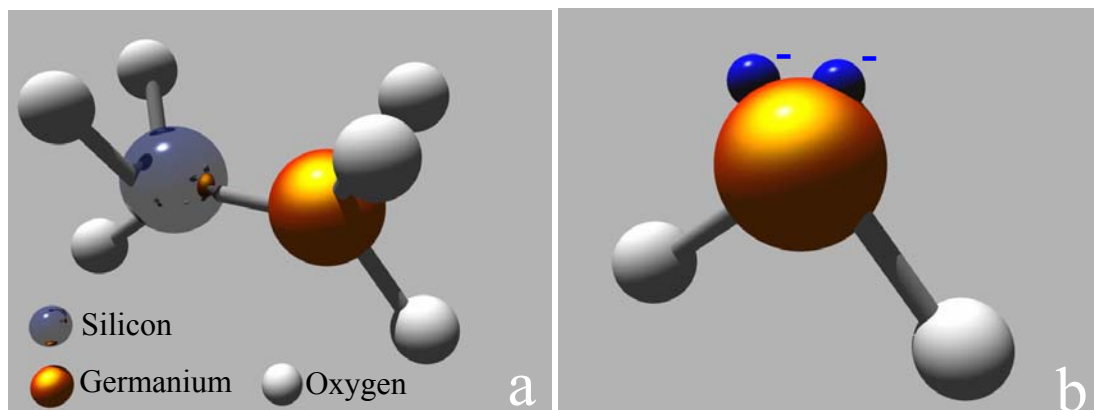


Figure 3.1 Germanium Oxygen Deficient centers: (a) neutral oxygen vacancy or Ge-Si wrong bond, (b) GeO in the reduced state

These oxygen deficiency centers were reported in the same work by Russell and Hand to create additional absorption bands in the material after irradiation with a few milliwatts per squared micrometer of a 488nm Ar^+ laser [5]. These new absorption bands are the result of Ge-Si bond breakage, charge release and retrapping at neighboring Ge sites, forming Ge(1) and Ge(2) color centers with absorption bands at 281 and 213nm, respectively [6]. Tsai, *et al*, identified the Ge(1) center as an electron trapped at a Ge atom coordinated to four O-Si next-nearest-neighbor atoms and the Ge(2) center as an electron trapped at a Ge atom coordinated to one O-Ge ($\equiv\text{Ge-O-Ge}\equiv$) and three O-Si next-nearest-neighbor atoms (Figure 3.2) [7,8].

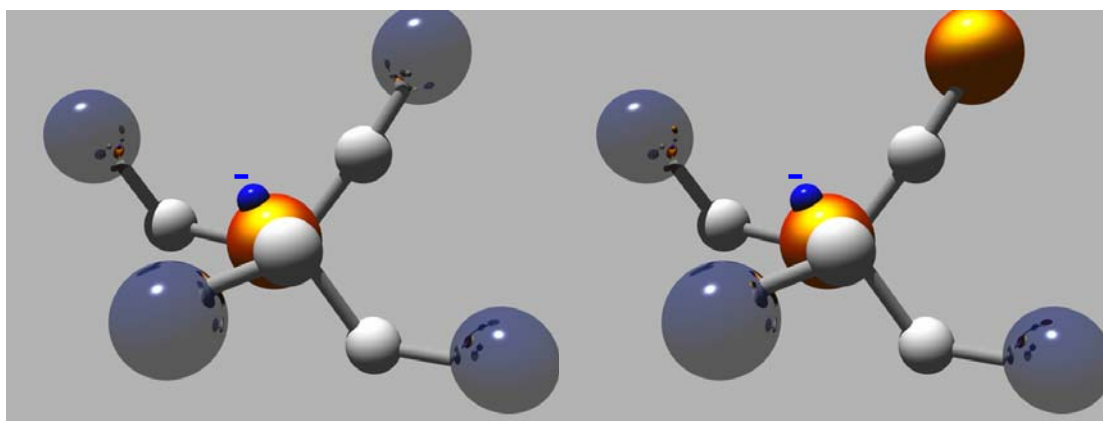


Figure 3.2 Ge(1) and Ge(2) centers

Yuen has studied UV absorption of germanosilicate glass and found three absorption bands located at 185nm, 242nm and 325nm [10]. According to Yuen the 242nm band is attributed to the presence of GeO in the glass and the 325nm band, which is 1000 weaker in magnitude than the 242nm band, is also related to GeO. Their difference in intensity lies in the fact that the 325nm band is correlated with a triplet to singlet transition, while the 242nm band with a singlet-singlet transition which is more probable to occur [10]. However, these two bands were later assigned to the wrong bond defect ($\equiv\text{Ge-Si}\equiv$ or $\equiv\text{Si-Si}\equiv$ bond) [6], [11]. GeO is a reactive species and is more likely to be incorporated as an oxygen vacancy in the germania silica network, producing the Ge-Si wrong bond. Finally, the 185nm absorption band was correlated with the formation of the GeE' centers.

Hosono, *et al*, [12] examined the photochemical reactions taking place inside a 10mol% GeO₂ – 90mol% SiO₂ glass preform upon Hg lamp and 248nm KrF laser irradiation. Their group confirmed the assignment of the 242nm absorption band to oxygen-deficient defects and the creation of Ge(1) and Ge(2) color centers after 248nm irradiation, abbreviated as GECs [13]. KrF irradiation was also found to photochemically convert part of the GECs to GeE' (Germanium electron centers). The formation of GeE' centers should take place through a single photon absorption process, since it can be generated using a Hg lamp of low power density [1]. The same group proposes that the formation of GECs and self trapped hole centers (STHs) is generated through a two photon absorption process [12]. A possible photochemical reaction leading to the creation of the GeE' center is presented in Figure 3.3. Shaver, *et al*, have also reported the creation of GeE' centers by means of two photon

absorption under 193nm laser irradiation [14]. However this assertion is still under investigation.

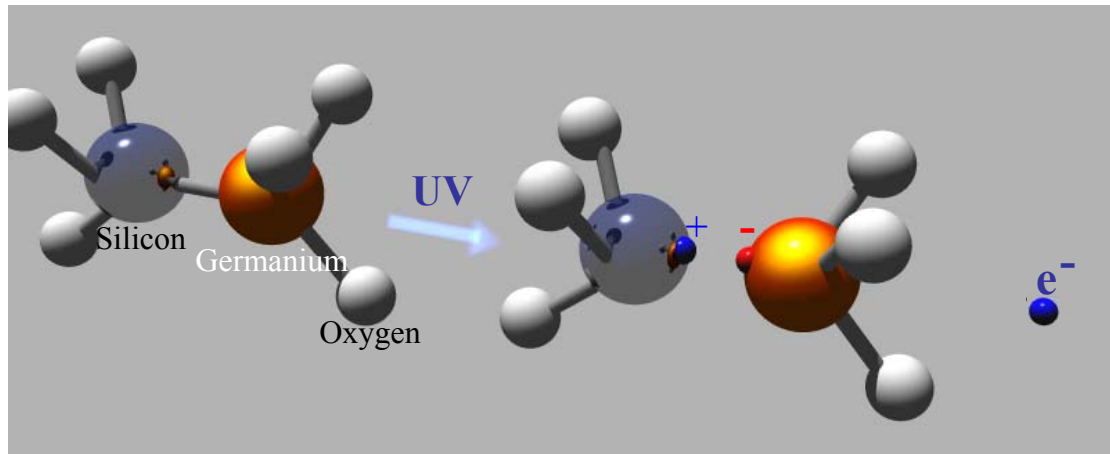


Figure 3.3 Creation of E' centers by means of UV irradiation

Dianov et al, conducted Raman spectroscopy at a fiber's germanosilicate core before and after 248nm laser irradiation [9]. The changes of the Raman spectra before and after irradiation suggested the decrease of order of the tetrahedron rings in the glass. Large rings (sixfold or more) were broken by the UV irradiation and formed fourfold, threefold or twofold rings [9]. This increase of low-fold rings is suggested by the same group to be the result of the destruction of the GeO₂ deficiency centers by UV irradiation and the conversion of the broken bonds into oxygen atoms with the formation of Ge-O-Ge and possibly Si-O-Ge(Si) bonds. Another effect of the 248nm UV irradiation on that type of glass was the creation of different forms of non-bridging oxygen hole centers or the creation of drawing induced centers [9], which are associated with an absorption band at 630nm [15].

Albert et al, have also studied the photosensitivity of germanosilicate optical fibers exposed to 193nm and 248nm laser radiation [18]. They used optical fibers with low and high germanium concentration and compared and studied the refractive index modulation during Bragg grating inscription with 193nm excimer laser radiation. It was reported that the index change rate of the hi-Ge fiber was varying linearly with the laser fluence, indicating a single photon absorption mechanism by the GODCs at that concentration. On the contrary, the low-Ge fiber demonstrated a refractive index change rate that varied proportionally to the square of the laser fluence, indicating the presence of a two photon/step absorption mechanism. Photosensitivity on low-Ge fibers has also been reported using 213nm 150ps radiation by Pissadakis, *et al*, [24],

where a significant component of the index change is attributed to glass compaction initiated by a two photon/step absorption process.

3.1.2 B-Ge co-doped optical fibers

The addition of various co-dopants in germanosilicate fibers can greatly enhance their photosensitivity. Williams, *et al*, reported that the addition of boron inside the fiber core can lead to a 4 times larger refractive index modulation after 248nm laser irradiation than that of pure germanosilicate fibers [16]. The boron codoping did not give rise to any other absorption peaks in the range between 200 – 300nm, nor did it affect the amplitude or shape of the main absorption band at 242nm [16]. This observation is indicating that the enhanced photosensitivity observed is not the product of additional production of GODCs due to boron doping. Instead, it is believed to be originating from photoinduced stress relaxation [17].

Shelby did an extensive study on the effect of ionizing radiation on borosilicate glasses [17]. He used a variety of compositions for his sample glasses and examined the glasses density, refractive index thermal expansion and permeation before and after irradiation. It was found that the magnitude of compaction was dependant on glass composition. The degree of compaction for a given irradiation dose increased roughly with the boron content of the glass [17]. This could be an indication that boron atoms are directly involved in the densification process. Also, Shelby claims that the photosensitivity of B-doped glass may be the result of competing processes which involve both positive and negative dilations related to the two phase nature of most borosilicate glasses [17]. Apart from densification of the glass matrix, Shelby reports stress relaxation after irradiation. It is assumed that the glass network is relieved from stresses before the radiation-braked boron oxygen bond reforms. Finally, in agreement with the density observations, the refractive index of these glasses also increased with increased irradiation dose.

Ky, *et al*, have conducted Bragg grating inscriptions on B-Ge co-doped optical fibers and measured changes in axial stresses and refractive index during irradiation with pulsed 240nm laser radiation [19]. It was initially found that the fiber core developed an axial stress that was increasing with increasing fluence. After a certain amount of fluence the core network is seen to exhibit dilation. This dilation is probably taking place after the depletion of oxygen deficiency centers and the formation of high tensile stresses inside the core network [19].

Dong, *et al*, have conducted Bragg grating inscriptions in B-Ge codoped optical fiber using 193nm laser radiation [25], where both positive and negative index changes were observed. The Bragg gratings formed by negative index changes were found to withstand higher temperatures than the ones formed by positive index changes. This could lead to the conclusion that negative index changes are related to structural changes inside the fiber core which exhibit greater demarcation temperatures than electronic changes.

3.1.3 SiO₂ (undoped) optical fibers

For the case of un-doped silicon glass, Weeks [20] was the first to identify a point defect using electron spin resonance (ESR). A narrow resonance was reported in the ESR spectra of neutron irradiated crystalline quartz and silica from a species termed the E' center. Using ESR, three intrinsic defects in silica have since been identified: the E' centre (SiE' center), the non-bonding oxygen hole centre (NBOHC, ≡O) and the peroxy (or superoxide) radical (≡O-O) [21]. They are schematically presented in Figure 3.4. Silica optical fibres also exhibit the characteristic absorption band at 630nm associated with the drawing induced defect (DID) [15]. The drawing induced defect (DID) originates from mechanical stresses that are stored in the glass matrix during the fiber drawing. In oxygen deficient silica, SiE' defects are very common, since the Si-Si wrong bonds – which give rise to SiE' defects – are the dominant precursor defect [3]. Thus the SiE' center is considered to be the fundamental defect in SiO₂ glasses. The absorption band that is associated to the SiE' center lays at 215nm [23]. Peroxy radicals give rise to an absorption band at 160nm, The NBOHCs at 260 and the Si-Si wrong bond at 245nm [3].

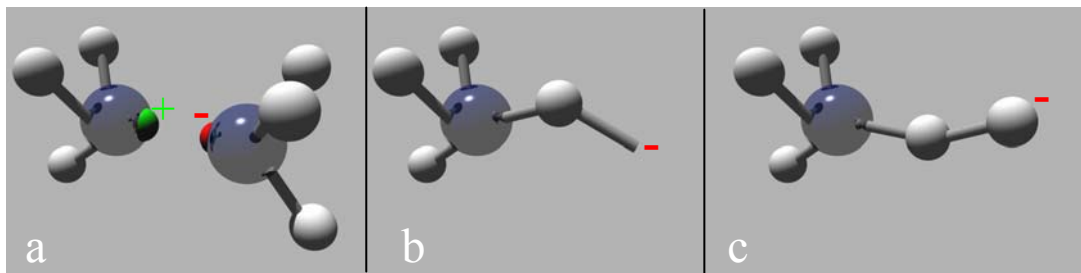


Figure 3.4 Silica defects: (a) SiE' center, (b) non binding oxygen hole center and (c) peroxy radical

Shaver, *et al*, have irradiated high purity ultraviolet grade fused silica with 193nm [14] and Escher have irradiated it with 248nm [22] excimer laser radiation. They have found that the lasers they used can create point defects similar to those

created by ionizing radiation [14]. After the completion of the 193nm irradiation of the samples Shaver, *et al*, measured the UV transmission spectrum of the irradiated area. They found two different permanent optical effects. The first is the appearance of two UV absorption bands located at 215nm and ~260nm, with the later being weaker than the 215nm band. The second effect is the creation of a birefringent annular zone observed using 632.8nm light. The birefringence is attributed to mechanical stresses, originating from irradiation induced volume changes [24]. By applying external compressive stress to the irradiated silica sample they managed to eliminate the radiation induced birefringence. This led to the conclusion that 193nm irradiation creates tensile stress in the unexposed areas caused by radiation-induced compaction of the exposed volume [14]. Consequently, the increase in density of the exposed area is accompanied by a change in the refractive index of the material. The mechanism creating these changes inside the glass network is initiated by a two photon absorption process, as evidenced by the quadratic dependence on laser fluence on the work by Shaver [14]. Fiori, *et al*, irradiated α -SiO₂ with 248nm laser and observed reversible and irreversible densification, attributed to rearrangement of strands of SiO₄ tetrahedra [26].

3.2 Photosensitivity mechanisms and models

A global model predicting the photoinduced index changes during Bragg grating inscription is a challenge that has not been accomplished. No single model can predict all of the experimental results, as there are many microscopic mechanisms taking place during the fiber irradiation. The effect of experimental parameters like the inscribing laser's wavelength, power, intensity, pulse duration and the variety of fiber types that can be used can initiate different physical mechanisms during grating inscription. Several attempts to model various photosensitivity mechanisms will be presented in the following subsections.

3.2.1 Color center model

Hand and Russell [5] proposed that color centers created after UV irradiation are responsible for the appearance of new absorption bands in the UV spectrum of germanosilicate glass. The resultant refractive index change was shown to follow the Kramers – Kronig relationship which can be expressed as [27]:

$$\Delta n_{eff}(\lambda) = \frac{1}{2\pi^2} P \int_0^{\infty} \frac{\Delta \alpha_{eff}(\lambda')}{1 - (\lambda/\lambda')^2} d\lambda' \quad (3.1)$$

where P is the principle part of the integral, λ is the wavelength, λ' is the wavelength for which the refractive index is calculated and $\Delta \alpha_{eff}$ is the effective change in the absorption coefficient of the defect given by:

$$\Delta \alpha_{eff}(\lambda) = (1/L) \int_0^L \Delta \alpha(\lambda, z) dz \quad (3.2)$$

where L is the glass thickness.

In this model, photoinduced changes in the properties of the glass introduce new electronic excitations and transitions of defects. These color center defects give rise to absorption bands at various wavelengths and are therefore responsible for the observed index changes.

Poyntz-Wright, *et al*, [28] have developed a quantitative color center model based on studies of absorption at 488nm. The mechanism proposed by them is no different than the one described in 3.1.1, or the one proposed by Hand and Russell [5] where Ge-Si wrong bonds (GODCs) are transformed into GeE' centers with the resulting electrons from the process trapped in Ge(1) and Ge(2) centers.

Hosono, *et al*, have found a strong correlation between the absorption band at 195nm and the GeE' centers, which shows compatibility with the Kramers Kronig mechanism [29]. There has been reported in the literature [30, 31] that the color center model can explain a large part of the measured magnitude of the index change for Type I gratings, which will be later described.

However, the color center model is not capable of explaining large refractive index changes. Changes of the order of 10^{-3} in standard telecommunications fibers [32] are difficult to be explained solely by the color center model, especially in a fiber with small Ge content in the core. It is also incapable of explaining the photosensitivity observed in undoped silicate glass optical fibers.

3.2.2 Stress relief model

Sceats, *et al*, [33] have proposed the stress relief model, assuming that the photoinduced refractive index changes inside the fiber core are the result of stresses alleviation. In a germanosilicate optical fiber the core is under tension because of the difference in thermal expansion between the core and cladding material as the fiber is rapidly cooled below the glass transition temperature during fiber drawing. Through

the stress optic effect the tension reduces the refractive index, thus, any photoinduced changes are expected to give rise to positive index changes in this model. Sceats, *et al*, claim that the breaking of the Ge-Si and Ge-Ge wrong bonds, lead to the relaxation of the tensioned fiber core and therefore give rise to positive index changes. However, stresses are not only present in germanosilicate fibers, but can also appear through point defects in undoped silica fibers. The advantage of the stress relief model is its ability to explain refractive index changes in these fibers, contrary to the color center model, which requires the presence of a dopant. The refractive index change induced by the core relaxation can be calculated for x-polarized light to be:

$$n_x = n_0 - c_1\sigma_x - c_2(\sigma_y + \sigma_z) \quad (3.3)$$

where n_0 is the unstressed material refractive index, c_1 and c_2 the stress optic coefficients and $\sigma_x, \sigma_y, \sigma_z$ are the stress coefficients along the respective axes. Experimental verification of the model comes from the work of Limberger, *et al*, [40] who measured axial stresses in the fiber during Bragg grating inscription. This model however cannot justify the thermal reversibility of grating inscription [34].

3.2.3 Compaction / Densification model

In the compaction / densification model, refractive index changes are the result of photoinduced density changes of the fiber core glass. This model was proposed for optical fibers by Bernardin and Lawandy [35], who conducted theoretical and experimental studies on germanosilicate fibers. Their idea was stimulated by experiments performed by Fiori and Devine, who observed that α -SiO₂ films irradiated with 248nm excimer laser light demonstrated both refractive index change and reversible reduction of their thickness [26]. The compaction model has been found to follow the Lorentz-Lorenz relation for refractivity (R) which is:

$$R = \frac{(n^2 - 1)}{\rho(n^2 + 2)} \quad (3.4)$$

where ρ is the specific gravity and n is the refractive index. Differentiation of (3.4) leads to [36]:

$$\Delta n = -\frac{(n^2 + 2)(n^2 - 1)}{6n} \left[1 - \frac{\Delta R}{(R \cdot \Delta V / V)} \right] \frac{\Delta V}{V} \quad (3.5).$$

Canning, *et al*, [92] irradiated germanosilicate waveguides with 193nm excimer laser radiation and observed both positive and negative refractive index changes. The positive index changes are proposed to originate from macroscopic polarizability

changes and the negative index changes are attributed to changes in the material density. This density change is speculated to be the result of breakage of high order ring structures to low order structures [26]. This speculation was further reinforced by Raman spectra of compressed amorphous silica [37]. Fiori and Devine applied hydrostatic pressure to silicate glasses and found refractive index changes similar to those produced by laser irradiation [37]. This result indicated that the compaction of amorphous silica is proceeding through internal structural rearrangements and not strictly through a process of defect creation.

Limberger, *et al*, have studied tension and compaction in telecommunications optical fibers after Bragg grating inscriptions [38]. They reported that the fiber's core tension was increased after the exposure, a result in contrast to the stress relief model and found glass compaction to take place along with the increase of the glass stress. Moreover, they conducted quantitative measurements on the effect of each mechanism and concluded that the photoelastic effect (due to stress) can reduce the amplitude of the modulated index change due to compaction by 31% – 35% [39]. A thorough study of silicate glass densification modeling has been conducted by Borelli and has been presented in numerous papers [40, 41]. Further work was conducted by Schenker and Oldham who studied the effects and correlation between densification and color centers [43]. Allan, *et al*, observed that the densification of fused silica under 193nm excimer laser radiation follows a power law in dose ($densification \propto NI^2$) [42]. It is interesting to note that glass compaction depends on both N (number of pulses) and I (fluence per pulse).

3.3 Phenomenological classification of Bragg gratings

So far, it has been discussed that photosensitivity in optical fibers can be manifested by many different kinds of microscopic mechanisms and photochemical reactions, which vary in amplitude and effect depending on the glass composition and inscription setup. Based upon observations on the dynamics of the refractive index modulation during Bragg grating recording and grating thermal stability, Bragg gratings have been classified into different categories. This classification serves as a globally accepted reference for the scientific community.

3.3.1 Type I Bragg gratings

Type I Bragg gratings are characterized by a monotonic change of both the average and modulated refractive index under laser irradiation [44]. These gratings usually exhibit excellent spectral characteristics but they are thermally demarked at temperatures as low as 300°C. The reflection spectrum of the guiding mode in these gratings is complementary to the transmission signal, indicating negligible loss due absorption or reflection in the cladding. Niay, *et al*, [45] report that the formation of Type I gratings in germanosilicate fibers is caused by the depletion of oxygen deficient centers and the formation of color centers which lead to positive refractive index changes. It has also been reported by Limberger, *et al*, that the development of Type I gratings is accompanied by an increase in the axial stress in the fiber core [19]. This type of gratings is very commonly utilized in telecommunications applications.

3.3.2 Type IIA Bragg gratings

Type IIA gratings are characterized by the complex behavior of the average and modulated refractive index trend during laser irradiation [46]. Their formation requires the existence of a saturated Type I grating, which under prolonged irradiation is partially or totally erased and then the Type IIA grating is starting to form, reaching saturation. Simultaneously the average refractive index shifts from positive changes to negative sign changes (blue-shifting) during the inscription of the Type IIA component. This mechanism is indicative of an inverse relationship between the index modulation of the Type I and Type IIA grating. Niay, *et al*, have observed that the mechanism involved in the Type IIA grating formation induces negative index changes to the core of a germanosilicate fiber [45]. Dong, *et al*, have also reported the inscription of negative index gratings after the formation and bleaching of positive index gratings in B-Ge codoped optical fiber [25]. Ky, *et al*, have studied Type IIA grating growth in B/Ge and Sn/Ge codoped optical fibers and reported that the Type IIA gratings are slowly formed alongside negative index changes and reduction in the core's stresses [19]. According to their group this is an indication that the origin of the negative refractive index changes is photoinduced compaction in the bright fringes of the irradiated core and dilation in the dark ones. The thermal stability of these gratings has been studied by the entire above mentioned groups, as well as, by Tsai et al [61], who tried to correlated thermal stability with specific defect sites. Type IIA gratings have been found to endure temperatures of up to 500°C for more than 4 hours without

degradation. Groothoff and Canning have also reported the formation of thermally durable Type IIA gratings in a custom made B/Ge optical fiber under 193nm ArF laser irradiation [62]. These gratings were reported to withstand temperatures of up to 700°C without strength loss. From the thermal annealing studies it is evident that an advantage of Type IIA gratings over Type I is the enhanced thermal stability, a feature attractive for high temperature sensing applications. Finally, Type IIA grating formation has also been observed by using 213nm laser radiation [24].

3.3.3 Type II Bragg gratings

Type II gratings were first demonstrated by Russell, *et al*, [47]. The grating was produced by a single high energy ($1\text{J}/\text{cm}^2$) pulse of an excimer laser in an experiment to correlate pulse energy and grating strength. There is a critical level of absorbed energy, which – if surpassed – triggers a highly non linear mechanism that initiates damage to the fiber hyperstructure. The damage is confirmed by the examination of a Type II grating under an optical microscope, where a damage track at the core-cladding interface is easily observed. Another interesting remark concerning the damage track is the fact that it is localized on the illuminated side of the core, indicating a strong asymmetrical local absorption of UV laser light. Due to this asymmetrical damage inside the core, both the reflection and transmission spectrum of this type of gratings exhibit non-uniformities and are broader compared to Type I and Type IIA grating spectra. Their advantage, though, is their high temperature stability. In thermal annealing tests conducted by Russell, *et al*, [47] it was demonstrated that this grating type can withstand temperatures up to 800°C for 24h with no degradation in grating strength. This makes them attractive for high temperature sensing applications.

3.3.4 Other Types of Bragg gratings

Alongside the three major Bragg grating types described above, three more types have been reported in the literature. Mihailov, *et al*, [48] have proposed two new grating types named Type I-IR and Type II-IR. These gratings are produced by an ultrafast (125fs) infrared (80nm) Ti:Sapphire laser, with the first (Type I-IR) being formed with laser pulse energy below the damage threshold of the fiber material and the second one (Type II-IR) occurs coincidentally with white light generation inside the fiber. Both grating types withstand high temperatures [48] with the Type II-IR retaining their strength for more than 450 hours at 1000°C. Another grating type has

been proposed by Bennion, *et al*, [49]. It is the Type IA Bragg grating, which is formed under prolonged UV exposure of a standard grating in hydrogenated germanosilicate fiber.

3.4 Femtosecond induced interactions

The use of ultrafast laser systems on in-fiber Bragg grating inscription was first realized by Mihailov, *et al*, [50] by using an 800nm 120fs Ti:Sapphire laser system and a specially designed phase mask. Hirao, *et al*, had previously used ultrafast laser systems for the fabrication of long period gratings [51]. Mihailov, *et al*, managed to induce index changes of up to 1.9×10^{-3} inside the core of an SMF-28 fiber (containing 3.5% GeO₂). The spectral quality of the grating was similar to that of UV-inscribed Type I, but its thermal stability was similar to this of Type II gratings [50]. This unique grating annealing and inscription behavior implied that the dominant index change mechanism was not originating from the exploitation of GODCs to induce electronic changes. Most probably, non linear mechanisms (such as multi photon absorption) take place as well.

Since then, Bragg gratings inscribed with both ultraviolet and infrared femtosecond (fs) laser systems have been studied both for their unique properties and to gain a better insight on the mechanisms behind index changes. In this section basic ultrafast laser-matter interactions will be discussed along with their effect on Bragg grating inscription.

3.4.1 Non linear ionization

Mihailov, *et al*, [50] examined 800nm fs-inscribed Bragg gratings under an optical microscope and discovered damage tracks throughout the whole fiber core region and in the core-cladding interface. This damage could be the result of a high energy pulse, but for the case of the 300μJ/pulse inscriptions [50] it seems highly unlikely. However, it is possible to occur multi photon absorption in the core material causing there structural changes. Later, Mihailov, *et al*, [52] conducted Bragg gratings inscriptions on both Ge-doped and all-SiO₂ fibers, where it was observed that periodic structures could be easily photoimprinted on both types of fibers. This finding verifies that 800nm femtosecond laser radiation initiates a different refractive index change

mechanism than longer pulse duration UV lasers. This mechanism is speculated to be nonlinear multiphoton ionization resulting in local melting and rapid resolidification of the fiber material [53].

Multi photon ionization is a process that can be induced by two types of mechanisms: Photoionization and avalanche ionization [54]. Photoionization refers to direct excitation of the electron by the laser field. Depending on the laser wavelength and intensity as well as the properties of the material exposed, photoionization can take place through tunneling or multiphoton ionization [54]. In tunneling photoionization the laser field suppresses the Coulomb well enough that a bound electron can tunnel through the short barrier and become free (Figure 3.5a). In multiphoton ionization, the excitation of an electron from the valence to the conduction band takes place through successive absorptions of more than one photon (Figure 3.5c). The transition point between multiphoton ionization and tunneling ionization was estimated by Keldysh [55]. The Keldysh parameter, γ , is defined as

$$\gamma = \frac{\omega}{e} \left[\frac{m c n \epsilon_0 E_g}{I} \right]^{\frac{1}{2}} \quad (3.6)$$

where ω is the laser frequency, I is the laser intensity at the focus, m and e are the reduced mass and charge of the electron, c is the velocity of light, n is the refractive index of the material, E_g is the band gap of the material, and ϵ_0 is the permittivity of free space. When the Keldysh parameter is larger than about 1.5 photoionization is a multiphoton process. Similarly, for values smaller than 1.5, photoionization is a tunneling process. For values near 1.5, an intermediate model may be accounted (Figure 3.5b).

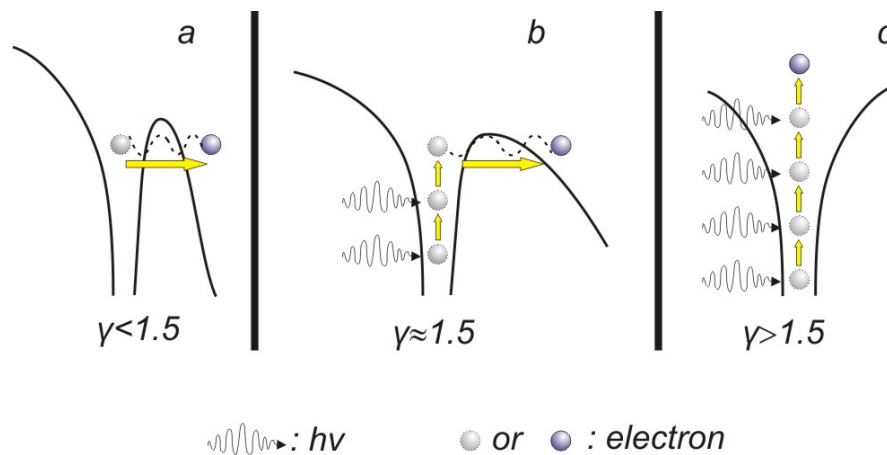


Figure 3.5 (a) tunneling ionization, (b) intermediate ionization, (c) multiphoton ionization

On the other hand, avalanche ionization involves free-carrier absorption followed by impact ionization [54]. An electron already in the conduction band of the material linearly absorbs several laser photons sequentially, moving to higher energy states in the conduction band (Figure 3.6a). After the sequential absorption of n photons, where n is the smallest number that satisfies the relation $k\hbar\omega \geq E_g$ [54], the electron's energy exceeds the conduction band minimum by more than the band gap energy. The electron can then collisionally ionize another electron from the valence band (Figure 3.6b).

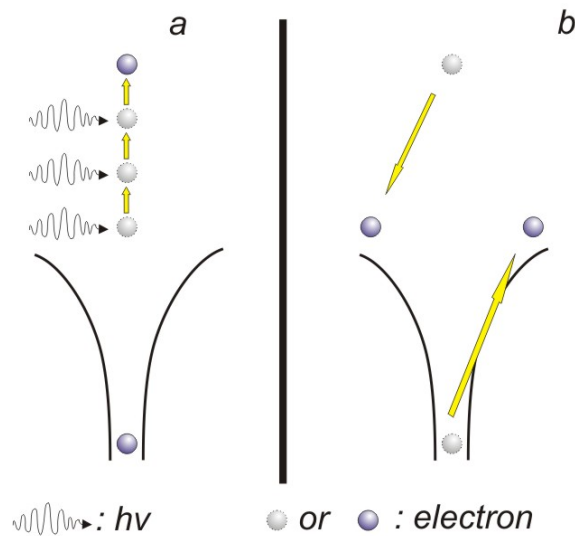


Figure 3.6 (a) Absorption from a “seed” electron at the conduction band, (b) Impact ionization

The seed electrons required by avalanche ionization to be in the conduction band of the material are provided either by thermally excited carriers, by easily ionized impurity or defect states, or by carriers that are directly photoexcited by multiphoton or tunneling ionization.

3.4.2 Heat accumulation - dissipation

For pulse durations longer than a few tens of picoseconds, there is a significant transfer of energy from the laser excited electrons to the lattice on the time scale of the pulse duration. The energy transferred to the lattice is carried out of the focal volume by thermal diffusion. Damage can occur in the material, when its temperature in the irradiated region becomes high enough for the material to melt or fracture [56]. Energy is deposited into the material by the laser pulse and is transported out of the irradiated region by thermal diffusion, thus it is the relative rate of energy deposition and thermal diffusion that determines the damage threshold.

For pulses shorter than a few picoseconds, the mechanism of thermal transfer is totally different than for longer laser pulses. The non-linear absorption occurs on a time scale that is short compared to the time scale for energy transfer to the lattice, decoupling the absorption and lattice heating processes [57]. Electrons in the conduction band are heated by the laser pulse much faster than they can cool by phonon emission, diffuse out of the irradiated volume, or recombine with their parent ion. This ultra fast deposition of energy into the material, on a time scale much faster than the thermal diffusion time, could lead to structural changes of the bulk material.

The above picture can be inverted, though, should the use of femtosecond laser pulses be accompanied by very high repetition rates. Since the effects discussed above, are studied on the time scale, the effect of the laser pulse repetition rate on heat accumulation and dissipation should not be omitted. In the case of femtosecond pulse duration one can offset the high heat dissipation rate by applying very large repetition rates. It has been calculated by Herman, *et al*, [58] that heat starts being accumulated at the bulk material when repetition rates higher than 100 kHz are utilized.

3.5 Conclusions

In this chapter a brief discussion on the origin of photosensitivity and its modeling in optical fibers was presented. Photosensitivity for both doped and undoped fibers was studied along with models which are used for experimental correlation of observed data with underlying physical mechanisms during laser irradiation. As stated in the presentation of the models above, there is no global model that can accurately predict photoinduced refractive index changes inside an optical fiber. A more realistic approach on the modeling of photoinduced changes in a dielectric material can be attained by taking into account multiple photosensitivity models and mechanisms each with varying contribution to the total changes. The modeling of photosensitivity is further complicated by the use of femtosecond laser pulses, who promote non-linear interactions between light and matter.

References

- [1] H. Hosono, *et al*, “Nature and origin of the 5-eV band in SiO₂:GeO₂ glasses”, *Physical Review B*: **46**: 11445-11451, (1992)
- [2] J. Nishii, *et al*, “Photochemical reactions in GeO₂-SiO₂ glasses induced by ultraviolet radiation: Comparison between Hg lamp and excimer laser”, *Physical Review B*, **52**: 1661-1665, (1995)
- [3] A. Othonos and K. Kali, “Fiber Bragg gratings”, Artech House Inc., London, (1999)
- [4] J. Albert, B. Malo, F. Bilodeau, D.C. Johnson, K.O. Hill, Y. Hibino and M. Kawachi, “Photosensitivity in Ge-doped silica optical waveguides and fibers with 193-nm light from an ArF excimer laser”, *Optics Letters*, **19**: 387-389, (1994)
- [5] D.P. Hand, P. St. Russell, “Photoinduced refractive-index changes in germanosilicate glass”, *Optics Letters* **15**: 102-104, (1990)
- [6] E.J. Friebele and D.L. Griscom, *Proceedings of the Materials Research Society*, Pittsburgh, p.319, (1986)
- [7] T.E. Tsai, D.L. Griscom, E.J. Friebele, “On the structure and of Ge-associated defect centers in irradiated high purity GeO₂ and Ge-doped SiO₂ glasses”, *Diffusion and Defect Data*, **53-54**: 469-476, (1987)
- [8] T.E. Tsai, D.L. Griscom, “Defect centres and photoinduced self-organization in Ge-doped silica core fiber”, *International Workshop on Photoinduced Self-Organization Effects in Optical Fibre, Proceedings SPIE* **1516**: 14-28, (1991)
- [9] E.M. Dianov, V.G. Plotnichenko, V.V. Koltashev, Yu. N. Pyrkov, N.H. Ky, H.G. Limberger, R.P. Salathe, “UV-irradiation-induced structural transformation of germanosilicate glass fiber”, *Optics Letters*, **22**: 1754-1756, (1997)
- [10] M. J. Yuen, “Ultraviolet absorption studies of germanium silicate glasses”, *Applied Optics*, **21**: 136, (1982)
- [11] St. J. Russell, D.P. Hand, L.J. Poyntz-Wright, “Frequency doubling, absorption and grating formation in glass fibres: Effective defects or defective effects?”, *Fiber Laser Sources and Amplifiers II, Proceedings SPIE*, **1373**: 126-139, (1990)

- [12] J. Nishii, N. Kitamura, H. Yamanaka, H. Hosono, H. Kawazoe, “Ultraviolet-radiation-induced chemical reactions through one- and two-photon absorption processes in GeO₂-SiO₂ glasses”, *Optics Letters*, **20**: 1184–1186, (1995).
- [13] H. Kawazoe, *Journal of Non-Crystalline Solids*, **71**: 231 (1985)
- [14] M. Rothschild, D.J. Ehrlich and D.C. Shaver, “Effects of excimer laser irradiation on the transmission, index of refraction, and density of ultraviolet grade fused silica”, *Applied Physics Letters* **55**: 1276-1278, (1989)
- [15] P. Kaiser, “Drawing induced coloration in vitreous silica fibers”, *Journal of the Optical Society of America*, **64**: 475-481, (1974)
- [16] D. L. Williams, B. J. Ainslie, J. R. Armitage, R. Kashyap, R. Campbell, “Enhanced UV photosensitivity in boron codoped germanosilicate fibres”, *Electronic Letters*, **29**: 45-47, (1993)
- [17] J. E. Shelby, “Effect of radiation on the physical properties of borosilicate glasses”, *Journal of Applied Physics* **51**: 2561-2565, (1980)
- [18] J. Albert, B. Malo, K.O. Hill, F. Bilodeau, D.C. Johnson, S. Theriault, “Comparison of one photon and two photon effects in the photosensitivity of germanium doped silica optical fibers exposed to intense ArF excimer laser pulses”, *Applied Physics Letters* **67**: 3529-3531, (1995)
- [19] N. H. Ky, H.G. Limberger, R.P. Salathe, F. Cochet, I. Dong, “UV-irradiation induced stress and index changes during the growth of Type I and Type IIA fiber gratings”, *Optics Communications* **225**: 313-318, (2003)
- [20] R.A. Weeks, “Paramagnetic resonance of lattice defects in irradiated quartz”, *Journal of Applied Physics* **27**: 1376-1381, (1956)
- [21] D. L. Griscom, “Defect structure of glasses: Some outstanding questions in regard to vitreous silica”, *Journal of Non Crystalline Solids* **73**: 51-77, (1985)
- [22] G. C. Escher, *Proceedings of SPIE* **998**: 30, (1988)
- [23] D. L. Griscom, *Proceedings of SPIE* **541**: 38, (1985)
- [24] S. Pissadakis, M. Konstantaki, “Photosensitivity of germanosilicate fibers using 213nm, picosecond Nd:YAG radiation”, *Optics Express* **13**: 2605-2610, (2005)
- [25] L. Dong, W.F. Liu, L. Reekie, “Negative-index gratings formed by a 193nm excimer laser”, *Optics Letters* **21**: 2032-2034, (1996)
- [26] C. Fiori, A. Devine, “Evidence for a wide continuum of polymorphs in α -SiO₂”, *Physical Review B* **33**: 2972-2974, (1986)

[27] St. J. Russell, *et al*, “Optically induced creation, transformation and organization of defects and color centers in optical fibers”, *International Workshop on Photoinduced Self-Organization Effects in Optical Fiber*, Quebec City, Quebec, *Proceedings SPIE* **1516**: 47-54, (1991)

[28] L. J. Poyntz-Wright, M. E. Fermann, P. St. Russell, “Non linear transmission and color center dynamics in germanosilicate fibers at 420 – 540nm”, *Optics Letters* **13**: 1023-1025, (1988)

[29] Hosono, *et al*, “Correlation between GeE’ centers and optical absorption bands in SiO₂:GeO₂ glasses”, *Japanese Journal of Applied Physics* **35**: L234-L236, (1996)

[30] R. M. Atknis, V. Mizrahi, T. Erdogan, “248nm induced vacuum UV spectral changes in optical fiber preform cores: Support for a colour center model of photosensitivity”, *Electronics Letters* **29**: 385-387, (1993)

[31] L. Dong, *et al*, “Photoinduced absorption changes in germanosilicate preforms: Evidence for the color-centre model of photosensitivity”, *Applied Optics* **34**: 3436-3440, (1995)

[32] H. G. Limberger, P. Y. Fonjallaz, R. P. Salathe, “Spectral characterization of photoinduced highly efficient Bragg gratings in standard telecommunications fibres”, *Electronics Letters* **18**: 953-955, (1993)

[33] M. G. Sceats, G. R. Atknis, S. B. Poole, “Photoinduced index changes in optical fibers”, *Annual Reviews in Material Science*, **23**: 381-410, (1993)

[34] R. M. Atkins, V. Mizrahi, “Observations of changes in UV absorption bands of single mode germanosilicate core optical fibers on writing and thermally erasing refractive index gratings”, *Electronics Letters*, **28**: 1743-1744, (1992)

[35] J. P. Bernardin, N. M. Lawandy, “Dynamics of the formation of Bragg gratings in germanosilicate optical fibers”, *Optics Communications*, **79**: 194-199, (1990)

[36] M.V. Bazylenko, D. Moss, J. Canning, “Complex photosensitivity observed in germanosilica planar waveguides”, *Optics Letters* **23**: 697-699, (1998)

[37] C. Fiori, R. A. B. Devine, “Ultraviolet irradiation induced compaction and photoetching in amorphous thermal SiO₂”, *Materials Research Society Symposium Proceedings*, **61**: 187-195, (1986)

- [38] P.Y. Fonjallaz, H.G. Limberger, R.P. Salathe, F. Cochet, B. Leuenberger, “Tension increase correlated to refractive index change in fibers containing UV-written Bragg gratings”, *Optics Letters* **20**: 1346-1348, (1995)
- [39] H.G. Limberger, P.Y. Fonjallaz, R.P. Salathe, F. Cochet, “Compaction and photoelastic induced index changes in fiber Bragg gratings”, *Applied Physics Letters* **68**: 3069-3071, (1996)
- [40] N. F. Borrelli, D. C. Allan, R. A. Modavis, “Direct measurement of 248- and 193-nm excimer-induced densification in silica–germania waveguide blanks”, *Journal of the Optical Society of America A*, **16**: 1672-1679, (1999)
- [41] N. F. Borrelli, C. Smith, D. C. Allan, T. P. Seward III, “Densification of fused silica under 193-nm excitation”, *Journal of the Optical Society of America A*, **14**: 1606-1615, (1997)
- [42] D. C. Allan, C. Smith, N. F. Borrelli, T. P. Seward III, “193-nm excimer-laser-induced densification of fused silica”, *Optics Letters*, **21**: 1960-1962, (1996)
- [43] Richard E. Schenker, William G. Oldham, “Ultraviolet-induced densification in fused silica”, *Journal of Applied Physics*, **82**: 1065-1071, (1997)
- [44] M. Douay, W. X. Xie, E. Fertein, P. Bernage, P. Niay, J. F. Bayon, and T. Georges, *Proceedings of SPIE* **2044**: 88, (1993)
- [45] P. Niay, P. Bernage, S. Legoubin, M. Douay, W. X. Xie, J. F. Bayon, T. Georges, M. Monerie and B. Poumellec, “Behaviour of spectral transmissions of Bragg gratings written in germania-doped fibres: Writing and erasing experiments using pulsed or CW UV exposure”, *Optics Communications* **113**: 176-192, (1994)
- [46] W. X. Xie, P. Niay, P. Bernage, M. Douay, J. F. Bayon, T. Georges, M. Monerie, “Experimental evidence of two types of photorefractive effects occurring during photoinscriptions of Bragg gratings within germanosilicate fibres”, *Optics Communications* **104**: 185-195, (1993)
- [47] J. L. Archambault, L. Reekie, P. St. J. Russell, “100% Reflectivity Bragg reflectors produced in optical fibers by single excimer laser pulses”, *Electronics Letters*, **29**: 453-455, (1993)
- [48] C. Smelser, S. Mihailov, D. Grobnic, “Formation of Type I-IR and Type II-IR gratings with an ultrafast IR laser and a phase mask”, *Optics Express*, **13**: 5377-5386, (2005)

- [49] Y. Liu, J. A. R. Williams, L. Zhang, I. Bennion, “Abnormal spectral evolution of fibre Bragg gratings in hydrogenated fibers”, *Optics Letters*, **27**: 586–588, (2002)
- [50] S. J. Mihailov, C. W. Smelser, P. Lu, R. B. Walker, D. Grobnic, H. Ding, G. Henderson, “Fiber Bragg gratings made with a phase mask and 800-nm femtosecond radiation”, *Optics Letters*, **28**: 995-997, (2003)
- [51] Y. Kondo, K. Nouchi, T. Mitsuyu, M. Watanabe, P. G. Kazansky, K. Hirao, “Fabrication of long-period fiber gratings by focused irradiation of infrared femtosecond laser pulses”, *Optics Letters*, **24**: 646–648, (1999)
- [52] S. J. Mihailov, C. W. Smelser, D. Grobnic, R. B. Walker, P. Lu, H. Ding, J. Unruh, “Bragg gratings written in all- SiO₂ and Ge-doped core fibers with 800-nm femtosecond radiation and a phase mask”, *Journal of Lightwave Technology*, **22**: 94–100, (2004)
- [53] K. M. Davis, K. Miura, N. Sugimoto, K. Jirao, “Writing waveguides in glass with a femtosecond laser”, *Optics Letters*, **21**: 1729-1731, (1996)
- [54] C. B. Schaffer, “Interaction of Femtosecond Laser Pulses with Transparent Materials”, *Ph.D. Thesis, Harvard University, Massachusetts*, (2001)
- [55] L. V. Keldysh, *Soviet Physics JETP* **20**: 1307, (1965)
- [56] B. C. Stuart, Michael D. Feit, S. Herman, A. M. Rubenchik, B. W. Shore, M. D. Perry, “Optical ablation by high-power short-pulse lasers”, *Journal of Optical Society of America B*, **13**: 459-468, (1996)
- [57] B. C. Stuart, M. D. Feit, S. Herman, A. M. Rubenchik, B. W. Shore, M. D. Perry, “Nanosecond-to-femtosecond laser-induced breakdown in dielectrics”, *Physical Review B*, **53**: 1749-1761, (1996)
- [58] S. M. Eaton, H. Zhang, P. R. Herman, F. Yoshino, L. Shah, J. Bovatsek, A. Y. Arai, “Heat accumulation effects in femtosecond laser written waveguides with variable repetition rate”, *Optics Express*, **13**: 4708-4716, (2005)
- [61] T. E. Tsai, E. J. Friebele, D. L. Griscom, “Thermal stability of photoinduced gratings and paramagnetic centres in Ge- and Ge/P-doped silica optical fibres”, *Optics Letters*, **18**: 935-937, (1993)
- [62] N. Grothoff, J. Canning, “Enhanced type IIA gratings for high-temperature operation”, *Optics Letters*, **29**: 2360-2362, (2004)

4. Type IIA Bragg Grating Incriptions in B-Ge fibers using 248nm fs and ps laser radiation

In the first experimental part of this thesis, Bragg grating recordings which were realized in B-Ge codoped optical fiber will be presented. For the recording process several 248nm laser systems were used, varying in pulse duration from a few tens of nanoseconds to a few hundreds of femtoseconds. This wide range of pulse durations available, gave the possibility to study the effect of pulse intensity in the Bragg grating inscription. Such a study can provide insight behind the physical mechanisms underlying the refractive index changes and the effect of non linear mechanisms in the inscription process.

Apart from the 248nm, a 193nm excimer laser was also used for the fabrication of in-fiber Bragg gratings. The above wavelengths were chosen because they overlap with known absorption bands of germanosilicate glasses. 248nm is close to the 242nm absorption band of germanosilicate glasses caused by germanium oxygen deficiency centers (GODCs) [1] and 193nm lies near the 185nm absorption band of the GeE' centers [2]. The utilization of femtosecond laser pulses gave rise to both positive and negative index changes inside the fiber core, even for moderate fluency per pulse, and thus both Type I and Type IIA gratings were observed. Under high intensity exposures, Bragg gratings exhibited enhanced thermal stability, indicating the existence of a physical mechanism that has not been clearly identified [3]. For the case of 248nm nanosecond laser irradiation the use of high fluencies per pulse was required to form Type IIA gratings. On the contrary, 193nm nanosecond irradiation required less fluence per pulse than 248nm nanosecond irradiation to form Type IIA gratings, due to the higher photon energy (6.4eV for 193nm versus 5eV for 248nm) and the magnitude of the absorption bands that each wavelength overlaps with. However, high intensity femtosecond inscriptions proved to be the fastest and most efficient ones, producing gratings with fine spectral features and higher thermal stability compared to the other Type IIA gratings. The magnitude and rate of refractive index changes during the irradiation of the gratings will be discussed along with their thermal durability.

4.1 Bragg grating inscription apparatus and methodology

4.1.1 Laser systems

Three different laser systems were used for the fabrication of Bragg gratings inside the B-Ge codoped optical fibers. A brief overview of the laser specifications is presented in table 4.1. The first system is a KrF excimer laser manufactured by Lambda Physik, emitting 248nm 500fs laser pulses. This system also provides the possibility to alter the pulse duration from 500fs to 5ps or 120fs. The shift from 500fs to 5ps can be realized by placing an etalon [7] at the stage of the final amplification of the pulse which temporally broadens the pulse (and spectrally decreases it). Shifting from 500fs to 120fs requires the use of two reflection gratings which are placed in parallel in the path of the propagating beam after it has exited the laser. The gratings broaden the spectral content of the pulse reducing its duration. With this system, it was possible to achieve intensities of up to $250\text{GW}/\text{cm}^2$ per pulse by focusing the laser beam to the fiber. The repetition rate during Bragg grating fabrication did not exceed 10Hz. The spatial coherence length of this laser is around $100\mu\text{m}$ for emission at 500fs and the temporal coherence is estimated to be $75\mu\text{m}$.

In order to further expand the pulse durations available at 248nm a second laser system was used. This system is a typical KrF excimer laser with pulse duration of 38ns. The maximum intensity achieved in this system by focusing the laser light into the fiber was $\sim 12\text{MW}/\text{cm}^2$ per pulse at a repetition rate of 10Hz.

Finally, laser emission at 193nm took place through an ArF excimer laser. This system, manufactured by TUI Laser, is capable of delivering 193nm 10ns laser pulses with spatial coherence above $500\mu\text{m}$. The intensity per pulse of this laser, after focusing into the fiber was $23\text{MW}/\text{cm}^2$.

Table 4-1 Laser systems used for the fabrication of in-fibre Bragg gratings

Wavelength	Pulse duration	Energy per pulse	Maximum Intensity delivered	Repetition Rate	Spatial Coherence Length
248nm	120fs	12mJ	$250\text{GW}/\text{cm}^2$	10Hz	$100\mu\text{m}$
248nm	500fs	20mJ	$100\text{GW}/\text{cm}^2$	10Hz	$100\mu\text{m}$
248nm	5ps	36mJ	$20\text{GW}/\text{cm}^2$	10Hz	$100\mu\text{m}$
248nm	38ns	600mJ	$11.84\text{MW}/\text{cm}^2$	10Hz	$100\mu\text{m}$
193nm	10ns	8mJ	$23\text{MW}/\text{cm}^2$	40Hz	$500\mu\text{m}$

4.1.2 The phase mask technique

In order to make possible the inscription of Bragg gratings in an optical fiber, it is necessary to produce a permanent periodic index change inside the fiber core. There have been many methods reported in the literature for the realization of this purpose, like the point by point inscription method [4], interferometric fabrication [5] and the phase mask technique [6]. The phase mask technique is the one used throughout the experimental part of this thesis. The phase mask is a transparent diffractive optical element with a relief grating structure etched on it. The grating of the phase mask is designed to be a phase grating, namely a structure that is imposing periodic phase changes on the light that is transmitted through the grating. For the case of Bragg grating inscription these phase changes periodically create dark (light out of phase) and bright (light in phase) fringes (see Figure 4.1) in the Fresnel diffractive regimes [46]. These bright fringes in turn induce refractive index changes in the fiber core, while the dark fringes leave their region of incidence unaltered, forming a periodic refractive index modulation inside the fiber core. The phase mask technique offers the unique advantage of creating the interference pattern through the optical element itself, eliminating time consuming and difficult laser beam collimation. For this reason, this technique is very popular, especially when low spatial and temporal coherence systems will be used.

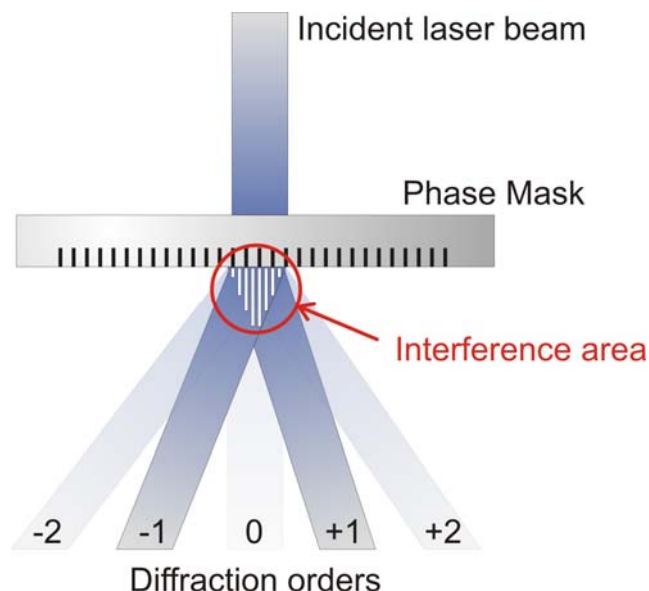


Figure 4.1 The phase mask and the creation of the interference pattern

The periodicity of the interference pattern induced in the fiber core is determined by the relief grating period Λ . Using vector analysis it is found that for eliminated zero order transmitted through the phase mask, a $\Lambda/2$ interference pattern

is formed in the Fresnel vicinity of the element, generated by the mixing of the +1 and -1 diffraction orders. In Figure 4.2, a basic layout of the etched grating parameters is illustrated.

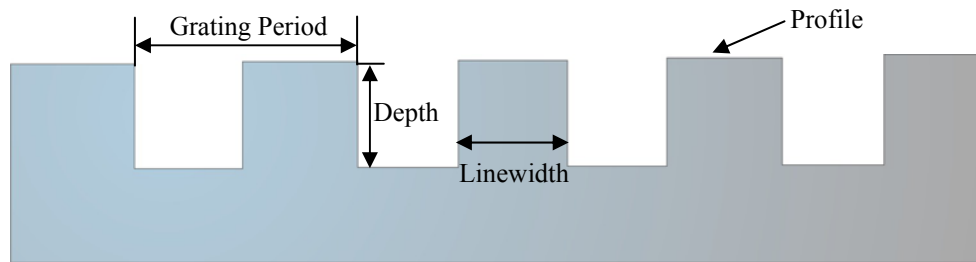


Figure 4.2 Etched grating parameters

The grating period, Λ , is defined as the distance between the equally spaced grating grooves and it is the determinant parameter for the beam splitting order and angle of incident light of λ wavelength [8] as determined by the grating equation:

$$m \cdot \lambda = \Lambda \cdot (\sin\theta_I + \sin\theta_D),$$

where m is the m^{th} diffraction order, λ is the illumination wavelength, Λ the grating period, θ_I the angle of incident illumination and θ_D the angle of diffraction for the m^{th} diffraction order. The determination of Λ is important, since the periodicity of the interference pattern created is $\Lambda/2$.

The depth of the grating is the distance from the top to the bottom of the grating grooves and determines the minimization of the 0^{th} order and the diffraction strength of the higher orders [8, 46].

The phase mask material can vary depending upon illumination wavelength and application. However, for Bragg grating inscription with ultraviolet laser systems it is rather common to fabricate phase masks using UV grade fused silica with an antireflection dielectric coating in the back side for achieving improved transmission.

4.1.3 Bragg grating inscription setup

The laser systems described above along with the phase mask and a set of beam manipulation components comprise the grating inscription setup. An illustration of this setup is presented in Figure 4.3.

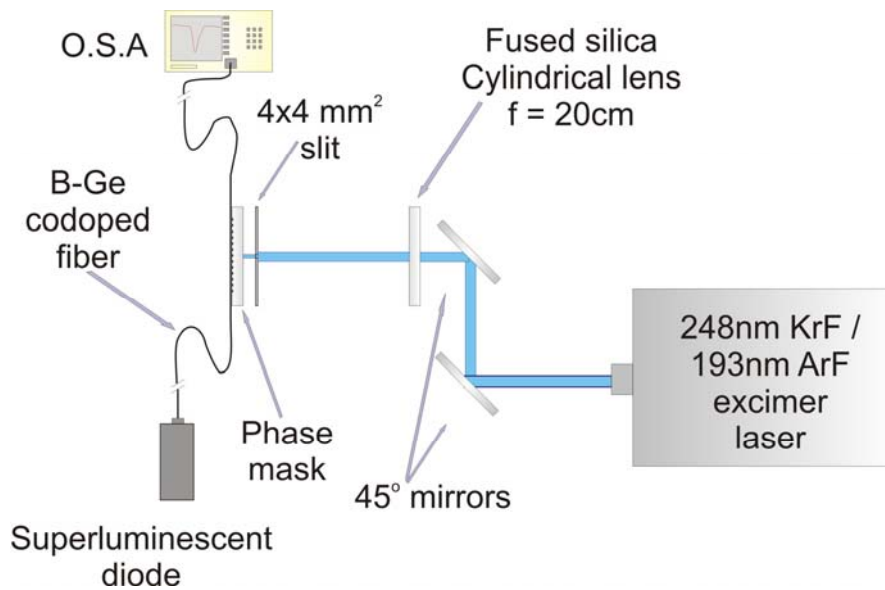


Figure 4.3 Bragg grating inscription setup for B-Ge codoped optical fibers.

After the laser beam exit aperture a 10m focal length spherical lens is reducing the size of the beam. A set of mirrors direct the beam to a cylindrical lens, which is used to focus the beam on the optical fiber. The optical fiber is placed on a micrometric x-y-z translational stage which is used for fine tuning position relatively to the phase mask. The typical distance kept between the fiber and the phase mask is of the order of 50 μ m, as measured by the translational stage verniers. The fiber is rigidly placed on the stage using specially designed holder featuring magnetic clamps on V-grooves. Before the phase mask an aperture is placed which screens the edges of the laser beam and selects the most homogenous part of it. The length of the aperture is 4mm. Adjustment of the energy density incident to the optical fiber is possible by altering the focusing of the beam using the cylindrical lens. The optical fiber is strained under 30-50g of tension in order to enhance its photosensitivity, through the building of axial stresses in its core [11]. The whole system is paced on latex isolating pads in order to prevent environmental vibrations from reaching the system. The energy of the first diffraction order is measured for estimating the energy density of the exposure and for monitoring online any changes that could originate from nonlinear absorption in the phase mask. Changes in the transmission or reflection spectrum of the inscribed fiber are measured online using an optical spectrum analyzer. The probing light is emitted by a superluminescent diode centered at 1530m.

The optical fiber exposed is the PS1250/1500 Boron-Germanium codoped optical fiber manufactured by Fibercore Ltd. U.K. Although the manufacturer does not provide quantitative data for the content of each dopant in the core, a paper by Nikogosyan, *et al*, [9] reports 10% mol Germanium content, but does not provide any data for Boron. The fiber's core diameter is 7.1 μm and its numerical aperture is 0.13.

4.1.4 Annealing setup

The furnace used for the annealing of the fibers was manufactured by Griffith corp. U.K. and has a temperature range from room temperature up to 1200°C. The heating element of this furnace is coiled around a ceramic tube of 25cm length and 4cm diameter. The temperature is controlled via a Eurotherm Series 4000 programmable controller and thermal feedback is provided to the controller via a Type K thermocouple. The sensing edge of the thermocouple probe was placed in contact with the Bragg grating of the optical fiber. The programmable controller provided the ability of repeatable ramping up and isothermal stages at equal temporal intervals. The Bragg grating was always positioned in the center of the furnace with the thermocouple at the same position.

Errors in the temperatures measured by the thermocouple lie in the range of 0.1 - 2°C. The annealing process was always carried out until no light was backreflected from the Bragg grating. Figure 4.4 illustrates the temperature rising schedule as it was programmed in the controller. The furnace was set to rise from room temperature to 100°C and stay there for 10min. Each subsequent step included a 100°C increase of temperature and a 10min stopover afterwards, until no light reflection was measured from the fiber. Refractive index changes of the grating were monitored online during the whole annealing process.

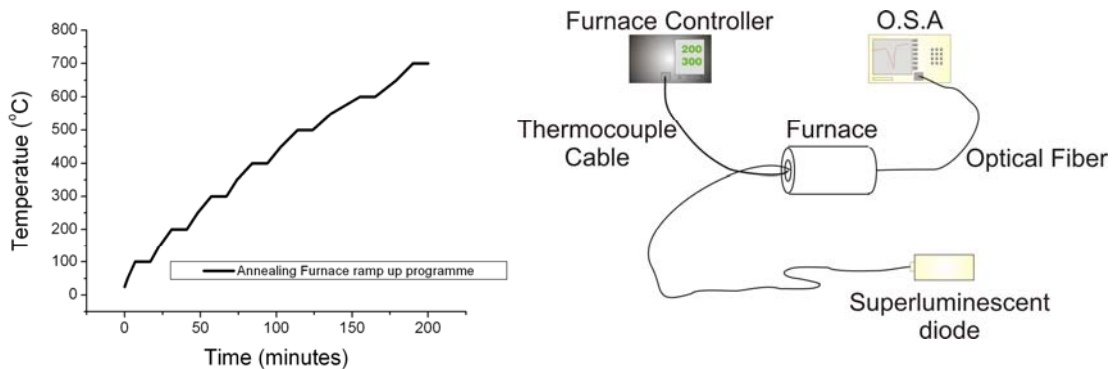


Figure 4.4 Temperature rising and thermal annealing setup

4.2 Recordings of Bragg gratings in B/Ge codoped optical fibers using 248nm ps and fs laser radiation

4.2.1 500fs inscriptions

The first exposures conducted for this thesis work, were realized with the 248nm 500fs KrF excimer laser described in 4.1.1. At this pulse duration, it was possible to achieve a maximum energy density of $50\text{mJ}/\text{cm}^2/\text{pulse}$ delivered before the fiber core, corresponding to an intensity of $100\text{GW}/\text{cm}^2$. Further increase of the energy density led to an abrupt rise of the nonlinear absorption in the phase mask (which is placed in close proximity to the optical fiber and thus accepting a very similar amount of energy density). Repetition rate was kept constant at $\sim 5.5\text{Hz}$. Results will be presented in terms of both modulated and average index changes in the fiber core. In the data presented it is assumed that refractive index changes take place only inside the fiber core region.

Initially, it is interesting to underline the different grating type formation regions and their initiation and termination points. Figure 4.5 illustrates the Bragg grating formation evolution during laser irradiation with a $50\text{mJ}/\text{cm}^2$, 500fs excimer laser pulse.

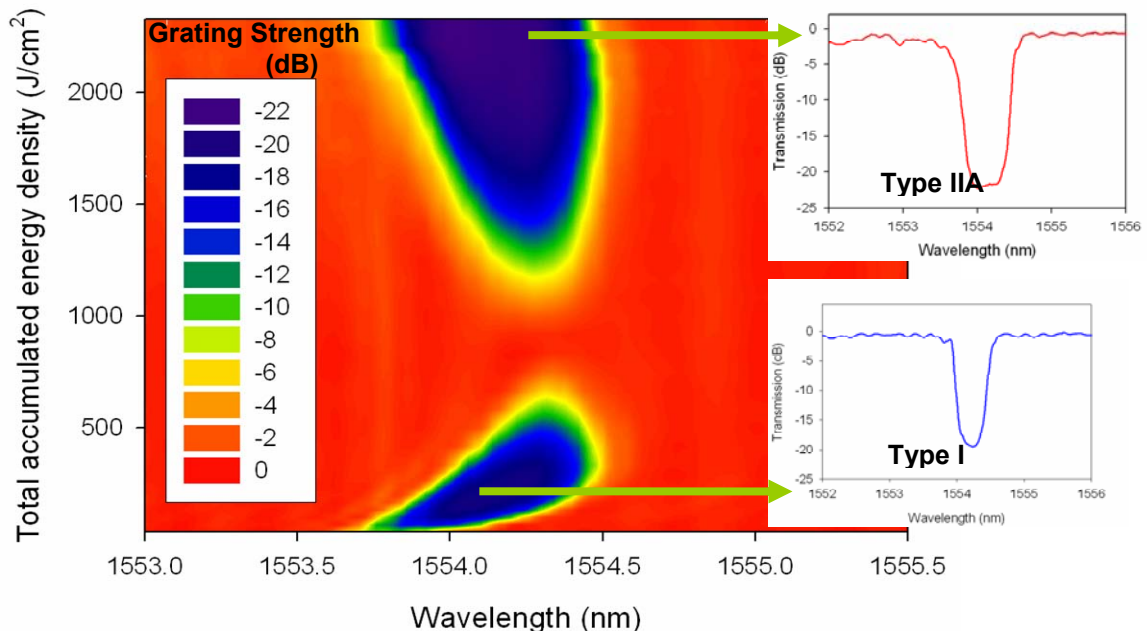


Figure 4.5 Bragg grating evolution of a grating inscribed with $50\text{mJ}/\text{cm}^2/\text{pulse}$, 500fs laser radiation.

During the early stages of exposure a Type I grating is formed. The growth of the grating is accompanied by a shift of the resonance wavelength towards the red part of the spectrum. This behavior has been attributed by Niay, *et al*, [10] to be the result of the gradual depletion of oxygen deficient centers and the subsequent formation of other defect types, which give rise to a positive refractive index change ($\Delta n > 0$). In the meantime, a different mechanism gives rise to negative index changes ($\Delta n < 0$), which are responsible for the erasure and subsequent formation of the Type IIA grating [10]. The formation of the Type IIA grating is accompanied by a small blueshift of the resonant wavelength, or no shift at all. The grating growth evolution will be examined for various 500fs inscriptions in terms of average and modulated changes in the graphs of Figure 4.6.

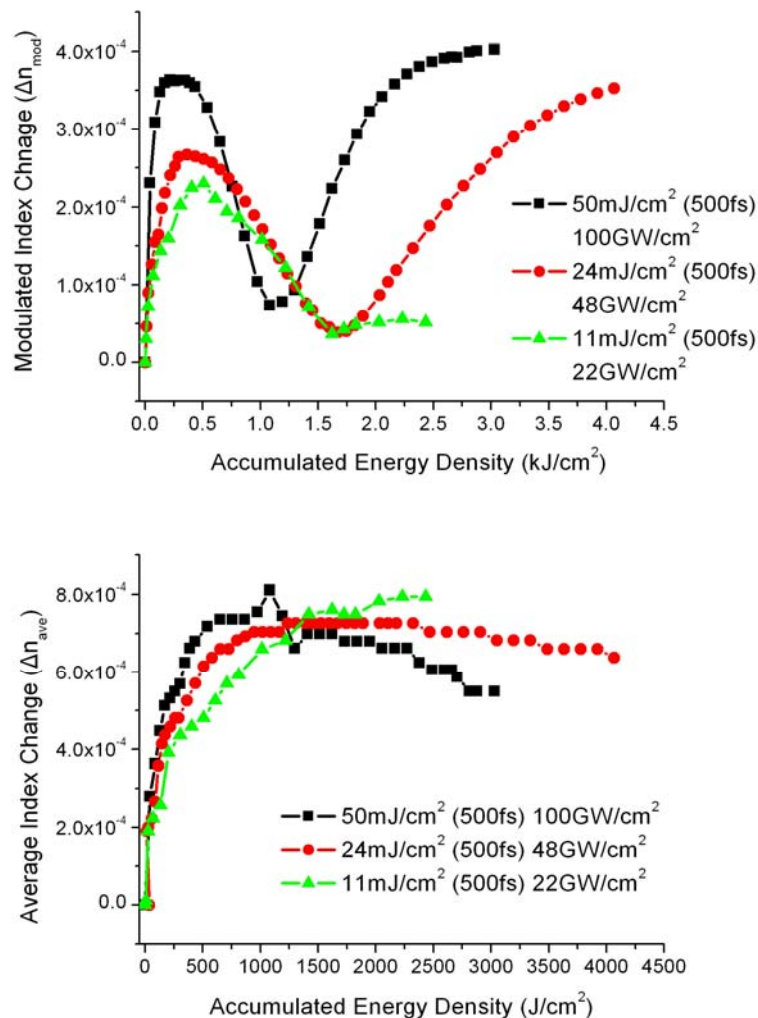


Figure 4.6 (a) Modulated index change versus accumulated energy density and (b) Average index changes versus the accumulated energy density incident to the fiber

From Figure 4.6a it is evident that the higher the energy density incident to the fiber the less accumulated energy density is needed to reach a specific refractive index change. The high intensity inscription ($100\text{GW}/\text{cm}^2$) exhibited the largest negative index changes (Figure 4.6b) which underlined the recording of a strong Type IIA grating (Figure 4.5.). Moreover, the results reveal that the lack of sufficient energy density per pulse can prevent the formation of a Type IIA grating, as that was shown for the case of the $11\text{mJ}/\text{cm}^2$ inscription, despite the fact that the pulse intensity was high ($22\text{GW}/\text{cm}^2$). The $22\text{GW}\cdot\text{cm}^{-2}/\text{pulse}$ inscription did not exhibit any decrease of its average index, since no Type IIA grating was formed. It should be noted that negative index changes take place since the early stages of the exposure, but they are not observable through the reflection or transmission spectrum because their amplitude is substantially lower than the positive ones. Their effect is manifested after the saturation of the Type I grating, when it starts being erased, as a consequence of the continuous growth of negative index changes which counterbalance the positive index changes. The effect of the energy per pulse is easily observable in Figure 4.6a, where doubling the intensity leads to a 2 times faster inscription in the Type I region and almost 4 times faster in the Type IIA region.

In order to investigate the effect of core composition on Bragg grating inscription, a recording was realized on a fiber without Boron codopant, but high Germanium concentration ($\approx 22\%$ GeO_2) [12, 44]. The intensity was kept close to $100\text{GW}/\text{cm}^2$ for direct comparison to the above $50\text{mJ}/\text{cm}^2$ grating inscription in B/Ge codoped optical fiber. The inscription results are presented in Figure 4.7.

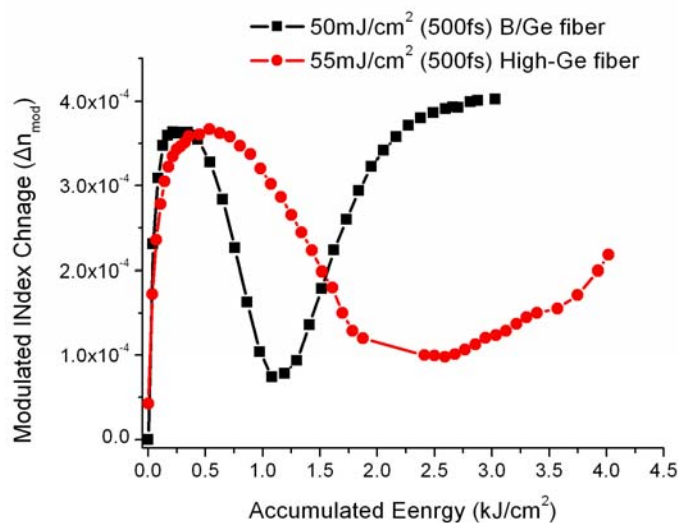


Figure 4.7 Modulated index change versus the accumulated energy density incident to B/Ge codoped optical fiber (square dotted line) and High-Ge fiber (circle dotted line)

Although the two fibers are irradiated with similar intensity per pulse ($100\text{GW}/\text{cm}^2$ versus $110\text{GW}/\text{cm}^2$) and with the same laser wavelength (248nm), there are substantial differences in the response of each fiber, especially in the Type I erasure and Type IIA formation region. Type I formation is generally agreed for germanium doped fibers under 248nm illumination to be heavily related to the depletion of oxygen deficient centers and the formation of color centers [13] which give rise to refractive index changes. Although the B/Ge fiber contains less than half the Ge concentration of the high-Ge fiber, both reach a similar amount of Type I modulated index change, indicating that Boron is enhancing the Type I photosensitivity regime, or that there is a ceiling of the achievable refractive index change through the depletion of GODCs. The different fiber composition plays a dominant role in the rate of negative index change creation, where the B/Ge codoped optical fiber exhibits a higher rate, as can be observed through the evolution of the Type I erasure and Type IIA formation regimes. This behavior is attributed to the presence of Boron which is known to alleviate stresses in the glass matrix and lower its transition temperature [43, 44].

4.2.2 Comparative nanosecond laser inscriptions

In order to study the effect of the intensity on the inscription process, a set of low intensity inscriptions was realized. The laser system used was the 248nm, 38ns KrF excimer laser described in 4.1.1. The energy density used for these inscriptions was ranging from $50\text{mJ}/\text{cm}^2$ to $450\text{mJ}/\text{cm}^2$. Under low energy density irradiation ($50\text{mJ}/\text{cm}^2$), the low intensity of the pulse ($11.84\text{MW}/\text{cm}^2$) was not sufficient to form a Type IIA grating in the optical fiber, indifferently of the irradiation dose. However, under 248nm 500fs irradiation the resultant high intensity of a $50\text{mJ}/\text{cm}^2$ pulse ($100\text{GW}/\text{cm}^2$) easily formed a Type IIA grating, underlying the important effect of intensity in refractive index engineering. Type IIA grating formation was observed under $450\text{mJ}/\text{cm}^2$ irradiation with the 38ns laser pulse. The results of the inscription process are presented in Figure 4.8, along side with the $50\text{mJ}/\text{cm}^2$ 500fs inscription.

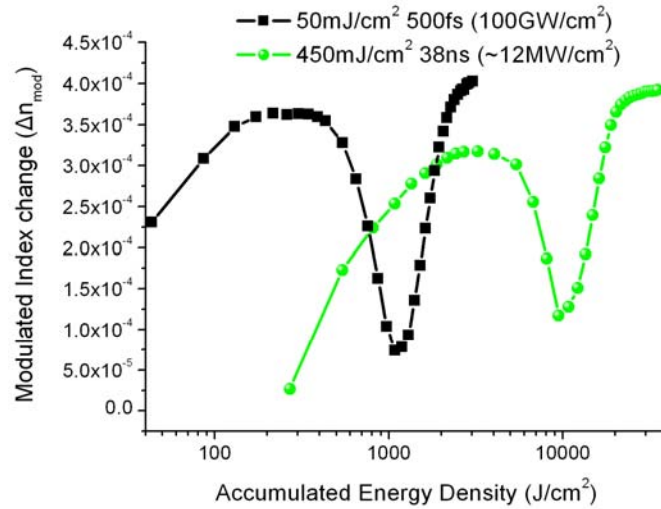


Figure 4.8 Comparison between the inscription efficiency using femtosecond and nanosecond laser radiation. Accumulated energy density scale is logarithmic.

Although the nanosecond inscription pulse has 9 times the energy density (thus, 9 times the number of photons per area) of the femtosecond, it takes an order of magnitude more accumulated energy to reach a specific refractive index change. This is a strong indication that the intensity is a key role factor in the recording process and high intensity pulses greatly accelerate the inscription process. It is also interesting to note that the low energy requirements of the high intensity inscription are evident in both Type I and Type IIA grating regions.

4.2.3 Comparative 120fs, 500fs and 5ps inscriptions

A more detailed picture of the effect of intensity in Bragg grating recording can be achieved by utilizing 120fs, 500fs and 5ps pulse durations for the 248nm wavelength. The effect of the intensity will be studied by conducting exposures using fixed/similar energy density per pulse and keeping the intensity fixed and adjusting the fluence. First, inscriptions using fixed/similar energy density are presented (Figure 4.9).

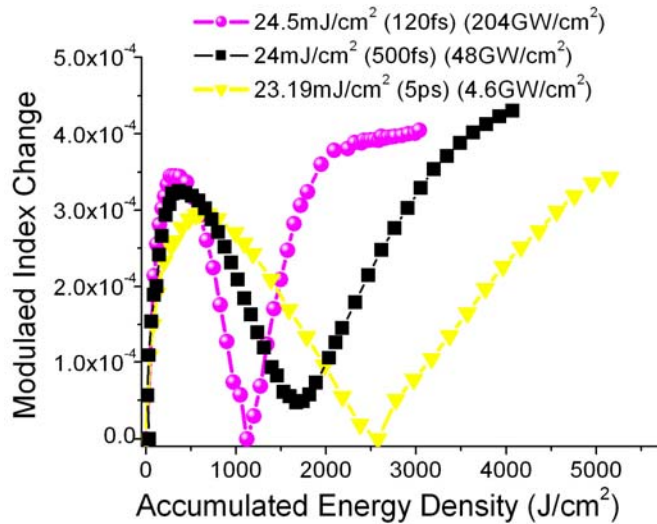


Figure 4.9 Inscriptions using similar energy density but different pulse duration

In all of the exposures realized, both Type I and Type IIA grating formation was observed. Higher intensities lead to faster grating formation both in Type I and Type IIA regions. However, the Type I behavior of the 500fs and 120fs inscriptions is very similar, indicating that the physical mechanism responsible is less intensity dependant and relies more on the energy density of the pulse. Large changes in inscription efficiency and speed are observed in the Type IIA region which is greatly accelerated by the higher intensities. This is clearly denoted by the slope after the saturation of Type I grating, which is increasing with increasing intensity (and consequently decreasing pulse duration). This slope corresponds to negative index changes formation [10]. Thus, negative index changes may be connected to a mechanism that is among others intensity sensitive.

Next, a set of inscriptions was realized using fixed intensity. For the first set a fixed intensity of $100\text{GW}/\text{cm}^2$ ($50\text{mJ}/\text{cm}^2$ - 500fs) was used (Figure 4.10a), while for the second one an intensity of $20\text{GW}/\text{cm}^2$ ($12.65\text{mJ}/\text{cm}^2$ - 120fs) (Figure 4.10b).

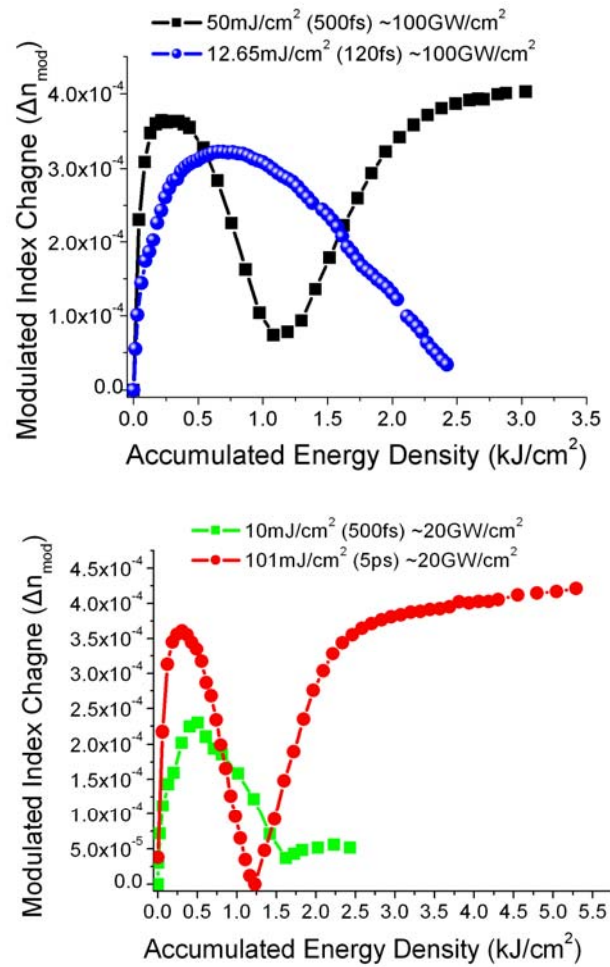


Figure 4.10 Comparative inscriptions using (a) $100 \text{GW/cm}^2/\text{pulse}$ and (b) $20 \text{GW/cm}^2/\text{pulse}$ intensity

In both cases the inscriptions realized with small energy density (12.65mJ/cm^2 for the case of 100GW/cm^2 exposures and 10mJ/cm^2 for the case of 20GW/cm^2 exposures) did not give rise to a Type IIA grating. This behavior could be attributed to the low photon content per area of these low energy density pulses that is insufficient to trigger the negative index formation mechanisms. This absence of Type IIA grating formation for those intensities and energy densities may be associated with thermal effects that may take place inside the fiber core. Greater energy densities lead to the induction of high temperatures in the bright fringes of interference, by single or multi-photon absorption. This rapid thermalisation is located in a small volume that is defined by the linear or non linear penetration depth for the 248nm radiation, in the B/Ge doped silicate core. The lateral dimensions of this heated volume are defined by the dimension of the bright interference fringe, that is estimated to be of the order of 250nm or smaller. It is also interesting to note that at the 20GW/cm^2 inscriptions, where the energy density per pulse of the two inscriptions has a difference of an order

of magnitude, the Type I regime exhibits large changes. The pulse containing the larger amount of photons ($101\text{mJ}/\text{cm}^2$) induces a larger amount of modulated refractive index change (3.7×10^{-4}) while the low energy density pulse managed to induce changes up to 2.5×10^{-4} . This observation is further reinforcing the high energy density dependence of the positive index changes.

More inscriptions realized with the above laser systems with different energy densities per pulse, verified the observation that high intensity inscriptions lead to faster Type IIA grating formation, while low energy density has an impact on both Type I and Type IIA grating formation.

4.2.4 Annealing results

The observation of the reflectance and transmittance spectrum of the fiber while it is irradiated is not sufficient to provide solid data on the physical mechanisms being behind the grating formation. Another indirect method of examining changes inside the fiber core is that of thermal annealing. Thermal stability data can be correlated with the demarcation of several photoinduced changes which can be of chemical, electronic or structural nature. In Figure 4.11 the annealing results of selected 38ns, 5ps, 500fs and 120fs inscriptions are presented.

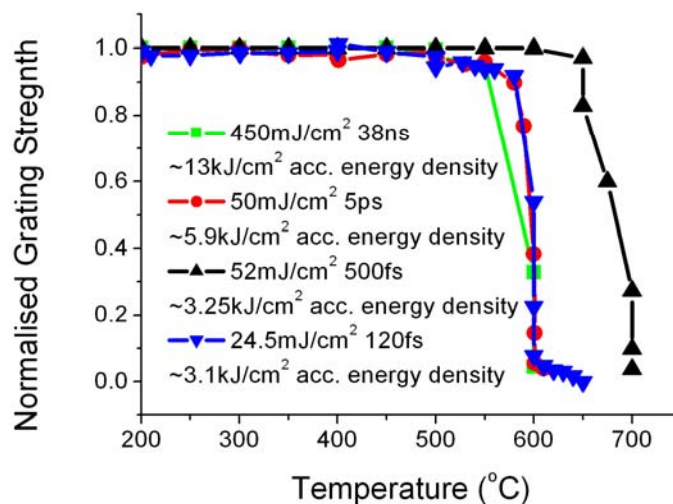


Figure 4.11 Thermal annealing results of fiber Bragg gratings inscribed using 248nm excimer laser radiation and various pulse durations

The most striking feature of the above figure is the thermal behavior of the $50\text{mJ}/\text{cm}^2$ 500fs grating. It exhibits an extended thermal stability of 100°C over the rest of the inscribed gratings. Enhanced thermal stability is also observed on the 120fs

inscription, although it has not the same magnitude of the 500fs one. For the 120fs case, a 10% of the grating strength is retained at 600°C, whereas the 5ps and 38ns gratings are totally erased at this temperature, despite being irradiated with pulses with larger energy densities. This remark leads to the speculation that high intensity pulses lead to structural changes inside the fiber core that can withstand higher temperatures. This observation leads to two conclusions. The first one is that the extended thermal stability observed for the case of the 500fs, 50mJ/cm² grating is not solely the result of the intensity of the pulse (100GW/cm²). In the recordings realized with the 120fs pulse duration, intensities up to 250GW/cm² were used and the magnitude of the extended thermal stability was lower than the 100GW/cm², 500fs case. The second conclusion, which is a consequence of the first, is the existence of a dependence of the extra thermal stability on the number of photons per pulse incident to the fiber. In order to verify that this enhanced thermal stability is not the result of damage in the fiber core or cladding (like in the case of Type II gratings [14]) a number of indicators were examined on the 500fs and 120fs fibers.

The first inspection was the checking of the overall transmittance of the fiber after the completion of the irradiation process. No degradation was observed for neither of the high intensity inscriptions, indicating lack of damage of the fiber structure. Then, a 632.8nm He-Ne CW laser beam was focused using a microscope objective inside the fiber core and the grating region was checked for side light scattering. No scattered light was observed reinforcing the claim of low or no damage. Finally, the optical fibers were checked for damage using an optical microscope capable of magnifying samples by 1000 times. However, no damage was visible in this case either. The above observations led to the conclusion that the thermal stability of the above gratings was not the product of extensive damage in the fiber structure. This unique behavior is indicative of a structural rearrangement inside the fiber core induced by the combination of high energy density and intensity [45].

Finally the behavior of the annealing of a Type I grating is presented in Figure 4.12. Here the different nature of the positive index changes induced during the inscription of the Type I grating component, exhibit a substantially lower thermal stability. This observation reinforces the model that negative index changes of the Type IIA gratings are structural changes, through densification of the glass network.

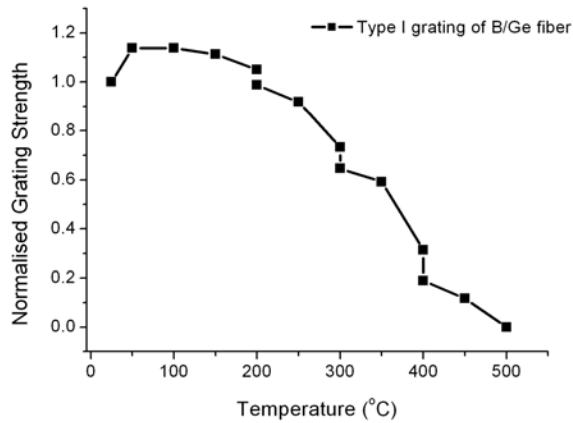


Figure 4.12 Annealing behavior of a Type I grating inscribed in a B/Ge codoped optical fiber using 248nm, 500fs laser radiation

4.2.5 Discussion

So far, the presented results include the refractive index evolution curves and thermal annealing behavior of Bragg gratings inscribed using 248nm laser radiation with varying intensities and energy densities. For most of the inscriptions realized, both Type I and Type IIA photosensitivity was observed. As stated in Chapter 3 the origin of Type I photosensitivity of B/Ge codoped optical fibers under 248nm illumination is mainly connected with the germanium oxygen deficiency centers that exist in the fiber core [15]. The absorption band of these defects peaks at 242nm, close to the 248nm laser wavelength. The color center model [1] seems to be ideal in modeling the Type I region through the Kramers - Kronig [16] relationship. However, under high intensities, there is an intensity effect to the Type I grating growth as can be seen in Figure 4.9. In this graph, the 5ps inscription achieves the lowest Type I index modulation, despite having a very similar energy density per pulse. This contribution to the grating growth could be attributed to non linear mechanisms which take place from the first pulse incident to the fiber and contribute to the index changes.

The effect of intensity, however, is greatly magnified in the regions of Type I grating erasure and Type IIA grating formation. These regions are dominated by a negative index change mechanism [10]. The negative index changes gradually counterbalance the positive index changes until the Type I grating is totally or partially erased and then the Type IIA grating is formed. The origin of this mechanism is generally agreed to be the structural change of the vitreous fiber core

[17]. The UV irradiation is causing compaction on the bright fringes of the irradiated grating pattern, while extensive volume compaction leads to dilation effects (Figure 4.13). The volume dilation is induced by radial and axial stress relaxation induced by the volume compaction in the bright fringes. This stress relief mechanism has to do with the nature of the drawing process of the B/Ge fiber. The addition primarily of B and secondarily of Ge in the silicate glass significantly reduces the glass transition temperature of the core matrix by several hundred degrees °C. Therefore during drawing the core is at superheated liquid phase leading to the creation of stresses in the core cladding layer upon rapid cooling.

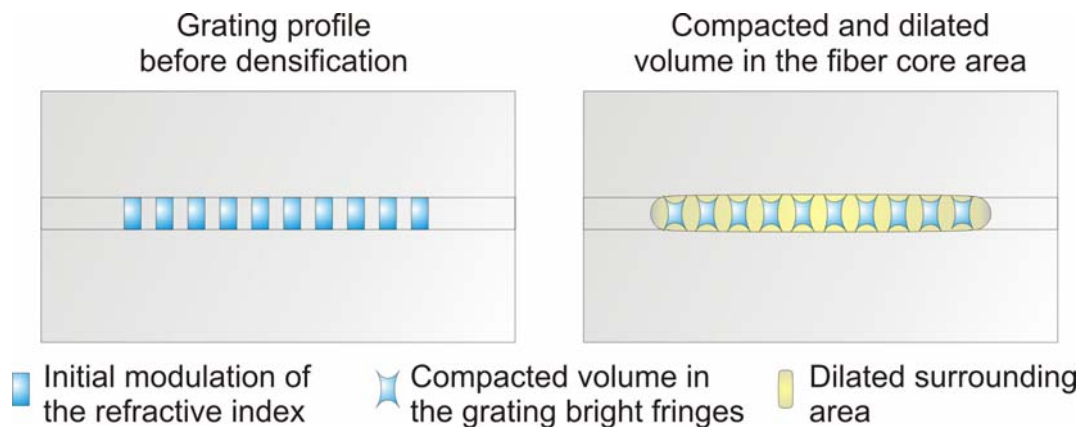


Figure 4.13 Compaction on the bright fringes of the irradiated grating pattern

The compaction in the bright fringes is attributed by Friebele and Higby to the cleavage of ring structures and the subsequent formation of smaller ring structures [21]. However, this is not the only mechanism causing the compaction, as compaction has also been related with the annihilation of the concentration of non-bridging oxygen hole centers [22]. Allan, *et al*, [19] have conducted measurements on the compaction of fused silica under 193nm radiation and found compaction to be analogous to the number of pulses (N) and the square of the intensity per pulse (I^2). Similarly, Schenker, *et al*, [20] studied compaction of fused silica under UV irradiation and found it to be analogous to $\kappa(NI^2)^c$, where κ and c are constants. The fact that densification is squarely dependant on the pulse intensity could be an indication of a two-photon process. The existence of a two photon absorption mechanism could also be speculated by the observation of the slope of negative index changes formation. The slope of this region (corresponding to the Type I erasure and Type IIA formation region) is greatly affected by the intensity as can be seen in Figures 4.6a, 4.9 and 4.10. Fitting the curve corresponding to the growth of the Type

IIA region to a simple linear function of the form $f(x) = a + b*x$ can reflect the slope of the curve in the b factor of the function. Thus, for the data in Figure 4.9 the b factors are: 120fs inscription $b= 5.13227E-7$, 500fs inscription $b= 2.2291E-7$ and 5ps inscription $b = 1.29144E-7$ (Figure 4.14). Taking into consideration the similarity of the energy density for these three exposures ($\sim 24\text{mJ}/\text{cm}^2$), the effect of the pulse intensity is evident through the steeping of the curve as smaller pulse durations are utilized for the inscription of the Bragg grating (the higher the b factor the steeper the curve). Similar changes in intensity do not seem to affect in the same magnitude the slope of the positive index changes. Thus, the negative index changes region seems to be dominated by a nonlinear mechanism that is highly responsive to intensity changes. Nonetheless a more detailed study on the existence of a two photon is required to reach rigorous conclusions.

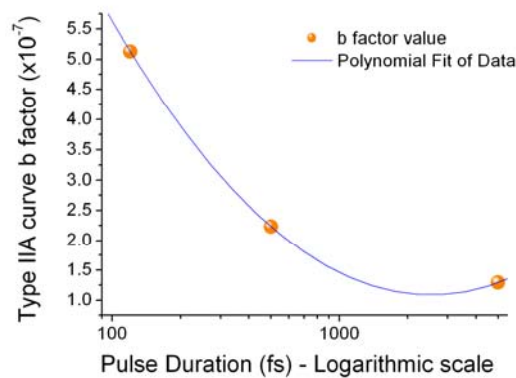


Figure 4.14 b factor values versus pulse duration for inscriptions using 120fs, 500fs and 5ps pulse duration

Concerning the effect of intensity in the inscription process, it is also important to note the extended thermal stability observed in the $50\text{mJ}/\text{cm}^2$, 500fs and the 120fs exposures. Assuming that the enhanced thermal stability is the product of a denser packing of the vitreous core, high intensities seem to promote an extra mechanism that gives rise to these denser structures. This mechanism is dependant on both the number of photons per unit area and the intensity of the pulse. This is easily confirmed by checking Figure 4.11 where the very high energy density 38ns pulse duration inscription did not exhibit enhanced thermal stability. Moreover, the high intensity, but low energy density $11\text{mJ}/\text{cm}^2$ was incapable of forming a Type IIA grating, a grating structure with enhanced thermal durability. The above remarks indicate that the mechanism responsible for the enhanced thermal durability is a multi parameter process. However, the exact nature of this mechanism is still unclear and

will be further discussed in conjunction with forthcoming Raman spectroscopy results.

4.3 Inscriptions using other laser wavelengths

The photosensitivity of an optical fiber and the underlying physical mechanisms can be further understood by irradiating the fiber with other laser wavelengths than the 248nm. The advantage of this approach is that the inscription efficiency of different laser wavelengths can be correlated with different defect types. This, in turn, can provide valuable information on the importance of the different mechanisms and indicate the existence of any additional ones. Apart from the 248nm wavelength, inscriptions were also realized using 193nm 10ns laser radiation. The results of these inscriptions are presented in Figure 4.15.

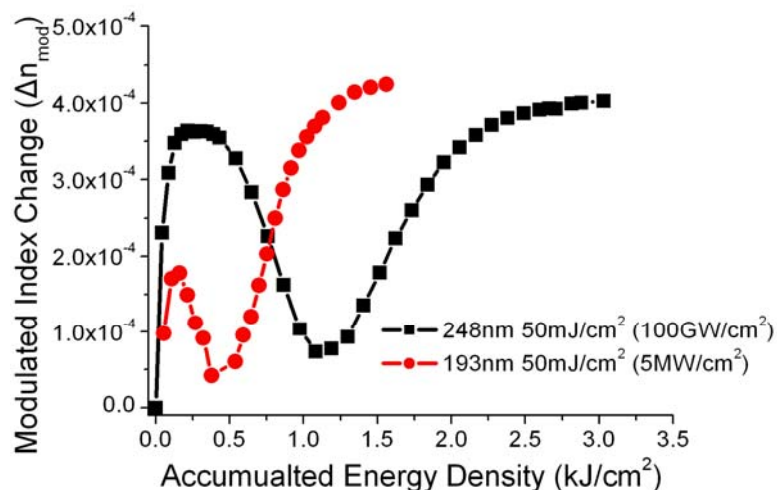


Figure 4.15 Bragg grating inscriptions realized on PS1250/1500 B/Ge optical fiber using various laser wavelengths, but similar energy densities

The differences induced by the various laser wavelengths are manifested throughout the whole inscription process. The type I component of the 248nm inscription is the one achieving the largest index change, while the 193nm the lowest. This behavior can be attributed to the overlap of the 248nm wavelength with the strong 242nm absorption band of Ge-doped fused silica [23]. 193nm laser radiation is the weakest in creating Type I defects despite having the largest energy photon (6.4eV). The nearest absorption band of Ge-doped silica lays at 185nm and is correlated with GeE' centers [24].

The inscription efficiency, however, is substantially differentiated in the negative index changes regime. 193nm laser radiation required the least amount of energy to induce similar index changes compared to the other wavelengths. The reason for this behavior could be the high photon energy of this laser and its higher spatial coherence. The high photon energy promotes two-step absorption and the high coherence of the laser provides high fringe contrast.

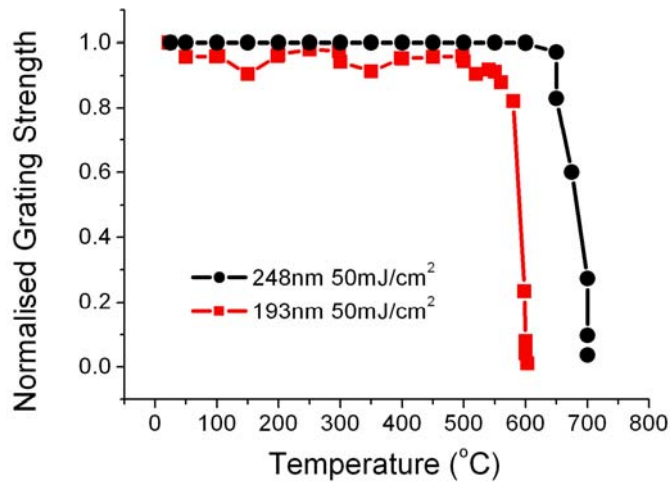


Figure 4.16 Annealing of the Bragg gratings inscribed using different laser wavelengths

From Figure 4.16 it is clear that the 193nm inscription did not demonstrate enhanced thermal durability, like the 248nm 500fs one. Although the photon energy of 193nm laser is larger than the photon energy of the 248nm laser, the large pulse durations available did not give rise to more rigid structural changes. The 193nm grating is erased at 600°C. Once again, the predominant role of the intensity in the thermal stability of the gratings is verified.

4.4 Unsaturated inscriptions of Type IIA gratings

This set of inscriptions was realized using the 248nm KrF excimer laser and the inscriptions were terminated before the saturation of the Type IIA grating component. The termination point was determined to be at a value of around $2.3 \times 10^{-4} \pm 0.3 \times 10^{-4}$ of modulated index change in the Type IIA region. This value corresponds to almost half of the modulated index change possible at the saturation region under similar exposure conditions. The idea behind these exposures is to examine the annealing behavior of the unsaturated gratings and observe possible grating growth through

thermally triggered mechanisms. The grating growth curves are presented in Figure 4.17.

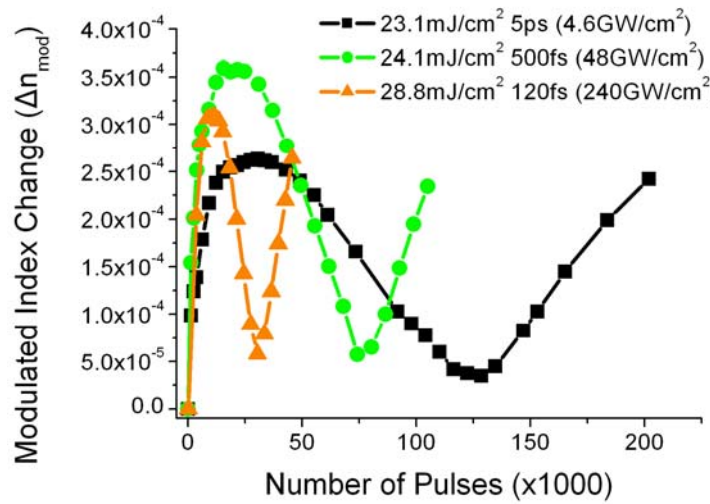


Figure 4.17 Unsaturated Bragg grating inscriptions using 248nm laser radiation and various pulse durations

High intensity pulses have led to substantially faster growth of negative index changes, as demonstrated in previous sets of exposures. A 10 time increase in the intensity per pulse halves the required number of pulses to form a similar index change in the Type IIA region, as can be seen for the case of the 5ps and 500fs inscriptions. Generally, the growth of the gratings does not exhibit any differences to the exposures presented in Figure 4.9, apart from the fact that grating growth was terminated before saturation. More interest exhibits the thermal annealing behavior of these gratings, which is presented in Figure 4.18.

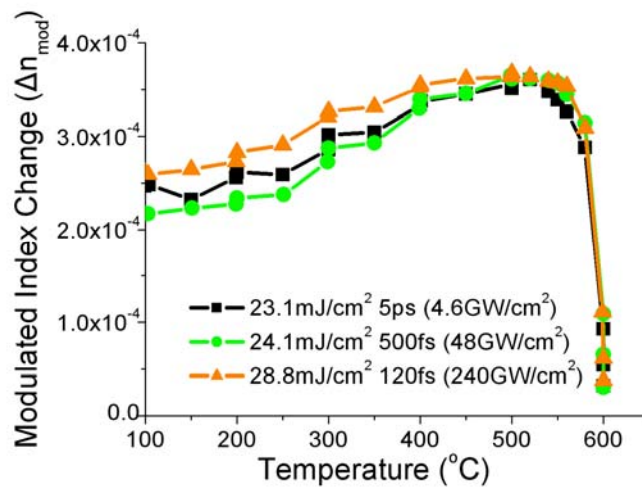


Figure 4.18 Thermal annealing behavior of Bragg gratings which were terminated before the saturation of refractive index changes in the Type IIA region

In the above Figure it is evident that as the temperature rises above 100°C, the modulated index change – and consequently the grating strength – is increased. This monotonic increase is continued until a temperature of 520°C is reached, which is also the temperature where the maximum index change has taken place, independently of the inscription intensity per pulse. Beyond the point of the 520°C the gratings are demarked in the same manner as a typical Type IIA grating, which is totally erased at 600°C. Such thermal annealing behavior has been reported before in the annealing of Bragg reflection inscribed in phosphate glass fiber using 193nm excimer laser radiation. Thermal amplification effects are usually associated with changes of the glass coordination on subsequent stress relaxation, in soft glass matrices characterized by low glass transition temperatures.

In the present case, structural changes initially induced in the glass matrix by the UV radiation are further progressing by the thermal annealing process. Another significant detail emerges from the annealing data of Figure 4.18 is related with evolution of the structural induced in the glass by the 248nm 500fs laser radiation. Since for the accumulation energy density provided, no enhancement of the thermal stability is observed (see gratings recorded using 25mJ/cm² 120fs and 50mJ/cm² 500fs), the structural effects that underline such thermal stability are probably formed during the late phases of exposure.

4.5 Raman scattering measurements

A deeper insight of the mechanisms underlying the grating inscription process can be achieved by employing comparative Raman scattering measurements of the core of pristine and irradiated optical fiber samples. The optical fibers were irradiated using 248nm 5ps, 500fs and 120fs pulse durations, while a pristine fiber was also examined. The fibers were irradiated without a phase mask with energy densities of 180mJ/cm², 90mJ/cm² and 56mJ/cm² for the 5ps, 500fs and 120fs pulse durations respectively. The energy density of each exposure was selected in a way to compensate for the doubling of intensity in the bright fringes of interference when using the phase mask technique. Thus, the above exposures correspond to the use of 90mJ/cm² for a 5ps exposure by employing a phase mask, 45mJ/cm² using 500fs pulse and 28mJ/cm² using 120fs pulse duration. The accumulated energy density

deposited in the fibers (normalized to compensate for the doubling in intensity using a phase mask) is identical to the one required to form a saturated Type IIA grating when using a phase mask. The probing beam of the Raman spectroscopy was the 473nm line of an Ar⁺ laser, illuminating the core of the exposed and unexposed fibers. Exposures were realized with a resolution of 1cm⁻¹ at a range from 84cm⁻¹ to 5193cm⁻¹. All of the resultant spectra were normalized to 800cm⁻¹, whose peak is associated with the Si-O-Si glass network structure [25] and which is expected to exhibit the smallest changes between the irradiated and the pristine samples. Results are presented in the range from 84cm⁻¹ to 1180cm⁻¹, where the peaks of interest are located (Figure 4.19).

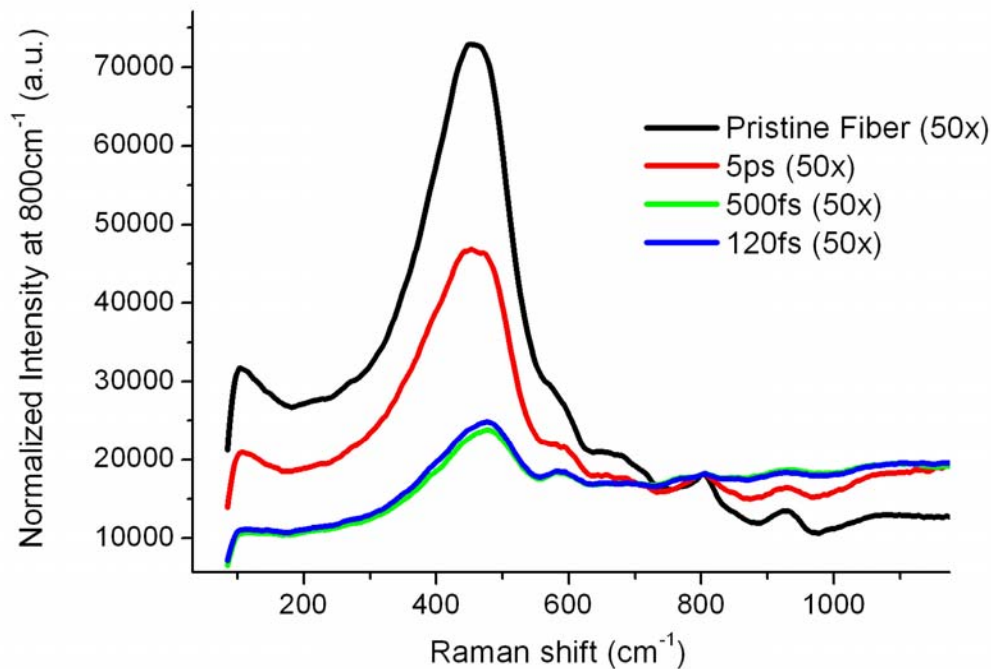


Figure 4.19 Raman scattering spectra of the core of various exposed and unexposed B/Ge optical fibers. In all cases excitation of the core comes from the 473nm line of an Ar⁺ laser and the microscope objective used has a magnification of 50x.

The black line in Figure 4.19 corresponds to the Raman scattering spectrum of the unexposed fiber, and it was the reference spectrum used for normalization of the other spectra at 800cm⁻¹. On the pristine fiber, the Raman spectrum features a strong peak at 452.6cm⁻¹. According to reference [25] there are two peaks near this vicinity at 435cm⁻¹ and at 480cm⁻¹. The first peak at 435cm⁻¹ is associated with the stretching of sixfold ring structures of SiO₄ and GeO₄ tetrahedra in the glass. The second peak at 480cm⁻¹ is associated with fourfold rings of SiO₄ and GeO₄. The appearance of a

broad peak in the pristine fiber centered somewhere between those two peaks can be attributed to the presence of both sixfold and fourfold ring structures in the pristine material. A broad curvature centered near 580cm^{-1} is also observed in the pristine sample. According to Galeener [25] this peak is caused by the threefold GeO ring (Ge-O-Ge). The next feature of the pristine fiber spectrum appears near 678cm^{-1} . According to Sharma, *et al*, [26] there is a peak centered at 670cm^{-1} associated with the Ge-O-Si structure. The feature located at 800cm^{-1} has already been discussed and was assigned to the glass network structure Si-O-Si [25]. The origin of the 927cm^{-1} peak is assigned by several researchers to borate groups [27] while some others [28] believe it is connected to the symmetric stretching mode of non-bridging bonds of SiO_3 chain units. Due to the fact that the optical fibers in this work contain Boron, the most probable origin of this peak is the B-O-Si bond stretching and bending vibration [33]. A minor peak centered at 1060cm^{-1} is connected by Furukawa, *et al*, [28] to the concentration of B_2O_3 in the silicate glass matrix. Finally, the second largest peak in the spectrum of the pristine fiber is located at 103cm^{-1} . This feature is called the boson peak [29] and it is usually correlated with long to medium range structural disorders in the glass matrix [30], [31].

Useful data can be extracted from Figure 4.18 by studying the relative changes of intensity and Raman shift of the various peaks of the irradiated fibers. Starting with the main peak at 452cm^{-1} , it is evident that the intensity of this peak is decreased with decreasing pulse duration and exhibits shifts towards larger inverse wavenumbers (see collective data in Table 4.2). This behavior has also been observed by Limberger, *et al*, [32], who associated it with the decrease of the order of the tetrahedron rings in the glass. The UV irradiation is causing cleavage of the large ring structures reducing them to lower order structures (i.e. sixfold rings reduced to fourfold, threefold or twofold rings). The shift towards higher inverse wavenumbers is further reinforcing this speculation, as the region above 480cm^{-1} is correlated with low order ring structures. Moreover, the strengthening of the 580cm^{-1} band which is related to threefold ring structures is another confirmation that UV irradiation is reducing the order of the ring structures. The utilization of high intensity pulses leads to larger changes in the spectra, indicating denser structures, due to the reduction of the number of manifold rings. The magnitude of the 670cm^{-1} peak is decreased after UV irradiation of the fiber and is almost totally flattened at high intensity inscriptions. Since this band is assigned to the Ge-O-Si structure, it is possible that UV irradiation

is cleaving the glass bonds, without exemption if they arise from Si-O or Ge-O units, leading to the formation of other defect types that in turn lead to denser structures. The 927cm^{-1} peak is also decreasing with increasing inscription intensity, proclaiming cleaving of the B-O-Si bonds [35]. The B_2O_3 peak centered near 1060cm^{-1} is gradually decreased until it is almost flattened for the case of 120fs irradiation, with subsequent shifts toward smaller inverse wavenumbers. According to Furukawa, *et al*, [28] this shift is indicating a reduction on the concentration of B_2O_3 in the glass matrix, a claim that is further solidified by the decrease of the relative intensity of the peak.

The boson peak centered at 103cm^{-1} is also decreasing with increasing irradiation intensity. This behavior could be attributed to the increase of order inside the glass matrix, as suggested in [31]. Hence, the flattening of this peak is speculated to be connected with a denser mesoscopic packing of the glass matrix. However, the nature of the Boson peak is complicated and a more rigorous explanation of its behavior would require Raman spectra from a range of less than 10cm^{-1} .

The data of this section indicate that there are significant differences between the amplitudes of structural changes of high (120fs and 500fs) and lower intensity irradiation (5ps). These spectral differences indicate that under high intensity exposures, the glass is packed into a denser configuration. However, the magnitude of the thermal stability enhancement is not the same for the 500fs and 120fs inscriptions, although their Raman scattering spectrum appears similar in form and amplitude. It is probable that differences would be observed in the region between 10cm^{-1} to 100cm^{-1} , where the structural order associated boson peak resides. If the enhanced thermal stability is related to a denser packing of the glassy matrix, the boson peak would most probably demonstrate the difference between the 500fs and 120fs inscriptions. Such capability was technically inevitable at the time of the measurements and this region will be studied in future experiments. Finally, in the subsequent sections, an examination of intensity related effects will be examined and a brief discussion will follow.

Table 4-2 Raman scattering data from the measurements realized on pristine fibers and fiber irradiated using 5ps, 500fs and 120fs pulses

	Boson Peak (100cm ⁻¹)	Six & Fourfold Ring (430-490cm ⁻¹)	Threefold GeO ring (580cm ⁻¹)	Ge-O-Si ring (670cm ⁻¹)	Unidentified Peak (925cm ⁻¹)	Boron Oxide Peak (1060cm ⁻¹)
	Si-O-Si ring (800cm ⁻¹)	Si-O-Si ring (800cm ⁻¹)	Si-O-Si ring (800cm ⁻¹)	Si-O-Si ring (800cm ⁻¹)	Si-O-Si ring (800cm ⁻¹)	Si-O-Si ring (800cm ⁻¹)
Pristine	1.758	4.037	1.528	1.14	0.745	0.716
5ps	1.159	2.593	1.207	0.975	0.912	0.981
500fs	0.594	1.319	1.016	0.938	1.034	1.0685
120fs	0.617	1.375	1.025	0.931	1.015	1.057

Raman shift (cm⁻¹)

	Boson Peak	Six & Fourfold Ring	Threefold GeO ring	Ge-O-Si ring	Unidentified Peak	Boron Oxide Peak
Pristine	103.5464	452.5988	595.3054	678.2294	927.0016	1061.9000
5ps	+5.7854	+1.9285	-3.857	+1.9285	+3.8569	-4.98
500fs	+13.4986	+25.0701	-13.4993	Disappeared	+3.8569	-19.7
120fs	+11.5708	+25.0701	-13.4993	Disappeared	+1.9285	-19.4

Relative intensity

	Boson Peak	Six & Fourfold Ring	Threefold GeO ring	Ge-O-Si ring	Unidentified Peak	Boron Oxide Peak
Pristine	Ref	Ref	Ref	Ref	Ref	Ref
5ps	Decreased	Decreased	Increased	Decreased	Decreased	Decreased
500fs	Decreased	Decreased	Increased	Decreased	Decreased	Decreased
120fs	Decreased	Decreased	Increased	Decreased	Decreased	Decreased

4.6 Intensity effects in the inscription process

So far, it has been demonstrated that the intensity of the inscription, alters both the speed of the recording process, as well as, the properties of the irradiated glass. Although Raman scattering spectra provided critical information concerning the structural changes inside the fiber core, the dynamics of these changes remain uncertain. Taking into advantage the various pulse durations available, a brief study of the effect of intensity is conducted.

Taking as a reference the inscriptions presented in Figure 4.9 (conducted using similar fluence per pulse but different pulse duration) it is useful to study at first the speed of creation of negative index changes. A reference point for this study is the point where the Type I grating is erased and Type IIA grating formation is starting to take place, referenced hereafter as the “turning point”. Shenker, *et al*, [20] proposed that two-photon occurrences are proportional to a dose parameter D which is analogous to the pulse counts times the square of the pulse fluence divided by the pulse length. (Dose parameter $\propto (NI^2 / \tau)^b$, where N is the number of pulses, I the fluence per pulse and τ is the pulse duration). This analogy can be exploited to study the trend of the inscription efficiency as the pulse duration is decreased. A logarithmic plot of the energy required to reach the turning point versus the pulse duration is presented in Figure 4.20. The plot points are fit to an exponential growth curve of the type: $y = ax^b$ that was first used by Patrick and Gilbert [34] to study possible two-photon absorption in the fiber.

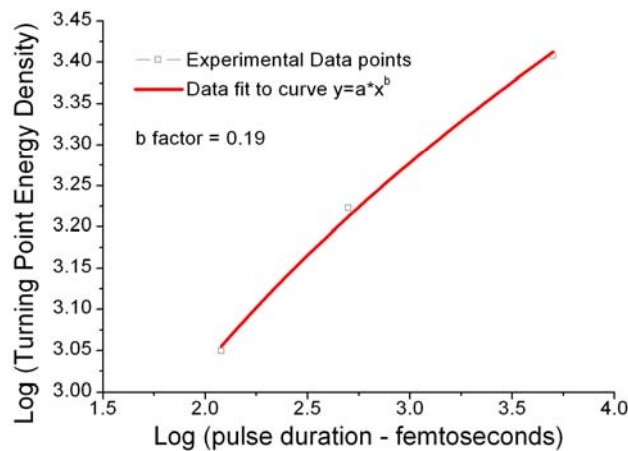


Figure 4.20 Power law fit of the accumulated energy required to reach the “turning point” under 5ps, 500fs and 120fs laser irradiation

The b factor in the work by Patrick, *et al*, [34] was found to have a value of 0.5, which has also been reported in the literature [35-36] for laser pulse durations longer than 10ps. However, for the intensity inscriptions realized in this work, the b factor is calculated at a value of 0.19. This change of value is most probably indicative of a nonlinear mechanism that is greatly enhanced by the high inscription intensities, or a nonlinear mechanism different to those exhibited under low intensity inscriptions.

Since the existence of non-linearities is strongly evident through the inscription results, the effect of intensity should also be accounted for possible thermal effects in the fiber core due to nonlinear absorption. The temperature increase ΔT in the bright fringes of the grating due to the irradiation process can be calculated by the equation [38]:

$$\Delta T \approx \frac{2Q_{pulse} (1 - 10^{-2a_{\lambda}r_{core}/10dB})}{C_p \rho \pi r_{core}^2} \quad (4.1),$$

where a_{λ} is the absorption coefficient of the fiber glass at 248nm, Q_{pulse} is the fluence of the laser beam at the core of the fiber, ρ is the glass density and C_p its heat capacity and r_{core} is the fiber core radius. High intensity irradiation however, can affect the absorption coefficient of the material resulting in a new nonlinear absorption coefficient of a higher value. Temperature changes in the core will be calculated for both low intensity inscriptions, where a linear absorption coefficient can be accounted for and high intensity inscriptions, where the use of a nonlinear absorption coefficient is more suitable. For the first case (low intensity inscription, linear absorption coefficient) the value of a is found from the literature to be 3000dB/cm at 248nm for a 10mol% Ge doped fused silica glass with Boron codopant [39]. A 2mol% Ge – SiO₂ glass preform exhibits at the same wavelength an absorption coefficient of 15.79dB/cm, stressing the significance of Germanium as a photosensitivity amplifier in the fiber core [40]. Applying to equation (4.1) a value of 450mJ/cm² for the fluence of the laser (corresponding to the nanosecond inscription realized), $a= 3000\text{dB/cm}$, $\rho= 2.405\text{g/cm}^3$ and $C_p=0.703\text{J}\cdot\text{g}^{-1}\cdot\text{K}^{-1}$ results in a temperature increase of 149°C. Taking into account a nonlinear component of the absorption coefficient ($\beta_{\lambda}=16.4\text{dB}\cdot\text{cm}^{-1}/\text{W}$) [41] the temperature increase in the bright fringes for the case of the 50mJ/cm², 500fs inscription can become as high as 322°C. The added contribution of both linearly and non-linearly induced temperature increases is significant enough to cause structural changes in the softened Boron doped glass. Thus, the accumulated thermal effect of

this temperature rise is possible to contribute to the thermal stability of the inscribed gratings through redistribution of the glass network to a more compact form.

4.7 Conclusions

A quick overview of the data presented in this chapter leads, first, to the understanding of the importance of intensity in the inscription process. A fixed value of refractive index change was reached substantially faster under high intensity irradiation, than for lower intensities. Negative index changes were more affected by the pulse intensity, than the positive ones, indicating that their formation involves a non linear mechanism. Nevertheless, the energy density of the recording pulse remains a dominating parameter, especially in the Type IIA regime. Lack of sufficient amount of photons per pulse will not give rise to Type IIA grating formation indifferently of the intensity of pulse. In short both intensity and energy density are critical to Type IIA grating formation. Moreover, thermal annealing of Bragg gratings inscribed with high intensity beams revealed pronounced thermal stability compared to gratings recorded using nanosecond pulse duration. The origin of this thermal stability was attempted to be traced, through exposures and annealing of unsaturated Type IIA gratings and retrieval of Raman scattering spectra of exposed and unexposed fibers. Raman scattering spectra revealed extended structural changes for the samples irradiated using 120fs and 500fs pulse durations. Finally, a brief study of the intensity impact in the inscription process clearly points the existence of nonlinear mechanisms during irradiation, but their nature is not yet fully understood. The dependence of the Type IIA refractive index changes obtained versus the pulse duration τ , does not follow the $\tau^{0.5}$ scaling rule that stands for pulse durations longer than 10ps [47], but the exponential factor is 0.19. This difference is further reinforcing the existence of a highly nonlinear mechanism. However, more work is required to clarify the nature of the nonlinear processes under intense UV irradiation and understand the origin of the structural changes inside the fiber matrix.

References

- [1] D.P. Hand, P. St. Russell, "Photoinduced refractive-index changes in germanosilicate glass", *Optics Letters* **15**: 102-104, (1990)
- [2] M. J. Yuen, "Ultraviolet absorption studies of germanium silicate glasses", *Applied Optics*, **21**: 136, (1982)
- [3] G. Violakis, M. Konstantaki, S. Pissadakis, "Accelerated Recording of Negative Index Gratings in Ge-Doped Optical Fibers Using 248-nm 500-fs Laser Radiation", *IEEE Photonics Technology Letters*, **18**: 1182, (2006)
- [4] B. Malo, K.O. Hill, F. Bilodeau, D.C. Johnson, J. Albert, *Electronics Letters*, **29**: 1668-1669, (1993)
- [5] G. Meltz, W. W. Morey, W. H. Glenn, "Formation of Bragg gratings in optical fibers by a transverse holographic method", *Optics Letters*, **14**: 823-825, (1989)
- [6] K. O. Hill, B. Malo, F. Bilodeau, D. C. Johnson, and J. Albert, "Bragg gratings fabricated in monomode photosensitive optical fiber by UV exposure through a phase mask", *Applied Physics Letters* **62**: 1035-1037, (1993)
- [7] G. Hernandez, "Fabry-Pérot Interferometers", *Cambridge University Press*, Cambridge, (1986)
- [8] Buchwald Kristian (2007) "Fused Silica Transmission Gratings", White Paper (available through www.ibsen-photonics.dk).
- [9] T. Ernst, D.N. Nikogosyan, "Single-quantum mechanism of Bragg grating inscription in a Ge/B codoped fibre by high-intensity 264nm femtosecond pulses", *Measurement Science and Technology* **18**: L1-L3, (2007).
- [10] P. Niay, P. Bernage, S. Legoubin, M. Douay, W. X. Xie, J. F. Bayon, T. Georges, M. Monerie and B. Poumellec, "Behaviour of spectral transmissions of Bragg gratings written in germania-doped fibres: Writing and erasing experiments using pulsed or CW UV exposure", *Optics Communications* **113**: 176-192, (1994)
- [11] N. H. Ky, H. G. Limberger, R. P. Salathe, F. Cochet, L. Dong, "UV-irradiation induced stress and index changes during the growth of type-I and type-IIA fiber gratings", *Optics Communications*, **225**: 313-318, (2003)
- [12] More information concerning the High-Ge Fiberlogix fiber can be found on <http://www.protodel.co.uk/>

- [13] D.P. Hand, P. St. Russell, “Photoinduced refractive-index changes in germanosilicate glass”, *Optics Letters* **15**: 102-104, (1990)
- [14] J. L. Archambault, L. Reekie, P. St. J. Russell, “100% Reflectivity Bragg reflectors produced in optical fibers by single excimer laser pulses”, *Electronics Letters*, **29**: 453-455, (1993)
- [15] J. Nishii, N. Kitamura, H. Yamanaka, H. Hosono, H. Kawazoe, “Ultraviolet-radiation-induced chemical reactions through one- and two-photon absorption processes in GeO₂-SiO₂ glasses”, *Optics Letters*, **20**: 1184–1186, (1995)
- [16] St. J. Russell, *et al*, “Optically induced creation, transformation and organization of defects and color centers in optical fibers”, *International Workshop on Photoinduced Self-Organization Effects in Optical Fiber*, Quebec City, Quebec, *Proceedings SPIE* **1516**: 47-54, (1991)
- [17] J. P. Bernardin, N. M. Lawandy, “Dynamics of the formation of Bragg gratings in germanosilicate optical fibers”, *Optics Communications*, **79**: 194-199, (1990)
- [18] M. G. Sceats, G. R. Atknis, S. B. Poole, “Photoinduced index changes in optical fibers”, *Annual Reviews in Material Science*, **23**: 381-410, (1993)
- [19] D. C. Allan, C. Smith, N. F. Borrelli, T. P. Seward III, “193-nm excimer-laser-induced densification of fused silica”, *Optics Letters*, **21**: 1960-1962, (1996)
- [20] R. E. Schenker, W. G. Oldham, “Ultraviolet-induced densification in fused silica”, *Journal of Applied Physics*, **82**: 1065-1071, (1997)
- [21] E. J. Friebele and P. L. Higby, *Laser Induced Damage in Optical Materials*, NIST Spec. Pub. 756, p. 89, (1987)
- [22] M. Rajaram, T. Tsai, E. J. Friebele, *Advanced Ceramic Materials* **3**: 598, (1988)
- [23] J. Albert, B. Malo, F. Bilodeau, D.C. Johnson, K.O. Hill, Y. Hibino and M. Kawachi, “Photosensitivity in Ge-doped silica optical waveguides and fibers with 193-nm light from an ArF excimer laser”, *Optics Letters*, **19**: 387-389, (1994)
- [24] M. J. Yuen, “Ultraviolet absorption studies of germanium silicate glasses”, *Applied Optics*, **21**: 136, (1982)
- [25] F. L. Galeener, “Planar Rings in Glasses”, *Solid State Communications* **44**: 1037, (1982)

- [26] S. K. Sharma, D. W. Matson, J. A. Philpotts, T. L. Roush, "Raman study of the structure of glasses along the join $\text{SiO}_2\text{-GeO}_2$ ", *Journal of Non-Crystalline Solids* **68**: 99-114, (1984)
- [27] W. L. Konijnendijk, J.M. Stevels, "Borate Glasses: Structure, Properties, Applications", edited by L.D. Pye, V.D. Frechette and N.J. Kreidl, *Materials Science Research*, **12**: 259, (1978)
- [28] T. Furukawa, W. B. White, "Raman spectroscopic investigation of sodium borosilicate glass structure", *Journal of Materials Science* **16**: 2689-2700, (1981)
- [29] K. L. Ngai, G. Floudas, A. K. Rzos, E. Riande, "Relaxations in Complex Systems", *Journal of Non-Crystalline Solids*, **307-310**: 73-160, (2002)
- [30] V. K. Malinovsky, A. P. Sokolov, "The nature of boson peak in Raman scattering in glasses", *Solid State Communications* **57**: 757, (1986)
- [31] B. Hehlen, E. Courtens, A. Yamanaka, K. Inoue, "Nature of Boson peak of silica glasses from hyper Raman scattering", *Journal of Non-Crystalline Solids* **307-310**: 87-91, (2002)
- [32] E. M. Dianov, V. G. Plotnichenko, V. V. Koltashiev, Y. N. Pyrkov, N. H. Ky, H. G. Limberger, R. P. Salathe, "UV-irradiation-induced structural transformation of germanosilicate glass fiber", *Optics Letters* **22**: 1754-1756, (1997)
- [33] N. Shibata, M. Horigudhi, T. Edahiro, "Raman spectra of binary high-silica glasses and fibers containing GeO_2 , P_2O_5 and B_2O_3 ", *Journal of Non-Crystalline Solids* **45**: 115-126, (1981)
- [34] H. Patrick, S. L. Gilbert, "Growth of Bragg gratings produced by continuous-wave ultraviolet light in optical fibre", *Optics Letters* **18**: 1484-1486, (1993)
- [35] T-E Tsai, G. M. Williams, E. J. Friebele, " Index structure of fiber Bragg gratings in Ge-SiO₂ fibers", *Optics Letters* **22**: 224-226, (1997)
- [36] M. Lancry, P. Niay, S. Bailleux, M. Douay, C. Depecker, P. Cordier, I. Riant, "Thermal stability of the 248-nm-induced presensitization process in standard H₂-loaded germanosilicate fibres", *Applied Optics* **41**: 7197-7204
- [37] L. V. Keldysh, *Soviet Physics JETP* **20**: 1307, (1965)
- [38] P. J. Lemaire, A.M. Vengsarkar, W. A. Reed, D. J. DiGiovanni, "Thermally enhanced ultraviolet photosensitivity in GeO_2 and P_2O_5 doped optical fibers", *Applied Physics Letters* **66**: 2034-2036, (1995)

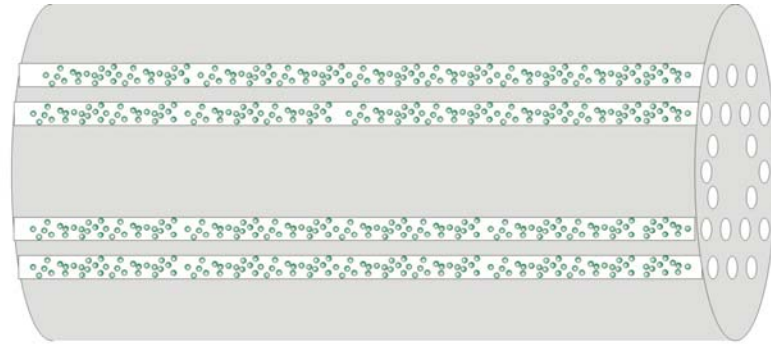
- [39] J.-M. Archambault, “Photorefractive gratings in optical fibers”, *Thesis submitted for the degree of Doctor of Philosophy*, University of Southampton, (1994)
- [40] A. Anedda, C. M. Carbonaro, R. Corpino, A. Serpi, “Absorption spectrum of Ge-doped silica samples and fiber preforms in the vacuum ultraviolet region”, *Journal of Non-Crystalline Solids* **280**: 281-286, (2001)
- [41] A. Dragomir, J. G. McInerney, D. N. Nikogosyan, “Two-photon absorption properties of commercial fused silica and germanosilicate glass at 264 nm”, *Applied Physics Letters* **80**: 1114-1116, (2002)
- [42] G. Violakis, M. Konstantaki, S. Pissadakis, “Accelerated Recording of Negative Index Gratings in Ge-Doped Optical Fibers Using 248-nm 500-fs Laser Radiation”, *IEEE Photonics Technology Letters*, **18**: 1182, (2006)
- [43] J. E. Shelby, “Effect of radiation on the physical properties of borosilicate glasses,” *Journal of Applied Physics*, **51**: 2561–2565, (1980)
- [44] D. L. Williams, B. J. Ainslie, J. R. Armitage, R. Kashyap, and R. Campell, “Enhanced UV photosensitivity in boron codoped Germanosilicate fibers,” *Electronics Letters*, **29**: 45–47, (1993)
- [45] C. W. Smelser, S. J. Mihailov, D. Grobnic, “Formation of Type I-IR and Type II-IR gratings with an ultrafast IR laser and a phase mask”, *Optics Express* **13**: 5377-5386, (2005)
- [46] J. D. Prohaska, E. Snitzer, and J. Winthrop, “Theoretical description of fiber Bragg reflectors prepared by Fresnel diffraction images”, *Applied Optics* **33**: 3896-3900, (1994)
- [47] B. C. Stuart, M. D. Feit, A. M. Rubenchik, B. W. Shore, M. D. Perry, “Laser Induced Damage in Dielectrics with Nanosecond to Subpicosecond Pulses”, *Physical Review Letters* **74**: 2248-2252, (1995)

5. Bragg Grating Inscriptions in Microstructured Optical Fibers

In the second experimental part of this thesis, the results on the Bragg grating inscription in commercial microstructured all silica optical fibers (MOFs) will be presented. The ultimate goal to be achieved with these experiments was to etch a relief grating profile in the holey matrix of the fiber so that – for the first time ever – a relief grating could be formed in a MOF. Such grating structures would exhibit refractive index changes of the order of around 0.46 (the difference of the refractive index of silicate glass and air). These changes are orders of magnitude higher than refractive index changes formed using standard photosensitivity inscription techniques, which reside in the region between 10^{-4} to 10^{-2} . Successful fabrication of such high index change gratings would give rise to novel, high sensitivity, optical sensors and highly tunable optical devices. Moreover these gratings would withstand temperatures of up to 1200°C, which is the glass transition temperature in fused silica.

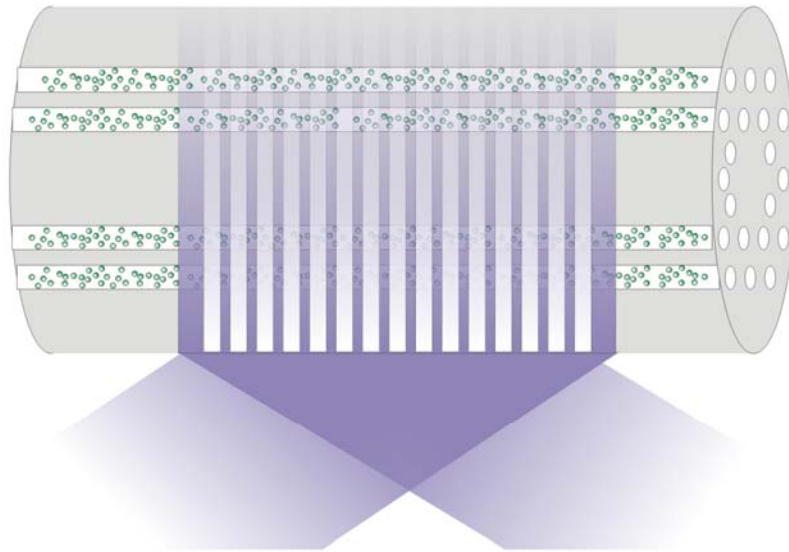
A setup capable of realizing this idea would roughly involve a gas absorbing at a specific wavelength leading to gas photodissociation, with specific reactive products, which in turn react with the silicate matrix of the fiber. This reaction would allow the local dissociation of the glass matrix to volatile gas products. The interference pattern of the phase mask would let these reactions happen only at the bright fringes of interference, resulting in a periodic structure with a period half of the phase mask pitch. This way a relief grating would be formed inside the holey region of the fiber. The whole concept of this idea is depicted in Figure 5.1. In order to verify the plausibility of the above idea a side-experiment was decided to be set up. This setup would involve a custom built vacuum chamber, where the etching gas would be infused. The chamber would feature a silica glass of high purity resembling the photonic crystal fiber host material. The silica glass will be in contact with the etching gas, and after UV irradiation, the effect of any photochemical reaction will be studied. This side experiment will be the first to present and discuss because of its “proof-of-concept” nature. Afterwards, the Bragg grating inscription setup in microstructured optical fibers will be presented, along with the results it produced. A short discussion will follow with conclusions and suggestions for future experiments and improvement of the setup.

1)



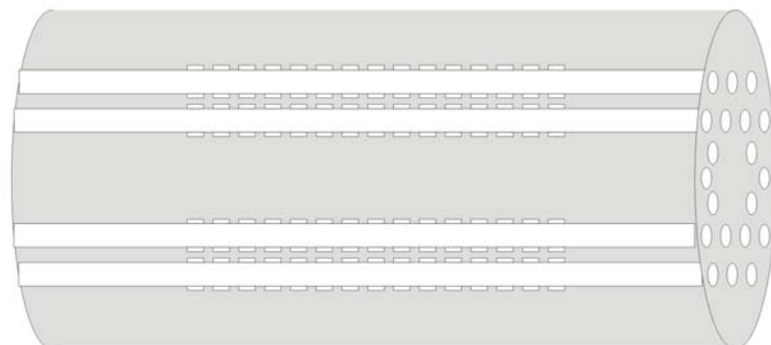
Microstructured optical fiber with gas flooded capillaries

2)



Exposure of the fiber to an UV interference pattern

3)



Etching in the bright fringes of the interference pattern

Figure 5.1 Illustration depicting the idea behind relief grating formation in MOFs

5.1 Experimental setup

5.1.1 Backside gas etching exposures on flat, thin fused silica bulks

A specially designed chamber was designed and manufactured for performing initial backside gas etching exposures on thin SiO₂ wafers. A 3 dimensional drawing of the chamber is presented in Figure 5.2. The front circular window of the chamber is removable, as well as, the cylindrical window holder for the straightforward removal of the sample window and the cleaning of the chamber cavity. A gauge at the top of the chamber is used for monitoring the pressure. The chamber has an input and an output socket, one for filling up and another for evacuation. The chamber is made of stainless steel alloy and the glass sample window is sealed using viton o-rings on both sides.

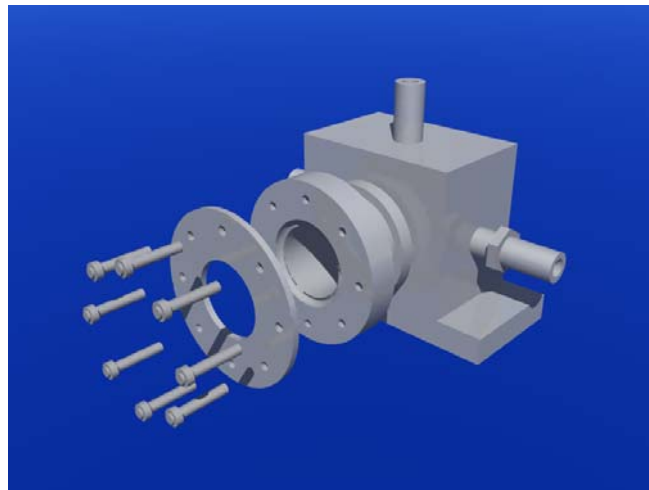


Figure 5.2 Schematic representation of the chamber used for the backside etching exposures

The chamber itself is clamped in a tilt stage providing fine adjustment of the x, y and θ angle. This is a crucial adjustment, because the fused silica window of the chamber must be perfectly parallel aligned to the phase mask. The requirement of contact between the phase mask and the chamber window is met by adding an x-stage to the chamber. This micrometric stage can place the window in contact or in close proximity to the phase mask with an accuracy of 50 μ m. Moreover, the phase mask is held in position using a custom holder specially designed for fitting onto the chamber setup. A layout of the whole setup is illustrated in Figure 5.3.

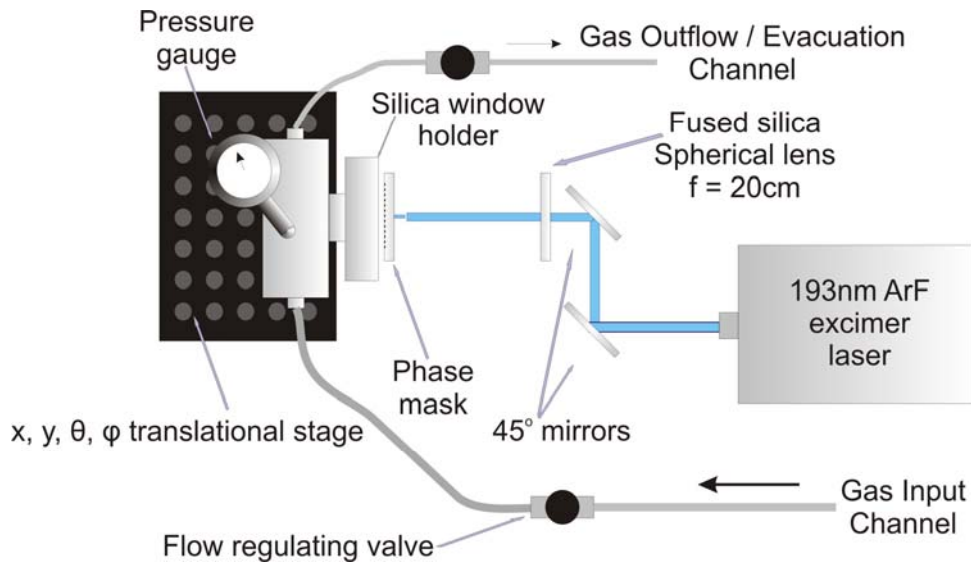


Figure 5.3 Backside gas etching setup of fused silica windows under 193nm laser irradiation

The phase mask used was optimized for 193nm illumination and has a pitch of 1070nm, resulting in grating recording with 535nm periodicity. It is manufactured by Ibsen Photonics [1], and transmits less than 1% of the incident power at the 0th diffraction order. The phase mask material is UV-grade fused silica. The laser system is the ArF excimer laser described in Chapter 4. A set of two highly reflecting 45° mirrors was utilized in order to guide the laser beam towards the grating recording setup. The laser beam is focused into the chamber window using an $f=20.0\text{cm}$ spherical lens. The energy density of the exposure is adjusted by introducing an attenuator into the path of the beam. A breadboard standing on vibration dampening pads is hosting the whole setup for providing vibration isolation. Finally, gas pumping in the chamber is realized by using an oil free mechanical pump and the gas infusion takes place directly via the gas bottle and gas regulation valves.

The experimental procedure involves the removal of the window holder of the chamber, its thorough cleansing and the careful placement of the fused silica window to be irradiated. Then, the chamber is evacuated until a pressure of the order of a few millibars is reached. This ensures a relatively high purity environment for the gas to enter. Afterwards, the gas is gradually inserted into the chamber until the desired pressure is reached. At this point the chamber is ready to be irradiated. When the irradiation of the window is finished, the gas is vacuumed and the chamber filled with air. The glass window can then be removed and obtained for analysis.

5.1.2 Bragg grating inscription setup in Microstructured Optical Fibers

The challenge of inscribing relief gratings inside a holey fiber using gas flow is the design of a special adaptor that will allow the flow of gas inside the fiber holes, without leakage at the connection points. Apart from this special component, the experimental setup layout does not greatly vary from the one used for the step index B/Ge codped fiber. The inscription UV beam is provided by the same laser used for the backside gas etching setup, the 193nm, 10ns ArF excimer laser. The Bragg grating inscriptions were performed using the phase mask technique in contact mode, as in the step index fiber case. An illustration of the inscription setup is presented in Figure 5.4.

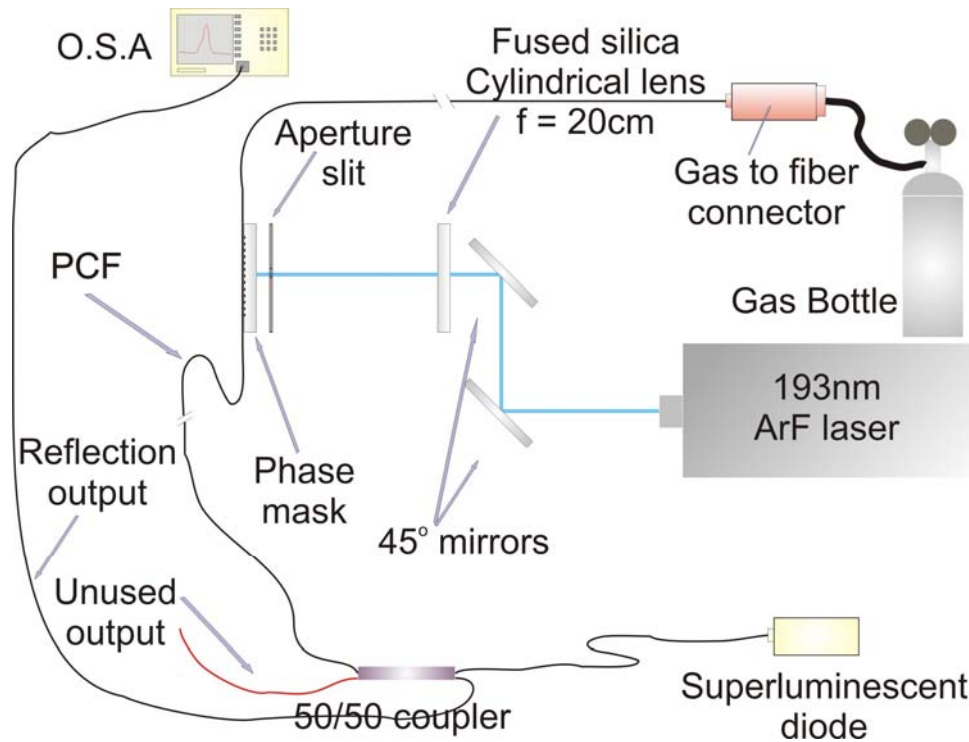


Figure 5.4 Experimental setup for Bragg grating inscription in MOFs with gas input

The UV-grade fused silica phase mask used was optimized for 193nm illumination with a period of 1070nm. Typical distances between the phase mask and the fiber were of the order of 100 μ m. Maximum intensity value reached for the grating recordings was 23MW/cm² with a pulse energy density of 230mJ/cm². Nonlinear absorption in the phase mask prevented any further elevation of the intensity since permanent damage would occur. The repetition rate used was 40Hz. The laser beam was focused into the fiber along the vertical axis using a 20.8-cm CaF₂ cylindrical lens. A 4x4mm² aperture was used to select the most homogenous

part of the beam, resulting into 4mm long Bragg gratings. The inscription process was monitored online using a superluminescent light source and an optical spectrum analyzer. Because of the nature of the experiments, when gas was inserted inside the fiber, no fiber transmission monitoring could take place, because one end of the fiber was coupled to the custom designed connector illustrated in Figure 5.5. This connector was directly connected to the gas bottle.

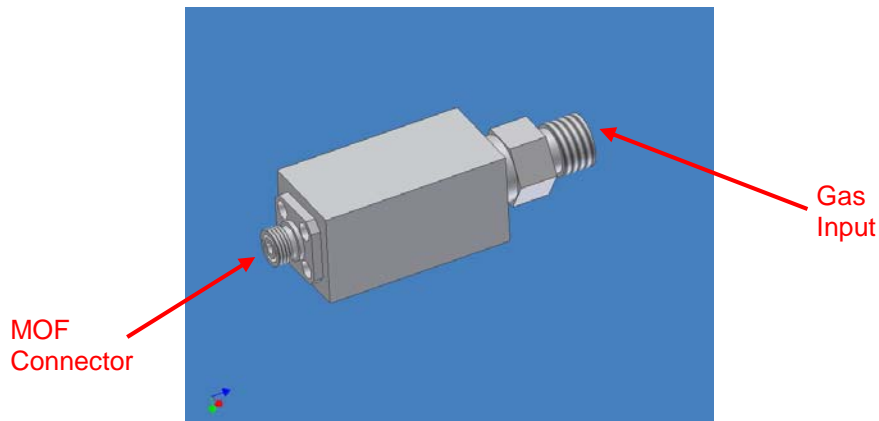


Figure 5.5 Custom MOF gas connector

The other end of the fiber was coupled to a standard SMA connector for probing light into the fiber and getting reflection spectra with the help of a 50/50 directional coupler. A commercial microstructured optical fiber (ESM-12-01 Crystal-Fibre, UK) was used for the exposures. The structure of the fiber is illustrated in Figure 5.6. The above fiber has a total of 54 air holes with a diameter of $3.68\mu\text{m}$ each and $8\mu\text{m}$ center to center distance between them.

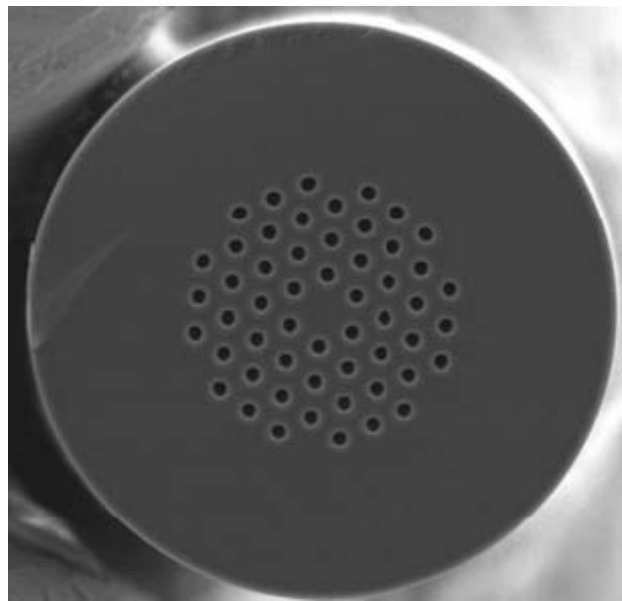


Figure 5.6 SEM image of the ESM-12-01 MOF from Crystal Fibre

The layout of the air holes results in a symmetrical hexagonal structure. The fiber has a solid core of 12 μ m diameter and attenuation at 1550nm of less than 0.8dB/km, indicating a high quality glass [2]. For the annealing process of the inscribed gratings, the programmable tube furnace that was described in Chapter 4 was used. Constant ramping up times with 10min intervals per 100°C were set for all gratings inscribed.

5.2 Computer Simulations for Side Illumination of the Microstructured Optical Fibers

The complex geometry of the holey microstructured fibers raised questions on the distribution of the energy of the inscription beam to the fiber hyperstructure. The holey matrix of the fiber is scattering and diffracting the incident radiation reducing the amount of energy deposited in the fiber core. Moreover nonlinear absorption in the fiber can further reduce the energy that reaches the core. In order to quantify the scattering and diffraction of light inside the fiber structure, a commercial ray tracing program was used [3]. A rigorous quantification of nonlinear absorption effects was possible by using a commercial program based on the finite difference time difference domain method [4-5].

The ray tracing simulation was capable of providing data in terms of linear losses of the beam energy density as it propagates throughout the MOF. The simulation was setup as follows. The experimental setup was modeled in the ray tracing program and analyzed in terms of energy density variations throughout the fiber core. An energy detector was placed right before the MOF and another one inside the fiber core. A third was placed inside the inner ring of air holes of the fiber structure. The program was set to simulate the propagation of half a million light rays of 193nm wavelength and illustrate 500 of them in the visualization window, depicted in Figure 5.7.

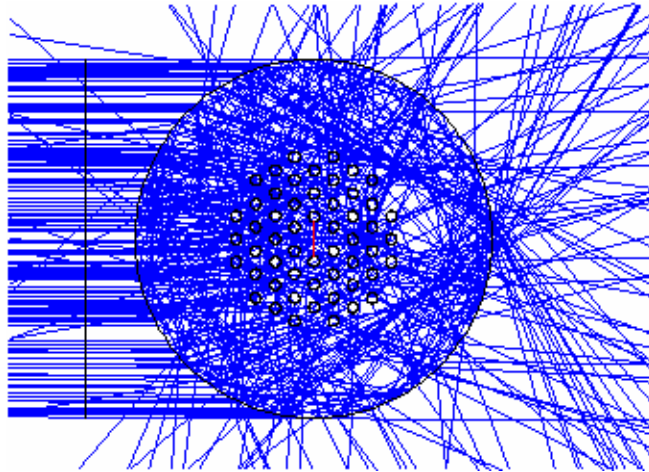


Figure 5.7 Ray tracing simulation of the propagation of the UV beams incident to the microstructured optical fiber

The detector window before the MOF appears as a long black hairline on the left side of the window and the detector inside the fiber core appears as a red hairline. Scattering from the air holes is taken into consideration, as well as scattering from the fiber cladding boundary. The peak irradiance was calculated from the program to be $24.17\text{MW}/\text{cm}^2$, while in the fiber core it's reduced down to $16.46\text{MW}/\text{cm}^2$. The above figure suggests a 31.9% decrease of energy density delivered in the fiber core.

The situation in the air holes, though, is different. The detector placed inside a hole of the inner ring of holes (the ones adjacent to the fiber core) gave off a 50% increase of energy density in that region. This is most probably the result of beam focusing due to the hole curvature. Such large deviations of energy density in the vicinity close to the fiber core can result non-uniformities of the refractive index changes.

Both linear and nonlinear absorption in the fiber was estimated by using the finite difference time difference domain method. Due to the large memory requirements of the FDTD method, the simulation was set up for 248nm illumination. Pulse duration was set to 500fs and material properties (including non linear refractive indices) were automatically set from the software's built in catalogues. The resultant energy distribution is illustrated in Figure 5.8.

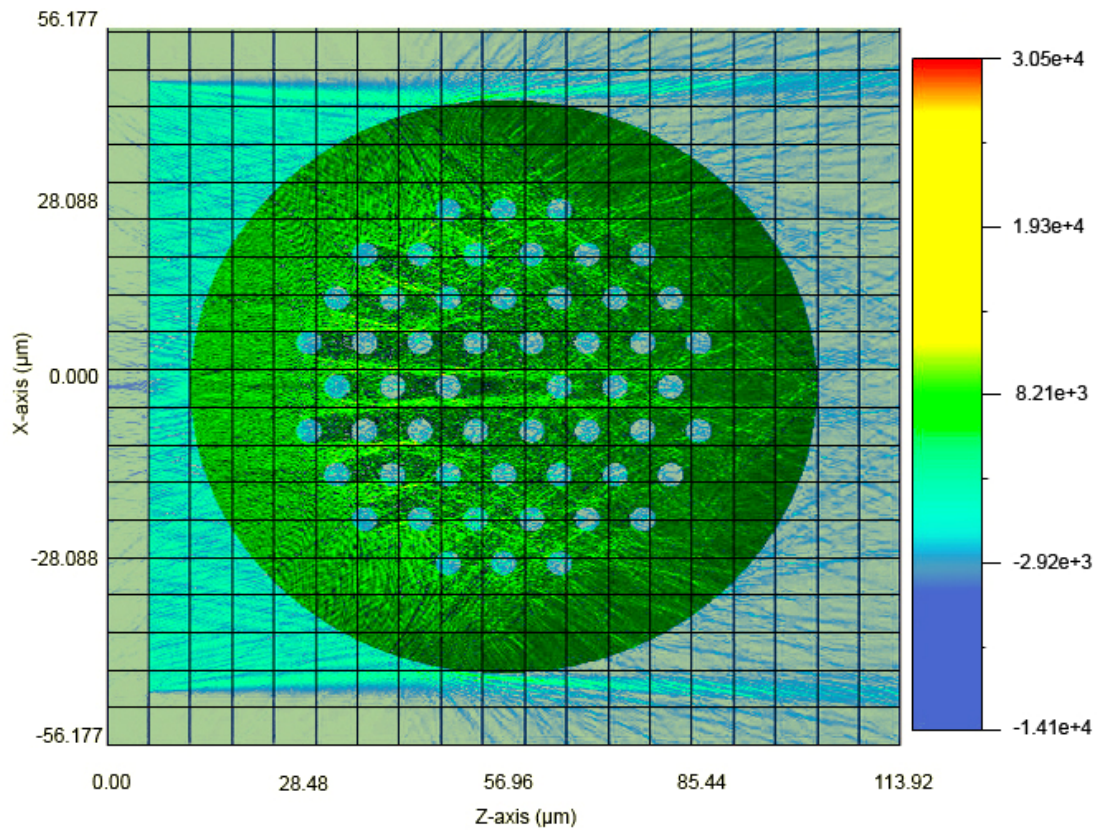


Figure 5.8 FDTD simulation of 248nm 500fs pulse propagation through the ESM-12-01 optical fiber

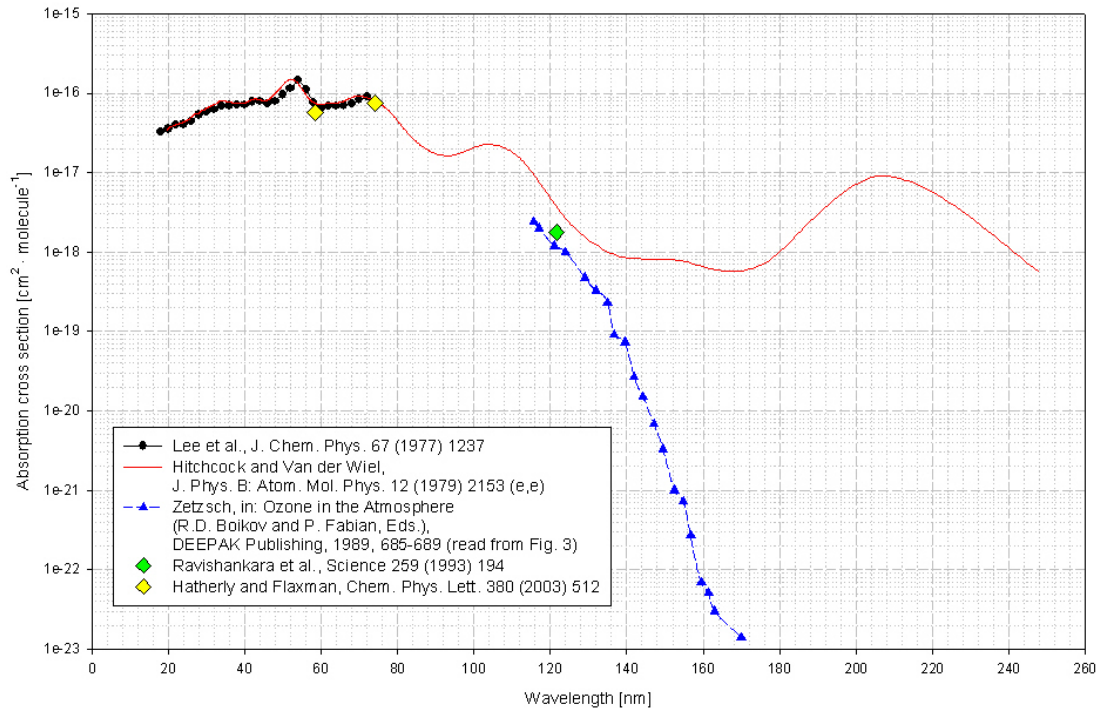
The FDTD simulation resulted in a 45% drop of energy density in the core. Taking into account that fused silica is less transparent at 193nm this percentage could be further increased. Increased energy density is also evident in the inner holes region, agreeing with the results of the ray tracing simulation.

Both simulations demonstrate a drop of the energy density in the fiber core region. The origin of the loss of energy is the scattering and diffraction of light in the holey region of the fiber. Nonlinear absorption in the fiber material introduces a further drop of energy, resulting at energy densities reduced up to 45% (and maybe more at shorter wavelengths). The results of these simulations will be later used to interpret several observations.

5.3 Backside gas etching irradiation results in slab samples

5.3.1 Etching gas – SF₆

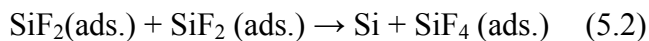
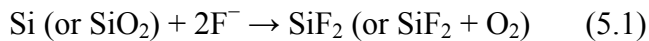
The gas used in all of the following experiments is SF₆. The reasons for this choice have to do with the proved performance of this gas in dry etching, using laser systems, especially in the microelectronics industry [6-9]. As its absorption spectrum shows in Figure 5.9, SF₆ exhibits sufficient absorption at 193nm [10].



VUV absorption cross sections of sulfur hexafluoride SF₆ at room temperature

Figure 5.9 SF₆ VUV absorption spectrum at room temperature

The product of the reaction of SF₆ with 193nm UV radiation depends on the intensity of laser beam. Sajad, *et al*, [11] suggest that low power beams can lead to formation of adsorbed SiF₄-Si which in turn becomes volatile SF₄ gas. Under high intensity inscriptions a possible photochemical reaction is [11]:



As it is suggested by the above reactions SF₆ is capable of dry etching both Si and SiO₂, at different rates. Unfortunately, there is little information in the literature on dry etching SiO₂ using 193nm radiation and SF₆, so any measurable etch – if possible

– would have to be determined experimentally. This way, by using the backside gas etching setup a set of exposures took place with applied energy density ranging from $50\text{mJ}/\text{cm}^2$ up to $230\text{mJ}/\text{cm}^2$ that was threshold of phase mask damage.

5.3.2 Experimental results

Using the setup described in section 5.1.1, a set of exposures took place in the laboratory examining the effect of different parameters, like gas pressure, evacuation prior to gas infusion, energy density, repetition rate, and exposure dose. The nature of the setup introduced some limitations to the range of the parameters that could be altered. Chamber pressure was limited to 1.5bars because of the small thickness of the sample fused silica windows. Their thickness was limited to $500\mu\text{m}$, because the goal was to simulate the effects of UV irradiation in a gas filled MOF. The value of $500\mu\text{m}$ was still much larger than the MOF's radius, but it was the best compromise between mechanical strength and small thickness. Maximum energy density that could be used without phase mask damage was $230\text{mJ}/\text{cm}^2$. The window to be placed on the window holder is very high purity fused silica ($>99.999\%$), so that no glass dopants act as color centers and give rise to index changes after UV laser irradiation. Finally the construction material of the chamber itself prevented the use of corroding gases such as HCl, since the chamber would contaminate the exposed window with corrosion products, negating any possible grating formation.

The analysis of the irradiated spots on the glass mainly involves diffraction efficiency measurement, optical microscopy scanning electron microscopy (SEM) analysis and atomic force microscopy (AFM). Diffraction efficiency was the first thing to be measured at the irradiated spots, because it provided undeniable proof of grating formation. Results from these measurements are presented in Figure 5.10. If diffracted orders were visible then grating formation definitely took place, otherwise optical microscopy, or SEM was utilised to check if any periodic structure was formed. The diffraction efficiency setup involved a 632.8nm He-Ne CW laser. Maximum output power was of the order of 10mW . The red laser beam was directed using a 45° mirror to a 20cm focal length spherical lens that focused the beam to the irradiated spot. The focused laser beam was several times smaller than the irradiated spot, so scanning of the sample was employed.

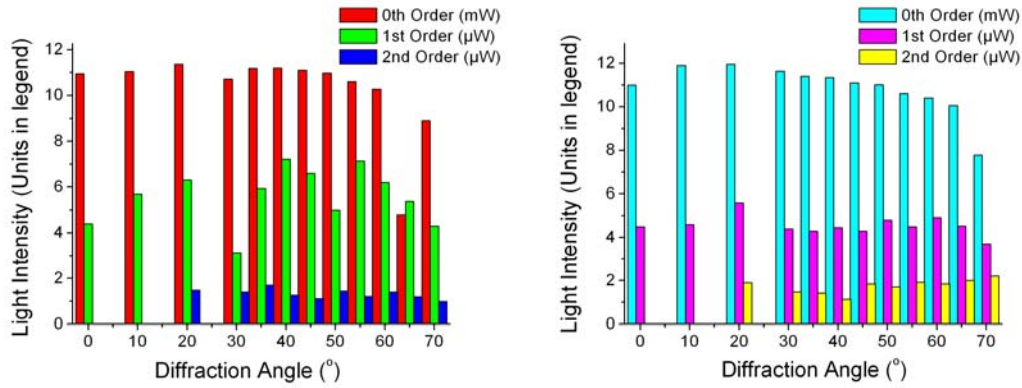


Figure 5.10 Diffraction efficiency results from samples irradiated with: (a) 255mJ/cm² energy density, after 100000 pulses of exposure and 1bar of SF₆ pressure, (b) 355mJ/cm², 100000 pulses and 1 bar of SF₆ pressure.

The strength of the inscribed grating is determined by the power of the measured diffraction orders. At first, exposures of as few as 50 pulses were realized, gradually escalating to exposures of 100000 and 250000 pulses. The effect of gas pressure was also studied, by exposing the window to 193nm radiation under 0.8bar, 1bar and 1.2bars of SF₆ pressure.

The experimental results revealed the existence of a threshold energy above which grating formation took place. This energy density threshold was approximately 177mJ/cm². For any energy density below this value, no grating formation was observed. An increase of SF₆ pressure from 0.8 bars to 1.2 bars did not give rise to grating formation at energy densities below 177mJ/cm². Furthermore, by irradiating a fused silica window having the chamber filled with air, there was a very weak photosensitive grating formation, invisible to the eye and optical microscope, but sufficient for scattering a weak 1st diffraction order.

In order to further understand the impact of each experimental parameter on the inscription process, as well as, the topology of the grating formed, optical, scanning electron and atomic force microscopy were used for sample analysis. In Figure 5.11 optical microscopy images are presented for the 177mJ/cm² exposure.

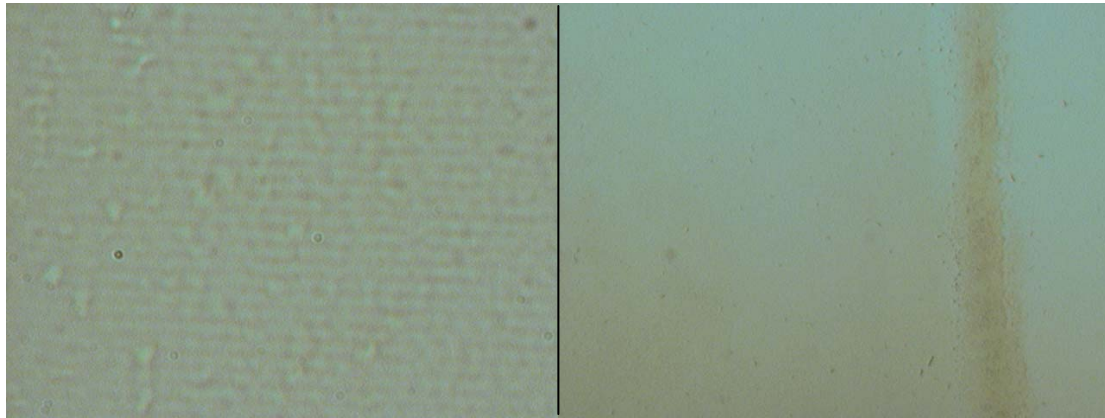


Figure 5.11 Right: 1000x magnification of backside gas etched fused silica window. Left: 50x magnification of the same window

On the left part of the Figure 5.11, the grating periodicity inscribed is clearly visible at 1000x magnification. Further, the brownish outline visible at the 50x magnification frame could be the product of photochemical reaction of SF_6 , since it was not removed after ultrasonic cleaning. Increasing the exposure energy density to $355\text{mJ}/\text{cm}^2$ resulted in higher diffraction efficiency of the 1st diffracted order and also a larger area of deposited material, reinforcing the speculation that the brownish formation observed at low magnifications is the accumulation of photodissociation products. The $355\text{mJ}/\text{cm}^2$ required less accumulated energy density to be formed than the $177\text{mJ}/\text{cm}^2$ grating. This fact is an indication of a process that is heavily dependant on the intensity per pulse and less dependant on the total accumulated energy density incident to the window.

In Figure 5.12 SEM and AFM scans of the $355\text{mJ}/\text{cm}^2$ spot are presented.

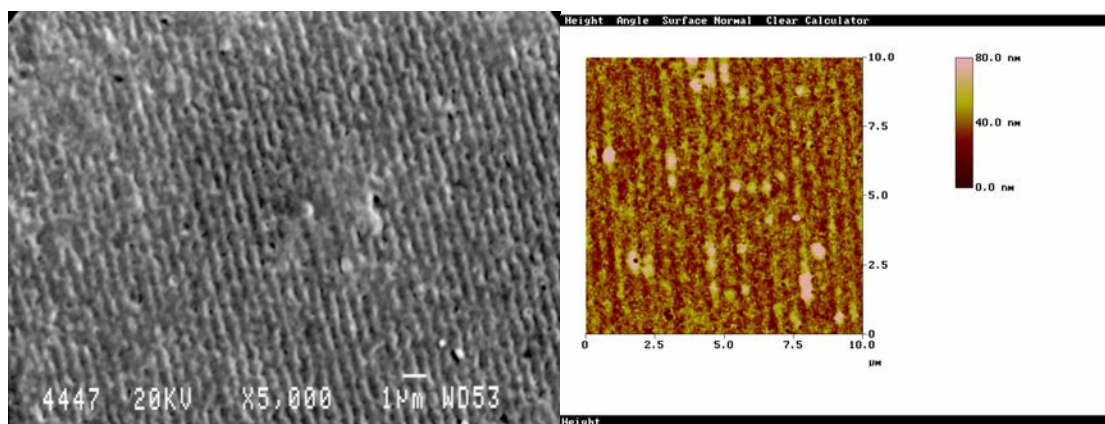


Figure 5.12 SEM (left) and AFM (right) scans of the grating inscribed in fused silica window using $355\text{mJ}/\text{cm}^2$ per pulse.

The large energy density per pulse probably ablated large amounts of metallic material from the chamber which in turn was deposited directly to the irradiated

window. In both SEM (left picture) and AFM (right picture) scans this material deposition is obvious and results in abrupt variations of the grating depth. Nevertheless, it is undeniable proof that the grating formed was not an index grating. The question that arises at this point is whether it is a relief grating, or a deposition grating. Since the grating edges are gently fading into the background material, it was very difficult to determine from SEM or AFM scans if the grating is formed by removing SiO₂ or by depositing photochemical reaction or metallic materials. In order to further investigate this matter, a 255mJ/cm² exposure was realized having the window protected from ablated metallic material, using another fused silica window right in front of the one to be irradiated. The resultant structure was much more finely defined, with clearer features and finer details. An AFM scan of this grating is presented in Figure 5.13.

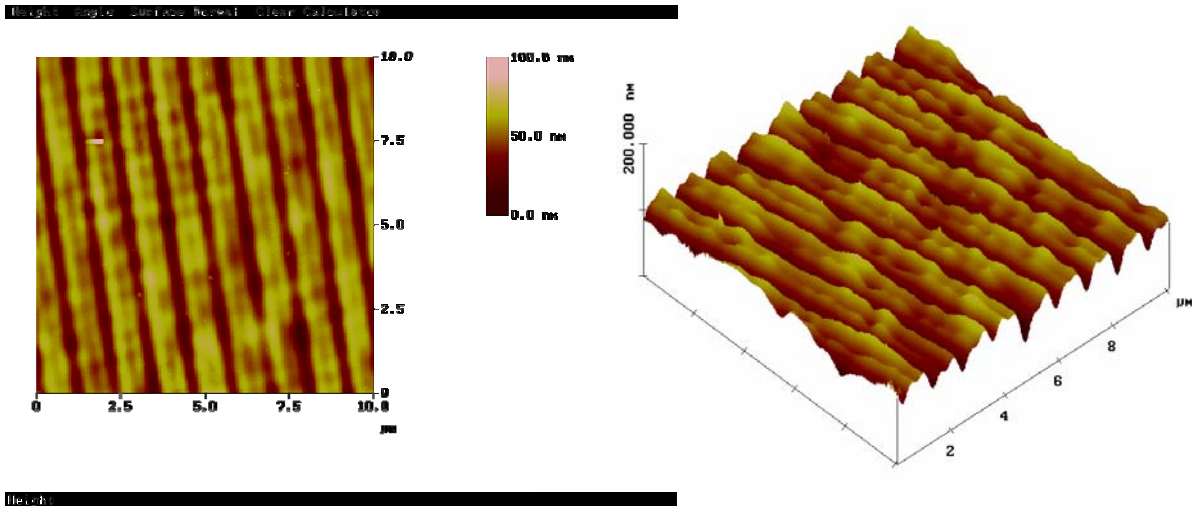


Figure 5.13 AFM scan of the grating inscribed with 255mJ/cm² per pulse

The maximum depth of the structure notches does not exceed 70nm, the grating lines appear to be parallel to each other and surface roughness is relatively high, indicating an etching mechanism rather than a deposition one. However AFM scans of the sample outside the exposure region revealed a plethora of spikes formation, or deposited photodissociation products.

With the above results at hand, having strong indications of grating formation, by means of etching, experiments were focused on recording Bragg gratings inside photonic crystal fibers.

5.4 Microstructured Optical Fiber Inscriptions

5.4.1 Inscriptions without gas flow

The first set of exposures to be presented, are those that took place without infusing any gas inside the fiber hyperstructure. The purpose of these exposures is to check if the setup is capable of forming an index grating and to study the photosensitivity of the high quality glass MOF. Bragg grating inscription in MOFs has already been reported in the literature for custom made fibers [12], or for hydrogenated fibers [13], but not for commercially available ones. Three different energy densities were used for these inscriptions, those of $9\text{MW}/\text{cm}^2$ ($90\text{mJ}/\text{cm}^2$), $17\text{MW}/\text{cm}^2$ ($170\text{mJ}/\text{cm}^2$) and $23\text{MW}/\text{cm}^2$ ($230\text{mJ}/\text{cm}^2$) intensity per pulse. Repetition rate of 40Hz was used for all exposures. These inscriptions – due to the lack of gas infusion – were the only ones possible to monitor the grating transmission spectrum online. The spectral data was analyzed using standard coupled mode theory and the resulting modulated and average index changes are presented in Figures 5.14a and 5.14b.

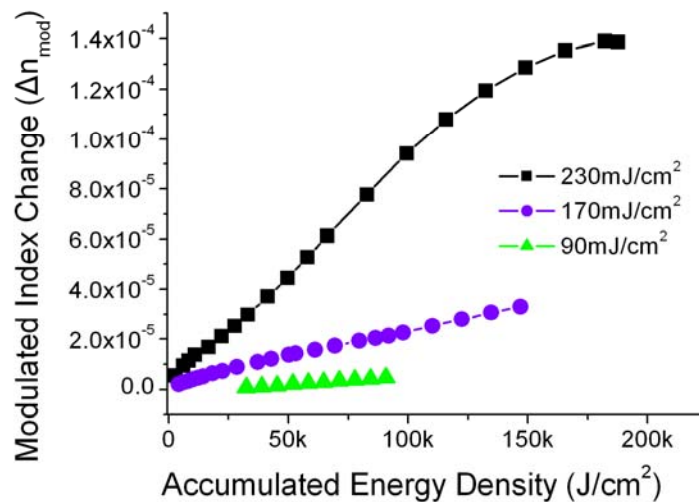


Figure 5.14a Modulated Index change versus accumulated energy density for inscriptions on commercial MOF using 193nm 10ns laser radiation

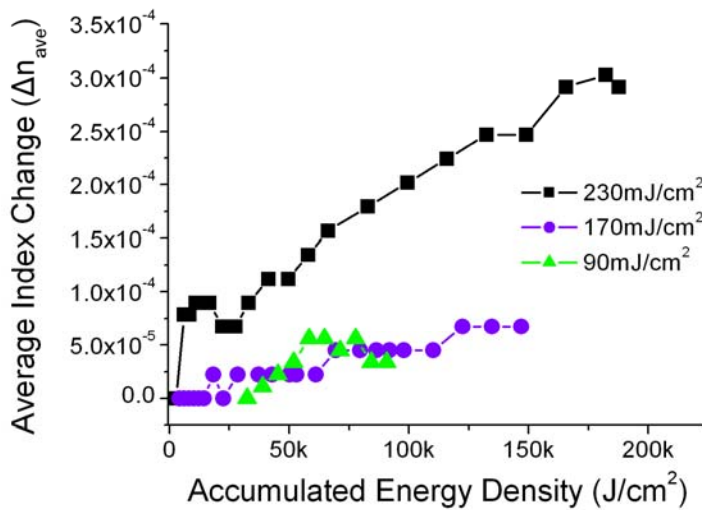


Figure 5.14b Average Index change versus accumulated energy density for inscriptions on commercial MOF using 193nm 10ns laser radiation

A linear and monotonous evolution of the modulated refractive index changes is observed, with the high energy density inscription achieving the largest value of index change (1.4×10^{-4}). The corresponding average index change is 3×10^{-4} . The index evolution curves of 170mJ/cm^2 and 90mJ/cm^2 inscriptions indicate lack of saturation of the recording process. The significant deviations of the refractive index change achieved under fixed accumulated energy density for the three different energy densities applied, demonstrate the impact of pulse fluence in the inscription process. Such large dependence on the energy content of pulse may denote the existence of a two photon or two step absorption mechanism. Such a mechanism is likely to take place, since the energy gap of fused silica is 9.3eV and the photon energy of the 193nm laser is 6.4eV .

The primary mechanism of the photoinduced refractive index changes in pure silicate glasses has been speculated to be that of two-photon/step absorption. This non linear process is causing structural rearrangement of the glass network [15, 17], through extensive bond cleaving. Nevertheless, there is also a contribution of point defects in the glass that give rise to index changes, through a single photon photosensitivity mechanism [14, 16, 18]. However, these defects are expected to contribute only at the initial stage of the grating recording, until they are depleted by the laser radiation.

In Figure 5.15 the reflection and transmission spectra of the 4mm long Bragg grating recorder with 230mJ/cm^2 and 782000 pulses are presented. After 187kJ/cm^2 of incident accumulated energy density, apart from the fundamental mode reflected (1542.88nm), there is a secondary, higher order one (1541.12nm) which is visible only in the transmission spectrum. There is also a general degradation of the fibre transmittance on shorter wavelengths indicating coupling to radiation modes [20]. Their origin is probably the formation of relief structures inside the fibre capillaries through compaction effects.

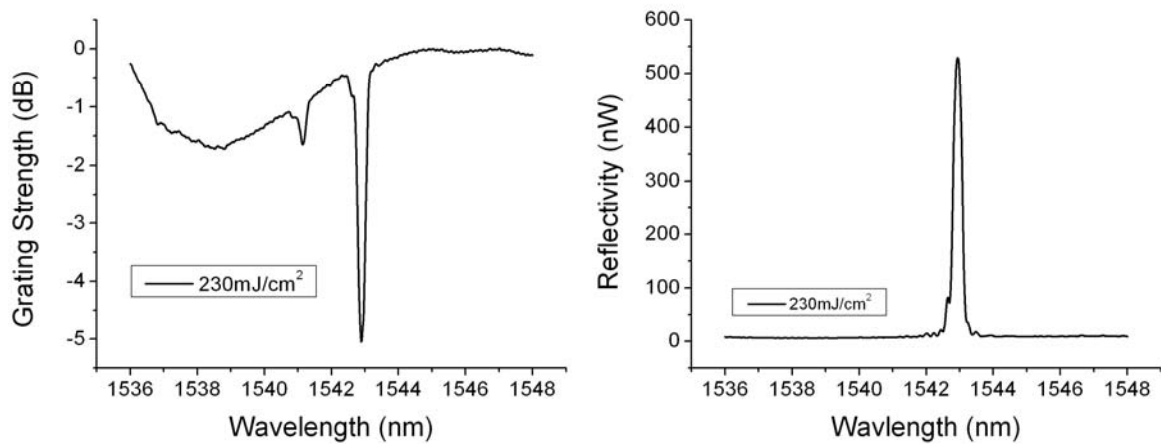


Figure 5.15 Transmission (left) and reflection (right) spectrum of the MOF inscribed with 230mJ/cm^2 energy density per pulse at the saturation point

In order to gain insight on the physical mechanism responsible for the grating formation, the fibres were subjected to thermal annealing until reaching the complete erasure point. The results of this isochronal annealing process are presented in Figure 5.15. The grating inscribed with 90mJ/cm^2 energy density was excluded from this study, due to its weak reflectivity. Nevertheless, for the other two cases a very similar annealing decay curve is obtained, with the marginal differences observed between them being attributed to experimental errors. This identical annealing behaviour indicates that that the same recording physical mechanism takes place, producing the same kind of defects. Taking into consideration the large difference of reflectivity of the two annealed gratings, this mechanism seems to have the same effect independently of the magnitude of the modulated index change. Moreover, interesting remarks can be made on the temperature stability of these gratings. Grating strength remains unaffected until a temperature of 150°C is reached. After this point, both gratings gradually lose a percentage of their reflectivity until the demarcation point of 900°C . By comparing to Type IIA gratings in B/Ge fibres (see chapter 4), there are

again distinct differences, with the most profound one, the total erasure of any index change at 600°C or 700°C in the best of cases – as presented in this work. These gratings retain a 50% or 40% of their strength at the above temperatures, indicating a totally different mechanism responsible for the index changes.

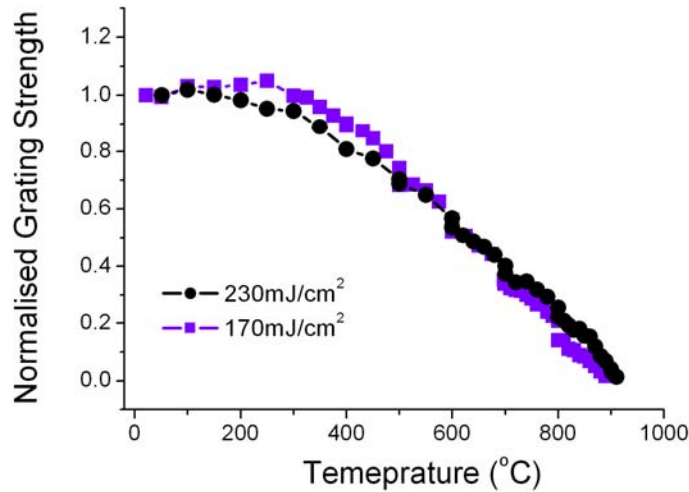


Figure 5.16 Thermal annealing decay curve of the gratings inscribed in MOFs without gas infusion

5.4.2 Incriptions with SF₆ flow inside the PCF

After the successful inscription of Bragg gratings in MOFs without gas flow, exposures using SF₆ gas followed. The restriction of obtaining only reflection spectrum during the exposure, along with the perturbation caused by the gas flow inside the MOF, resulted in a difficulty of obtaining a steady reference spectrum before the Bragg grating inscription. Each inscription exhibited different level of losses for different fiber lengths and gas flows. Assuming an output power of A from the EDFA light source, the coupler directs $A/2$ of light towards the optical fiber connector. This connector introduces a power loss of l to the light entering towards the MOF. The grating structure is back reflecting the light with an efficiency of R corresponding to the reflectivity of the grating. The reflected light suffers another loss of l factor from the MOF-coupler connector. Then the reflected light is halved as it passes through the 50/50 coupler and is directed to the Optical Spectrum Analyzer with a power of $\frac{A}{4} Rl^2$ (Figure 5.17).

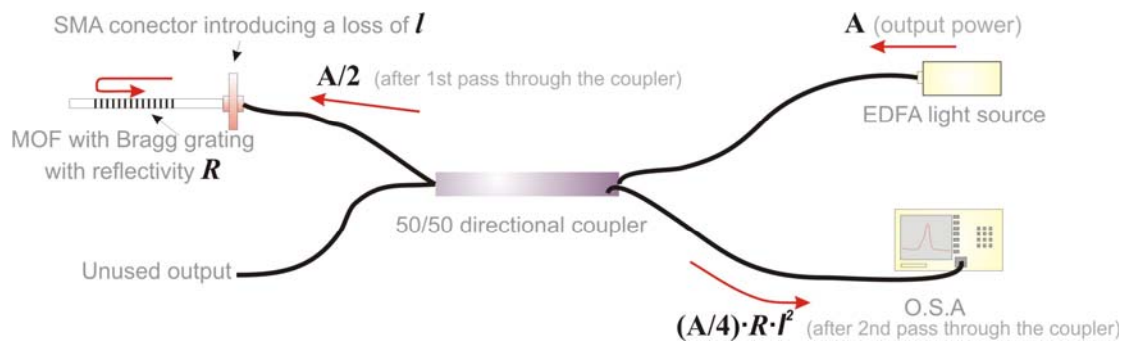


Figure 5.17 Diagram of losses introduced by the directional coupler connection

Although the online monitoring of the reflection spectrum is acceptable for Bragg grating recording, a large part of the dynamics of the inscription process is missed by the inability to monitor online the actual fiber transmission spectrum.

After several test runs, the ideal inscription conditions were found to be 1.5bar SF_6 pressure at the custom MOF connector, with minimum MOF length to be 60cm. No tension was applied to the fiber during the inscriptions. The repetition rate was 40Hz. Energy densities used for this case are over $170\text{mJ}/\text{cm}^2$. According to a work by Sajad, *et al*, [11], the threshold energy density value to photodissociate SF_6 with 193nm laser radiation is $165\text{mJ}/\text{cm}^2$, which comes in agreement with our observations. SF_6 inscription data will be presented side by side with the results obtained for the non- SF_6 -infused fibers, for comparison reasons. In Figure 5.18 the grating strength is plotted versus the accumulated energy density. Grating strength is calculated by comparing the reflection peak at the end of the exposure with the grating strength of the transmission spectrum and extrapolating that value over the reflection peaks during the inscription.

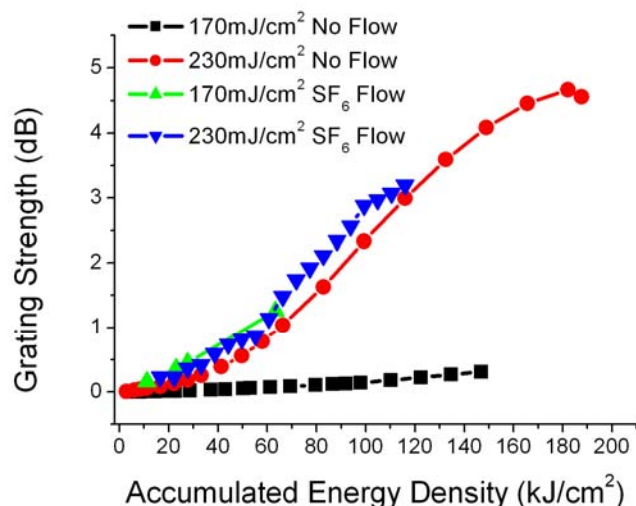


Figure 5.18 Grating Strength of various inscriptions realized with and without gas flow

In the above Figure the inscriptions realized with SF₆ flow and the one with 230mJ/cm² without flow appear to be multifold faster than the other one. The most interesting feature is the large gap in efficiency between the two 170mJ/cm² Bragg grating recordings. The one that was realized with SF₆ flow inside the holey matrix of the MOF achieves for the same accumulated energy density – or number of pulses since they have the same energy density per pulse – a much larger value of grating strength. Before moving to any conclusions it is now necessary to examine the difference between the two 230mJ/cm² inscriptions. The differences here are much less exaggerated, but the SF₆ flooded fiber still exhibits a larger value of grating strength for the same amount of accumulated laser pulses. Moreover, the two SF₆ inscriptions exhibit an almost identical value of grating strength for the same accumulated energy density. In total, these remarks indicate an SF₆ photochemical mechanism that once initiated contributes to the grating formation the same, rather irrespectively of the energy density per pulse.

Again, further insight into the inscription mechanisms is provided by the annealing of the fibers. The annealing results of the 230mJ/cm² grating inscribed with SF₆ flow will be presented side by side with the results of the 230mJ/cm² grating inscribed without gas flow. In Figure 5.19 the grating strength of the above two gratings is plotted versus annealing temperature.

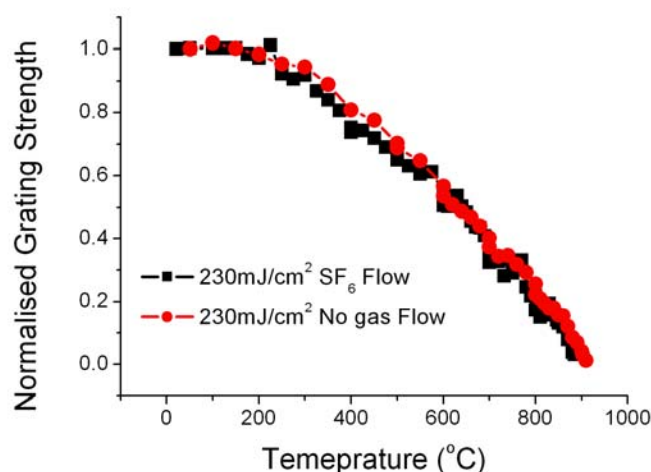


Figure 5.19 Thermal annealing decay curve of the gratings inscribed in MOF with and without gas flow

The resulting graph actually reveals a zero contribution of the SF₆ gas in the thermal stability of the grating. The two curves are practically the same, minimizing the possibility of existence of an etching mechanism. If any etching would occur, the relief grating part would be unaffected by temperatures below 1100°C, which is the glass transition point of fused silica. The inscription results however, show that SF₆ does contribute to the grating formation process. A possible explanation of this behavior could be justified by accounting the photodissociation products of SF₆ [11]. It is possible that during the UV irradiation of the gas filled fiber, SF₆ dissociates into products that are periodically deposited in the holey region of the fiber. These products are initially contributing to the grating strength until no more material can be deposited at the same spot. Over-deposition could be the reason of Fabry-Perot resonances observed during the inscription process. When the fiber is subjected to high temperatures, the deposited material is probably detached from the holes of the fibers through thermal excitation or by reacting with the fiber's SiO₂, giving off volatile products [11]. Thus no differences are observed during the annealing of the SF₆ filled and pristine MOF.

The plausibility of the above assumption could be confirmed by microscopically scanning the exposed holey matrix of a MOF, before annealing. For this reason another 170mJ/cm² inscription took place with SF₆ flow through the fiber. All experimental parameters remained identical to the ones of the previous recordings with SF₆ flow. After irradiation, the fiber was precisely cut at the grating region and

sent for SEM analysis. A set of pictures obtained from the scan is presented in Figure 5.20.

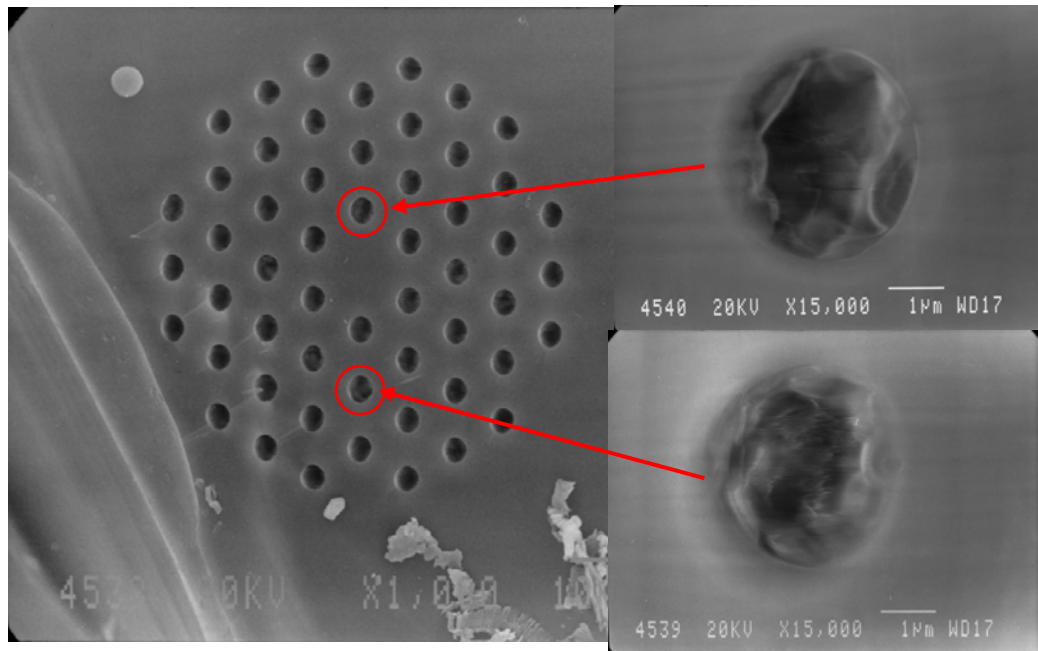


Figure 5.20 SEM scan of the fiber irradiated with gas flow in the fiber capillaries

The above images clearly reveal the existence of deposited material in the holes of the fiber. Unfortunately no data concerning the periodicity of this formation could be extracted from SEM scans. The outermost capillary ring of the fiber seems the least affected by the material deposition, which is surprising, since that ring is the first the radiation meets. However, the computer simulations demonstrated large energy density in the inner capillary ring of the fiber. The simulation results come in good agreement with the observed distribution of material deposition in the fiber capillaries which is maximized at the inner capillary ring. In order to have maximum effect on the grating reflectivity, any material deposition should take place in the inner ring of holes, where the propagation mode field is extended. Supposing that the SF_6 product that was deposited in the capillary wall, did contribute to the grating reflectivity, then the above remark comes in good agreement with the grating formation rates observed in Figure 5.18. Finally, another test conducted to check the grating's structure, was to probe visible light into the fiber and check for scattering at the grating section. In Figure 5.20, a 532nm fiber laser is coupled to the MOF and the laser light scattering is easily visible in dark environment.

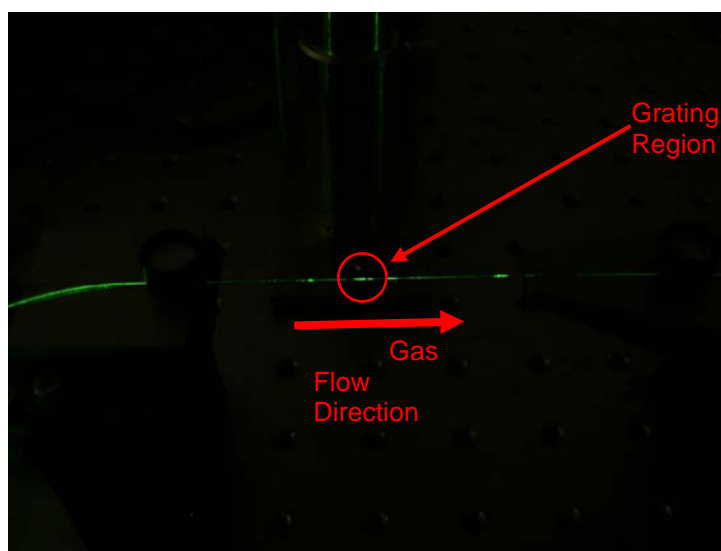


Figure 5.21 Photograph showing 532nm laser light scattered off from the fiber core

The glowing green part of the fiber on the left side of the picture has not its polymer jacket removed and thus scatters light intensely. When the jacket is removed, light remains confined inside the fiber until the grating region. The grating region itself exhibits light scattering along its length, apart from a small section near its end. Exactly after the end of the grating region and a few centimeters away from it as well, some light scattering indicates deposition of material along the gas flow direction. This measurement was the final confirmation of material deposition inside the fiber holes.

5.4.3 Inscription attempts using other gases

Following the examination of the SF₆ inscription results, an alternate route to gas etching of the silicate fiber was attempted. One of the gases used for this purpose was HCl, which irradiation produces Cl⁻ which is capable of etching SiO₂.

Unfortunately the technical difficulties on infusing HCl into the PCF were greater than expected. HCl is a highly corroding gas, requiring special materials for its manipulation. Although the setup tubing was changed from acrylic to Teflon, the custom gas connector from brass to special stainless steel and a special protective cover was used for the sealing of the whole setup, HCl proved corrosive enough to destroy the part of the stainless steel connector, whose debris stemmed the fiber holes.

Another gas that was examined was CHF₂Br. Although, its absorption spectrum at UV revealed a small value of absorption cross section for 193nm [10], its photodissociation products included F⁻ which is a strong SiO₂ etchant [19].

Unfortunately, the small absorption cross section prevented any photodissociation inside the MOF, so no results were obtained for that case either.

5.5 Conclusive remarks

In this chapter the inscription of Bragg gratings was demonstrated in both gas flooded and non-flooded microstructured optical fibers. Similar modulated refractive index changes were achieved for both cases under identical exposure dose and similarities were also observed in the annealing behavior of the fibers. The above remarks lead to the conclusion that no etching occurred during the irradiation process. However, SEM scans of the grating region cross section revealed material deposition in the fiber capillaries. The deposited material could not be identified, but could be exploited in the future to construct deposition gratings.

The inability to form a relief grating in the fiber capillaries could be attributed to the lack of precise control of gas flow in the capillaries or vibrations in the fiber due to rapid flow of the gas inside it. A high accuracy mass flow controller would help overcome both of the above obstacles. The use of high intensity laser sources (picosecond or femtosecond pulse duration) might also introduce an advantage over the use of nanosecond lasers. However, the above suggestions remain to be experimentally tested to check their viability.

References

- [1] More information can be found on <http://www.ibsen.dk>
- [2] More information on the ESM-12-01 fiber can be found on <http://www.crystal-fibre.co.uk>
- [3] The ray tracing software is the Zemax from Zemax Development Corporation. More information can be found in: <http://www.zemax.com/>
- [4] M. Qiu, "Analysis of guided modes in photonic crystal fibers using the finite-difference time-difference domain method", *Microwave and Optical Technology Letters*, **30**:327-330, (2001)
- [5] A demo version of the OptiFDTD software from OptiWave Inc. was used for FDTD simulations. More information can be found in <http://www.optiwave.com/site/products/fdtd.html>
- [6] T. J. Chuang, "Multiple photon excited SF₆ interaction with silicon surfaces", *Journal of Chemical Physics* **74**: 1453-1460, (1981)
- [7] Yu. A. Gorokhov, A. L. Gritsenko, V. N. Likhman, "Interaction of SF₆ Multiple Photon Dissociation Products with Silicon and SiO Surfaces", *Laser Chemistry* **5**: 35-52, (1984)
- [8] T. J. Chuang, "Infrared laser induced reaction of SF₆ with silicon surfaces", *Journal of Chemical Physics* **72**: 6303-6304, (1980)
- [9] D. J. Ehrlich, R. M. Osgood, T. F. Deutsch, "Laser chemical technique for rapid direct writing of surface relief in silicon", *Applied Physics Letters* **38**: 1018-1020, (1981)
- [10] VUV absorption spectrum of SF₆ and CHF₂Br retrieved online from: <http://www.atmosphere.mpg.de>
- [11] B. Sajad, P. Parvin, M. A. Bassam, "SF₆ decomposition and layer formation due to excimer laser photoablation of SiO₂ surface at gas–solid system", *Journal of Physics D: Applied Physics* **37**: 3402-3408, (2004)
- [12] N. Groothoff, J. Canning, E. Buckley, K. Lyttikainen, J. Zagari, "Bragg gratings in air–silica structured fibers", *Optics Letters* **28**: 233-235, (2003)
- [13] L. Fu, G. D. Marshall, J. A. Bolger, P. E. Steinvurzel, E. C. Mägi, M. J. Withford, B. J. Eggleton, "Fibre Bragg Gratings Written in Pure Silica Photonic Crystal Fibres with Ultraviolet Femtosecond Laser Pulses",

- [14] I. Hiroaki, A. Kazuo, H. Hideo, A. Yoshihiro, A. Takehiko, I. Hiroshi, “Dependence of defects induced by excimer laser on intrinsic structural defects in synthetic silica glasses”, *Physical Review B* **44**: 4812-4818, (1991)
- [15] C. Fiori, A. Devine, “Evidence for a wide continuum of polymorphs in α -SiO₂”, *Physical Review B* **33**: 2972-2974, (1986)
- [16] D. L. Griscom, *Proceedings of SPIE* **541**: 38, (1985)
- [17] M. Rothschild, D.J. Ehrlich and D.C. Shaver, “Effects of excimer laser irradiation on the transmission, index of refraction, and density of ultraviolet grade fused silica”, *Applied Physics Letters* **55**: 1276-1278, (1989)
- [18] D. L. Griscom, “Defect structure of glasses: Some outstanding questions in regard to vitreous silica”, *Journal of Non Crystalline Solids* **73**: 51-77, (1985)
- [19] V. L. Orkin, E. E. Kasimovskaya, “Ultraviolet Absorption Spectra of Some Br-Containing Haloalkanes”, *Journal of Atmospheric Chemistry* **21**: 1-11, (1995)
- [20] T. Erdogan, “Fiber Grating Spectra”, *Journal of Lightwave Technology*, **15**: 1277 – 1294, (Review Article), (1997)

6. Conclusions – Future perspectives

Summarizing the results of this thesis, two major points of interest are distinguished. The first point refers to the fabrication of Bragg grating reflectors in a commercial B-Ge codoped optical fiber by employing 248nm 120fs, 500fs and 5ps laser radiation. The availability of various pulse durations rendered possible the observation of the effect of the pulse intensity, as well as, that of the pulse duration and energy in the inscription process. Average and modulated refractive index data acquired by the exposures were examined alongside with thermal annealing curves of the gratings in order to further illustrate the underlying photosensitivity mechanisms. The acquisition of rigorous data concerning photoinduced changes in the exposed optical fibers was realized by utilizing Raman microscopy. Considering these Raman scattering data, it was observed that shorter pulse durations cause extended changes in the fiber core matrix, which were manifested also in the thermal annealing curves. The nature of these changes is speculated to be primarily structural, a remark extracted by observing changes in specific Raman spectrum peaks and the enhanced thermal stability exhibited by some of the inscribed gratings. Solid conclusions concerning the origin of the extended thermal stability could not be extracted solely from the Raman spectra and would require a more thorough study of the fiber photosensitivity and possibly the utilization of other characterization techniques.

Nevertheless, it was concluded that enhanced thermal stability is observed only after high intensity and high fluence laser beam is utilized for the fabrication of the Bragg reflector. The extra 100°C of thermal stability beyond the typical values of Type IIA gratings could be exploited in high temperature hostile environments for thermal, structural or chemical sensing. The comparative study of the Bragg grating inscriptions must be expanded to the use of more laser wavelengths and pulse durations, so that more rigorous remarks can be extracted, concerning the fiber photosensitivity.

The second achievement presented in this thesis refers to the inscriptions of Bragg gratings in commercial microstructured optical fiber using 193nm 10ns laser radiation. The microstructured fiber used is manufactured from high quality glass and exhibits intrinsically low photosensitivity. The Bragg grating inscriptions that were presented in this thesis, did not include fiber sensitization and were realized in pristine fiber, by simply using the phase mask technique. The effect of the pulse energy, as

well as, the addition of various gases inside the fiber capillaries for manufacturing relief gratings was studied. Although the realization of relief gratings was not successful, it was found that it is possible to cause photochemical changes inside the fiber capillaries. Moreover, the complex side illumination during grating recording in the MOF, was simulated using computer ray tracing and FDTD software. Taking into account non linear absorption in the silicate glass, it was found that only 55% of the incident pulse energy reaches the fiber core, indicating that more energy might be required to cause photodissociation of the etching gas that in turn would internally etch the fiber capillary. Other technical issues related to the gas flow in the fibre complex and stability issues that have to do with the control of that flow were also observed during the experimental work.

The uniqueness of the MOFs structure renders the Bragg gratings inscribed inside them attractive for several high-end applications. The ability to infuse gases or liquids inside the fiber core makes them ideal candidates for chemical and biological sensing with unmatched sensitivity. Furthermore, an infused liquid or gas can also act as cooling means for power delivery systems or be the part of an optical nano-liter liquid infusion system. By simultaneously splicing the fiber ends it can also act as a gas micro chamber with optical pressure readouts. In any case, the potential applications that may come out from the development of such Bragg reflectors in MOFs can be of a large number and significance.

List of Publications

Journal Papers

- 1) G. Violakis, M. Konstantaki, S. Pissadakis, “Accelerated Recording of Negative Index Gratings in Ge-Doped Optical Fibers Using 248-nm 500-fs Laser Radiation”, *IEEE Photonics Technology Letters*, **18**: 1182, (2006)
- 2) G. Violakis, S. Georgiou, M. Konstantaki and S. Pissadakis, “Inscription of Type IIA gratings in B-Ge optical fibres using femtosecond and picosecond 248nm laser radiation”, *to be submitted in Journal of Lightwave Technology*
- 3) M. Strosch, T. Woggon, U. Lemmer, G. Bastian, G. Violakis, S. Pissadakis, “Organic semiconductor distributed feedback laser fabricated by direct laser interference ablation”, *Optics Express* **15**: 3968-3973, (2007)
- 4) Michalis Livitzis, Georgios Violakis, Stavros Pissadakis, “Bragg Grating Recording in an All-silica Microstructured Optical Fiber Using 248nm, 5ps Laser Radiation”, *to be submitted in Optics Letters*
- 5) S. Pissadakis, G. Violakis, M. Konstantaki, “Recording of type IIA Bragg gratings in B-GE silicate fibres using 213nm radiation”, *to be submitted in Microwave and Optical Technology Letters*

International Conferences

- 1) G. Violakis, M. Konstantaki, S. Pissadakis, “Inscription of Thermally Durable Type IIA Bragg Gratings in B/Ge-codoped optical fiber using 248nm 500fs radiation”, *Conference on Lasers and Electro-Optics / Quantum Electronics and Laser Science Conference (CLEO/QELS)*, May 2006, Long Beach, California, U.S.A.
- 2) S. Pissadakis, M. Konstantaki, G. Violakis, “Recording of Type IIA Gratings in B-Ge codoped Optical Fibres Using 248nm Femtosecond and Picosecond Laser Radiation”, *ICTON 2006*, Nottingham, UK, June 2006 (invited)
- 3) S. Pissadakis, M. Konstantaki, G. Violakis, “Deep UV radiation induced photodissociative processes in transparent optical materials: index engineering

- and structural modification effects”, *4th LAMP*, Kyoto, Japan, May 2006 (invited)
- 4) Georgios Violakis, Stavros Pissadakis, “Bragg Grating Inscription in a Commercial Solid Core Microstructured Optical Fiber”, *ICTON 2007*, Rome, Italy, July 2007 (invited)
 - 5) Georgios Violakis, Maria Konstantaki, Stavros Pissadakis, “Comparative Studies on Type IIA Photosensitivity in a B-Ge Optical Fiber Using Ultraviolet Femtosecond Radiation”, *Bragg Gratings Photosensitivity and Poling Glass Waveguides 2007*, Quebec, Canada, September 2007
 - 6) Stavros Pissadakis, Michalis Livitzis, Georgios Violakis, “Inscription of Bragg reflectors in all-silica microstructured optical fibres using 248nm, picosecond and femtosecond laser radiation”, *Photonics Europe Conference*, Strasbourg, France, 2008 (invited)
 - 7) G. Violakis, M. Konstantaki, S. Pissadakis, “Comparative results on the recording of Type IIA gratings in B-Ge optical fibres using femtosecond and picosecond 248nm laser radiation”, *CLEO-Europe 2007*